



**SIMULATION OF MAGNETIC TARGETED DRUG  
DELIVERY**

**BY**

**AAIZA GUL**

**A DISSERTATION SUBMITTED IN PARTIAL FULFILLMENT  
OF THE REQUIREMENTS FOR THE DEGREE OF DOCTOR OF  
PHILOSOPHY (ENGINEERING AND TECHNOLOGY)  
SIRINDHORN INTERNATIONAL INSTITUTE OF TECHNOLOGY  
THAMMASAT UNIVERSITY  
ACADEMIC YEAR 2021  
COPYRIGHT OF THAMMASAT UNIVERSITY**

THAMMASAT UNIVERSITY  
SIRINDHORN INTERNATIONAL INSTITUTE OF TECHNOLOGY

DISSERTATION

BY

MS. AAIZA GUL


ENTITLED

SIMULATION OF MAGNETIC TARGETED DRUG DELIVERY

was approved as partial fulfillment of the requirements for  
the degree of Doctor of Philosophy (Engineering and Technology)

on January 11, 2022

Chairperson

  
\_\_\_\_\_  
(Associate Professor Mud-Armeen Muqin, Ph.D.)

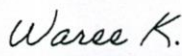
Member and Advisor

  
\_\_\_\_\_  
(Professor Stanislav S. Makhanov, Ph.D.)


Member

\_\_\_\_\_  
(Professor Pruettha Nanakorn, D.Eng.)


Member

  
\_\_\_\_\_  
(Associate Professor Waree Kongprawechnon, Ph.D.)

Member

  
\_\_\_\_\_  
(Associate Professor Pakinee Aimmanee, Ph.D.)

Director

  
\_\_\_\_\_  
(Professor Pruettha Nanakorn, D.Eng.)

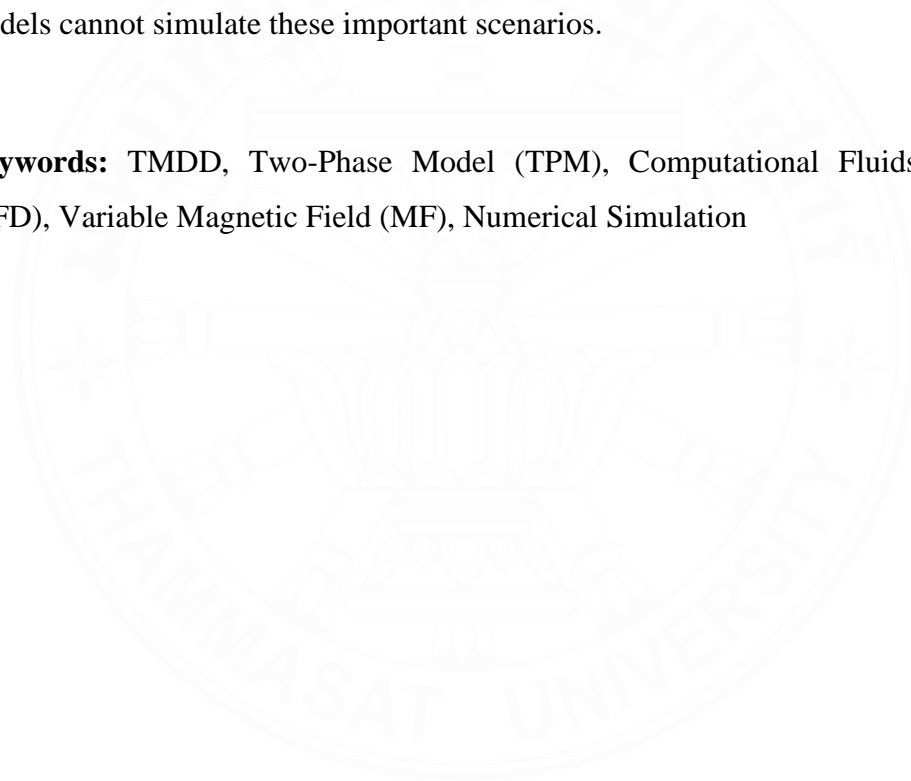
Thesis Title	SIMULATION OF MAGNETIC TARGETED DRUG DELIVERY
Author	Aaiza Gul
Degree	Doctor of Philosophy (Engineering and Technology)
Faculty/University	Sirindhorn International Institute of Technology/ Thammasat University
Thesis Advisor	Professor Stanislav S. Makhanov, Ph.D.
Academic Years	2021

## ABSTRACT

Targeted Magnetic Drug Delivery (TMDD) is a promising approach that is relevant to multimodal cancer therapy. Therefore, it is important to develop mathematical models of TMDD to serve as a second opinion for medical practitioners. A majority of TMDD models represent a mixture of blood and nanoparticles as a one-phase solution. Therefore, the magnetic nanoparticles (MN) and the blood follow the same streamlines. The existing two-phase models are usually one-way coupled, i.e., the blood flow has a strong impact on the MN flow. However, the inverse impact of the MN on the dynamics of the blood is not included in the models. To eliminate these drawbacks, the MN in a blood vessel is simulated by a two-phase (solid-liquid) flow in a 2D rectangular channel. The problem is governed by two-way coupled momentum and temperature equations for the blood flow and the MN. The numerical procedure invokes the stream function–vorticity formulation and an efficient numerical method on a finite-difference grid. The general formulation for the effect of the magnetic field is that of Biomagnetic fluid Dynamics (BFD) which incorporates both principles of MagnetoHydroDynamics (MHD) and FerroHydroDynamics (FHD). The model, validated by experimental results, has been applied to analyze the formation of and the zones of TMDD, where the velocity of the blood flow is low and the velocity

of the MN flow is high towards the magnet. Additionally, we analyze the formation of vortices relative to the magnetic force (MFs), the drag force (DF). The model is capable of simulating the (reverse) impact of the MN on the blood flow and evaluates the corresponding changes in the vorticity. The result shows that the MHD effect causes disturbance in blood flow. It reduces blood flow and minimizes the large vortices created by FHD. Moreover, the concentration of medical drugs is another essential result. These medications have the potential to harm healthy cells. Therefore, the effects of medical drugs have been evaluated against MN size. It analyzes the impact of the size and concentration of the MN on the temperature of the blood. The preceding models cannot simulate these important scenarios.

**Keywords:** TMDD, Two-Phase Model (TPM), Computational Fluids Dynamics (CFD), Variable Magnetic Field (MF), Numerical Simulation



## ACKNOWLEDGEMENTS

O Allah! Nothing is easy except what you have made easy. I thank Allah for giving me the strength and for enabling me to accomplish my work successfully.

I would like to acknowledge the tireless work of my supervisor Prof. Dr. Stanislav S. Makhanov for his guidance and support over my years at the Sirindhorn International Institute of Technology, Thammasat University.

In addition, I would like to thank my entire committee for their individual guidance and support during my doctoral studies. Thank you Prof. Dr. Pruettha Nanakorn, Assoc. Prof. Dr. Mud-Armeen Munlin, Assoc. Prof. Dr. Pakinee Aimmanee, Assoc. Prof. Dr. Waree Kongprawechnon.

My acknowledgment is to the financial support from the Excellent Foreigner Student combined with the Thammasat University Scholarship (TU-EFS) provided by Sirindhorn International Institute of Technology (SIIT), and the Center of Excellence in Biomedical Engineering of Thammasat University.

Special thanks to Assoc. Prof. Dr. Efstratios E. Tzirtzilakis for the immense support in my work, and for never refusing to answer a question of mine. Thank you for teaching me some Greeks. From αιζα (Σεβαστή).

Lastly, thanks to my friends: Pyae Pyae Phyo, Sidra, Aneeka, Irfan, and Ahmed for always listening to me, for supporting me, and for encouraging me.

Finally, I would like to thank my parents and my siblings for always being by my side.

Aaiza Gul

## TABLE OF CONTENTS

	Page
ABSTRACT	(1)
ACKNOWLEDGEMENTS	(3)
LIST OF TABLES	(8)
LIST OF FIGURES	(9)
LIST OF ABBREVIATIONS	(12)
LIST OF NANOPARTICLES	(14)
LIST OF SYMBOL/UNITS	(15)
CHAPTER 1 INTRODUCTION	1
1.1 Introduction	1
1.2 Research Background	1
1.2.1 Computational Models for TMDD	2
1.2.2 Magnetic Force Density on Matter	3
1.2.3 Magnetic Analysis of Blood	6
1.2.4 Blood Magnetization	8
1.2.5 Magnetic Field Analysis of Blood	9
1.3 Problem Statement	10
1.4 Research Objectives	11
1.5 Scope of the Study	12
1.6 Importance of the Study	12
CHAPTER 2 LITERATURE REVIEW	14
2.1 Introduction	14
2.2 Overview	14

2.3	Literature Review of TMDD	15
2.4	Magnet and Magnetic Fields	17
2.5	Numerical Simulation of TMDD	18
2.6	Tumor Microenvironments	23
2.7	Entropy Generation in MDJN	25

### CHAPTER 3 A TWO-PHASE, TWO-WAY COUPLED MODEL OF TARGETED MAGNETIC DRUG DELIVERY FOR SMALL REYNOLDS NUMBERS 27

3.1	Introduction	27
3.2	Mathematical Formulation	27
3.2.1	Governing Equations	28
3.2.2	Magnetic Field	30
3.2.3	Drag coefficient	31
3.2.4	Heat Transfer coefficient	31
3.3	Boundary and Initial Conditions	32
3.4	Dimensionless Equations	32
3.5	Grid Generation	34
3.6	Numerical Method	38
3.7	Results and Discussion	41
3.7.1	Validation of the model	41
3.7.2	Numerical Experiments and Discussion	46
3.7.2.1	Impact of the Reynolds Number	47
3.7.2.2	Impact of the Magnetic Field	53
3.7.2.3	Impact of the Size of the MN on the Blood Flow	57
3.7.2.4	Impact of the Size of the MN on the Temperature	59

### CHAPTER 4 A THREE-LAYER MODEL OF MAGNETIC TARGETED DRUG DELIVERY 64

4.1	Introduction	64
4.2	Mathematical Formulation	64
4.2.1	Governing Equations	64
4.2.2	Magnetic Field	66

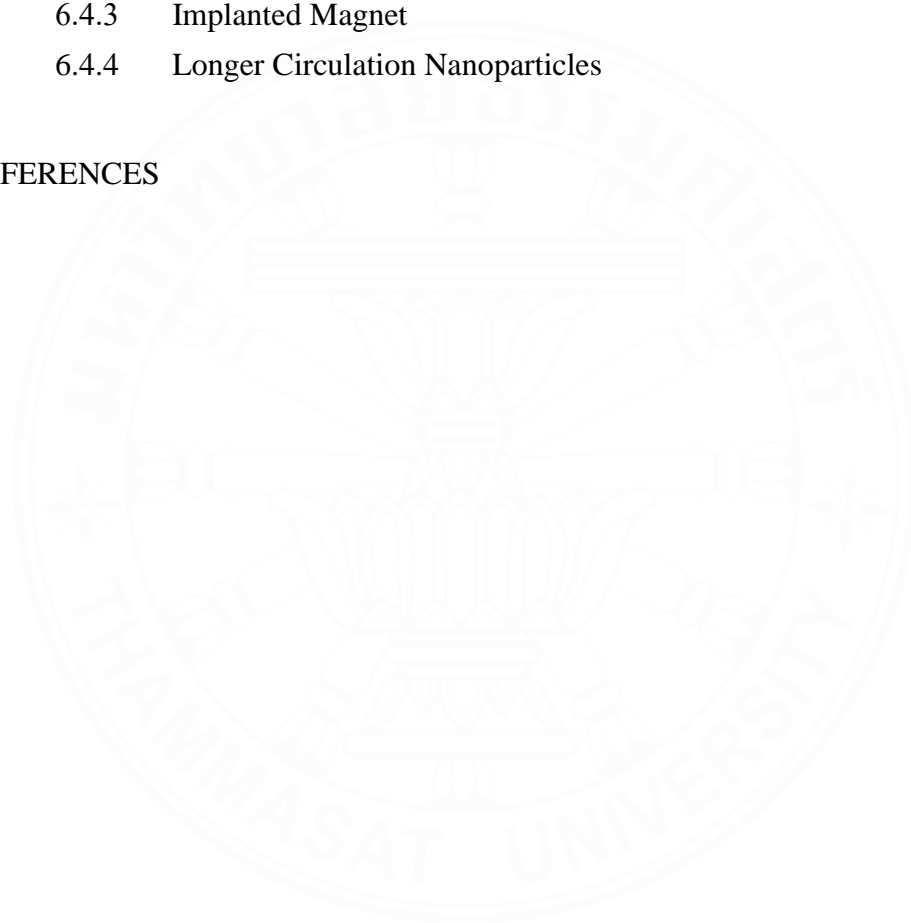
4.2.3	Therapeutic Drugs Concentration	66
4.2.4	Drag coefficient	67
4.2.5	Mass Transport Through Blood Vessel	68
4.2.6	Mass Transport Through Endothelium Membrane	69
4.2.7	Mass Transport Through Tissue	70
4.3	Boundary and Initial Conditions	73
4.4	Special Case: MHD	75
4.5	Dimensionless Equations	76
4.6	Numerical Method	79
4.7	Results and Discussion	81
4.7.1	Impact of the Magnetic Field Intensity (FHD and MHD):	81
4.7.2	Impact of MN (therapeutic drug-loaded and MN) on Blood Flow:	85
4.7.3	The Concentration of MN (therapeutic drug-loaded) in Normal and Tumor Cells:	89

## CHAPTER 5 ENTROPY GENERATION IN A MIXED CONVECTION POISEUILLE FLOW OF MOLYBDENUM DISULPHIDE JEFFREY NANOFUID 92

5.1	Introduction	92
5.2	Mathematical Formulation	92
5.2.1	Governing Equations	92
5.3	Thermo physical Properties of Nanofluids	93
5.4	Dimensionless Equations	94
5.5	Boundary Conditions	95
5.6	Mathematical Solution	96
5.7	Entropy generation	98
5.8	Nusselt Number and Skin-friction	99
5.9	Numerical Results and Discussion	100
5.9.1	Impact of the Different Parameters on the Velocity of Nanofluids	100
5.9.2	Impact of the Different Parameters on Entropy Generation	104
5.9.3	Impact of the Different Parameters on Temperature of Nanofluids	109

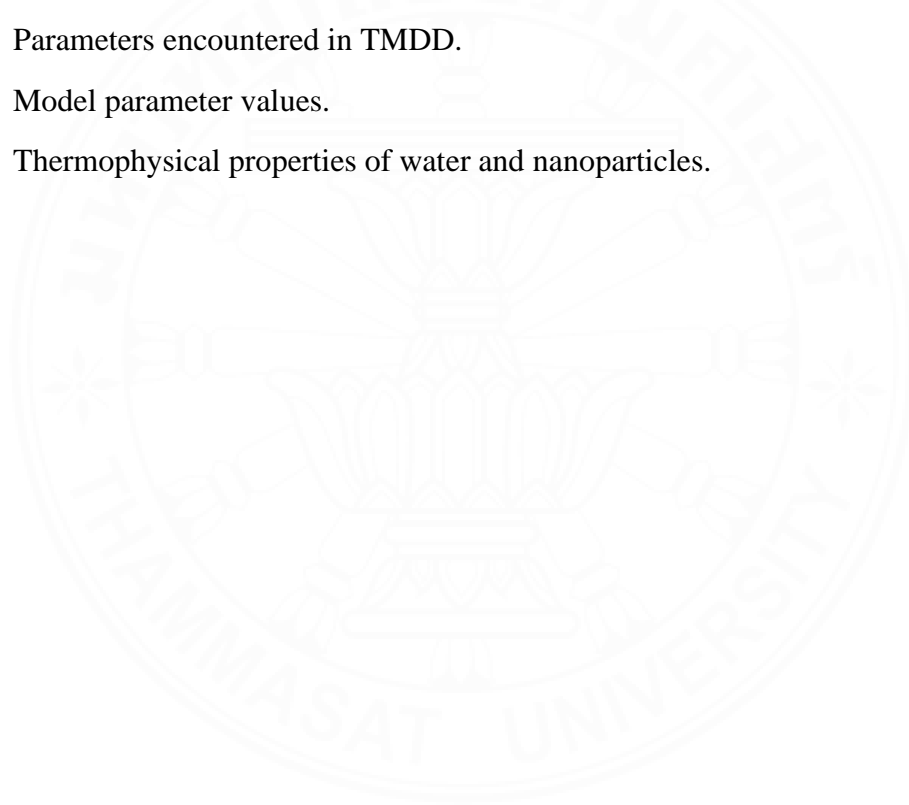


CHAPTER 6 CONCLUSION	111
6.1 Introduction	111
6.2 Conclusions	111
6.3 Limitations of the Present Work	113
6.4 Suggestions for Future Research	113
6.4.1 Damage to Vessels and Tissues	114
6.4.2 Aggregation of MN	114
6.4.3 Implanted Magnet	114
6.4.4 Longer Circulation Nanoparticles	115
REFERENCES	116



## LIST OF TABLES

Tables	Page
1.1 Various properties of blood.	7
1.2 The realistic velocities of blood flow and its nature in various blood vessels.	8
3.1 Grid-independence test.	41
3.2 Average Nusselt number of the proposed model, SPM <sub>1</sub> , SPM <sub>2</sub> vs. Experiments.	45
3.3 Average Nusselt number. Numerical models vs. Experimental data.	46
3.4 Parameters encountered in TMDD.	62
4.1 Model parameter values.	72
5.1 Thermophysical properties of water and nanoparticles.	94



## LIST OF FIGURES

Figures	Page
3.1 Flow domain and boundary conditions.	29
3.2 Adaptive finite-difference grid.	36
3.3 Blood flow, Case 1. The reference models generate similar solutions for $C_v = 0.001$ .	42
3.4 Case 1: Magnitude of the velocity for SPM <sub>1</sub> , OW, and TPM.	42
3.5 Blood flow, Case 2. The reference models vs. TPM.	43
3.6 Case 2: Magnitude of the velocity for SPM <sub>1</sub> , OW, and TPM.	44
3.7 Blood flow, $B = 0.5$ , $d = 250$ , $C_v = 0.001$ . a) Re=25, b) Re=50, c) Re=100; 1) contour lines of the vorticity function, 2) streamline plot.	51
3.8 MN flow: $B = 0.5$ , $d = 250$ , $C_v = 0.001$ . a) Re=25, b) Re=50, c) Re=100; 1) contour lines of the vorticity function, 2) streamline plots.	52
3.9 Streamlines of the blood flow: $B = 0.5$ a) $b=15$ , b) $b=10$ , c) $b=5$ .	54
3.10 Streamlines of the MN flow: $B = 0.5$ , a) $b=15$ , b) $b=10$ , c) $b=5$ .	55
3.11 Streamlines of the blood flow: $B = 1.0$ , a) $b=15$ , b) $b=10$ , c) $b=5$ .	56
3.12 Streamlines of the MN flow: $B = 1.0$ , a) $b=15$ , b) $b=10$ , c) $b=5$ .	57
3.13 Streamlines of the blood for different sizes of the MN: a) $d = 250$ , b) $d = 800$ , c) $d = 20000$ , $t_s \approx 1.0$ .	58
3.14 Streamlines of the MN for different sizes of MN:	59
3.15 Temperature of the blood flow: a) $\beta_2 = 0$ , b) $d=250$ , c) $d=800$ , d) $d=20000$ .	61
3.16 Temperature of the MN flow: a) $d=250$ , b) $d=800$ , c) $d=20000$ .	61
4.1 Blood vessel, endothelial membrane and tissue.	66
4.2 Flow domain and boundary conditions.	75
4.3 Streamlines of the blood flow: a) FHD, b) MHD, c) $B=2$ , d) $B=5$ , e) $B=8$ .	84

4.4 Streamlines of the MN flow: a) FHD, b) MHD, c) $B=2$ , d) $B=5$ , e) $B=8$ .	85
4.5 Streamlines of the blood for different sizes of the MN:	
a) $\bar{\rho}_p = 5200$ , b) $\bar{\rho}_p \approx 3015.6$ , c) $\bar{\rho}_p \approx 1343.8$ , d) $\bar{\rho}_p \approx 829.8$ , $\bar{\rho}_p \approx 1594$ , $t_s \approx 1.0$ .	87
4.6 Streamlines of the MN for different sizes of MN:	88
4.7 Concentration of drug-loaded MN in normal blood vessel, endothelial cell and tissue: $B = 2$ , $b = 10\text{cm}$ , $M_{nF} = 13125$ , $M_{nF_p} \approx 165804$ .	90
4.8 Concentration of drug-loaded MN in leaky blood vessel, endothelial cell and tissue (tumorous cells): $B = 0$ .	90
4.9 Concentration of drug-loaded MN in leaky blood vessel, endothelial cell and tissue (tumorous cells): $B = 2$ , $b = 10\text{cm}$ , $M_{nF} = 13125$ , $M_{nF_p} \approx 165804$ .	91
4.10 Concentration of drug-loaded MN in leaky blood vessel, endothelial cell and tissue (tumorous cells): $B = 5$ , $b = 10\text{cm}$ , $M_{nF} = 32812$ , $M_{nF_p} \approx 221000$ .	91
5.1 MDJN, SGN, NN vs. $\lambda_1$ .	101
5.2 Comparison of MDJN, SGN, and NN.	102
5.3 Impact of $\lambda$ on the velocity of MDJN.	102
5.4 Velocity of the MDJN vs. $\phi$ .	103
5.5 Velocity of the MDJN vs. $Gr$ .	103
5.6 Velocity of the MDJN vs. $N$ .	104
5.7 Entropy generation of MDJN vs. the SGN vs. $\lambda_1$ .	105
5.8 Impact of $\lambda$ on the entropy generation of MDJN.	106
5.9 Impact of $Br\Omega^{-1}$ on the entropy generation.	106
5.10 Impact of $Br$ on the entropy generation.	107
5.11 Impact of $\Omega$ on the entropy generation.	107
5.12 Impact of $\phi$ on the entropy generation.	108
5.13 Impact of $Gr$ on the entropy generation.	108

5.14 Impact of $N$ on the entropy generation.	109
5.15 Impact of $N$ on the temperature of the MDJN.	110
5.16 Impact of $\phi$ on the temperature of the MDJN.	110



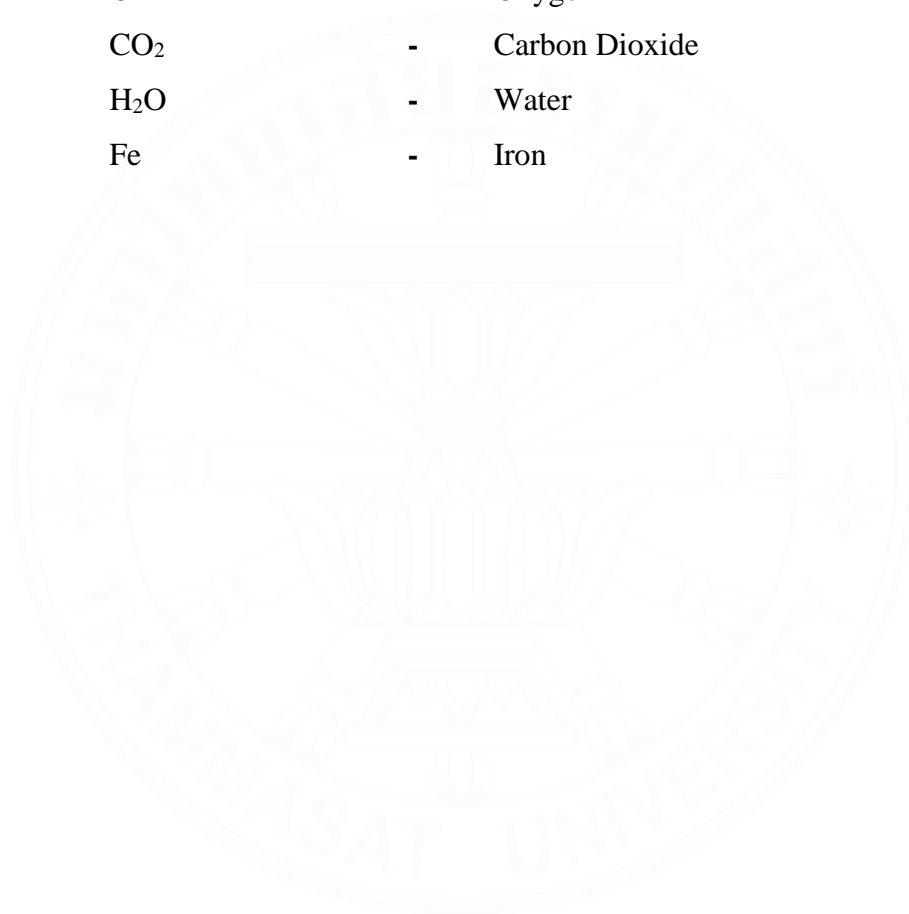
## LIST OF ABBREVIATIONS

<b>Abbreviations</b>	<b>Terms</b>
TMDD	Targeted Magnetic Drug Delivery
BFD	Bio Fluids Dynamics
FHD	Ferro Hydro Dynamics
MHD	Magnetic Hydro Dynamics
TPM	Two Phase Model
SPM	Single Phase Model
MN	Magnetic Nanoparticles
MF	Magnetic Field
MFs	Magnetic Force
DF	Drag Force
MFG	Magnetic Field Gradient
SOR	Successive Over-Relaxation
CFD	Computational Fluids Dynamics
RRDC	Renkin Reduced Diffusion Coefficient
BD	Brownian Diffusion
SD	Scattering Diffusion
DCB	Diffusion Coefficient in the Blood
DCM	Diffusion Coefficient in the Membrane
DCT	Diffusion Coefficient in the Tissue

EMD	Endothelium Membrane Diffusivity
TM	Tissue Diffusivity
RBC	Red Blood Cells
WBC	White Blood Cells
MDJN	Molybdenum Disulphide Jeffrey Nanofluid
JN	Jeffrey Nanofluid
SJN	Second Grade Nanofluid
ACS	American Cancer Society
ARC	Agency for Research on Cancer
MPS	Mononuclear Phagocyte System
PEG	Poly(Ethylene) Glycol
PLGA	Poly(Lactide-Co-Glycolide)

**LIST OF NANOPARTICLES**

<b>Formula</b>		<b>Parameters</b>
$\text{Fe}_3\text{O}_4$	-	Ferric oxide
$\text{MoS}_2$	-	Molybdenum disulfide
$\text{Al}_2\text{O}_3$	-	Alumina oxide
O	-	Oxygen
$\text{CO}_2$	-	Carbon Dioxide
$\text{H}_2\text{O}$	-	Water
Fe	-	Iron





## LIST OF SYMBOL/UNITS

Parameters	Symbol	Units
Velocity of Blood	$\mathbf{V}$	cm/s
Velocity of MN	$\mathbf{V}_p$	cm/s
Temperature of Blood	$\bar{T}$	K
Temperature of MN	$\bar{T}_p$	K
Curie Temperature	$\bar{T}_c$	K
Wall Temperature	$\bar{T}_w$	K
Maximum Entrance Blood Velocities	$\bar{u}_r$	cm/s
Maximum Entrance MN Velocities	$\bar{u}_{r1}$	cm/s
Vessel Height	$\bar{h}$	cm
Vessel Length	$L$	cm
Magnetic Field Strength	$\bar{B}$	T
Magnetization	$\bar{M}$	kA / m
Saturation Magnetization	$\bar{M}_{sat}$	kA / m
Particle Magnetization	$m$	kA / m
Distance in x-direction from Magnet	$\bar{a}$	cm
Distance in y-direction from Magnet	$\bar{b}$	cm
Concentration of MN (Fraction)	$C_v$	-
Concentration of MN (in Blood Vessels)	$C_M$	no/m <sup>3</sup>
Concentration of MN (in Membrane)	$C_M$	no/m <sup>3</sup>
Concentration of MN (in Tissue)	$C_M$	no/m <sup>3</sup>
Volume of MN	$V_{vp}$	m <sup>3</sup>
Density of Blood/Water	$\bar{\rho}$	kg/m <sup>3</sup>

Density of Nanofluids	$\bar{\rho}_{nf}$	kg/m <sup>3</sup>
Density of MN	$\bar{\rho}_p$	kg/m <sup>3</sup>
Density of Magnetic-core of MN	$\bar{\rho}_{p(core)}$	kg/m <sup>3</sup>
Density of Drugs	$\bar{\rho}_{drug}$	kg/m <sup>3</sup>
Density of Shell Carrier	$\bar{\rho}_{carrier}$	kg/m <sup>3</sup>
Dynamic Viscosity of Blood/Water	$\bar{\mu}$	kg/ms
Dynamic Viscosity of Nanofluids	$\bar{\mu}_{nf}$	kg/ms
Thermal Conductivity of Nanofluids	$\bar{k}_{nf}$	J/m sK
Thermal Conductivity of Blood/water	$\bar{k}$	J/m sK
Thermal Conductivity of MN	$\bar{k}_p$	J/m sK
Volumetric Coefficient of Thermal Expansion of Nanofluids	$\beta_{nf} \times 10^{-5}$	K <sup>-1</sup>
Volumetric Coefficient of Thermal Expansion of MN	$\beta_p \times 10^{-5}$	K <sup>-1</sup>
Volumetric Coefficient of Thermal Expansion of Water	$\beta_1 \times 10^{-5}$	K <sup>-1</sup>
Heat Capacity of Nanofluids	$\bar{c}_{nf}$	J/kgK
Heat Capacity of Blood/Water	$\bar{c}$	J/kgK
Heat Capacity of MN	$\bar{c}_p$	J/kgK
Electrical Conductivity of the Blood	$\sigma$	S/ m
Electrical Conductivity of the MN	$\sigma_p$	S/ m
Brownian Diffusion	$D_B$	m <sup>2</sup> /s
Scattering Diffusion	$D_S$	m <sup>2</sup> /s
Diffusion Coefficient (in Membrane)	$D_M$	m <sup>2</sup> /s
Diffusion Coefficient (in Tissue)	$D_T$	m <sup>2</sup> /s

Total Diffusion Coefficient (in Blood)	$D_{Tot} = D_B + D_S$	$m^2/s$
Renkin Reduced Diffusion Coefficient	$D$	$m^2/s$
Renkin Reduced Diffusion Coefficient (In Tissue)	$D_\tau$	$m^2/s$
Boltzmann Constant	$k_B$	$m^2 \cancel{kg} / s^2 \cancel{kg}$
Retardation Factor	$r_F$	-
Source Term	$\varphi_s$	$no/s m^3$
Diameter of MN	$\bar{d}$	nm
Diameter of Magnetic-core of MN	$d_m$	nm
Diameter of Endothelial Pores	$\bar{d}_{pore}$	nm
Diameter of drug-loaded MN	$\bar{d}_{mp}$	nm
Diameter of Long Fiber Cylinder	$\bar{d}_f$	nm
Volume Fraction of Tissue Fibers	$\varphi$	-
Specific Volume of the Fiber	$\nu$	$m^3$
Fiber Concentration	$C_F$	$mol/m^3$
Concentration of Drug in Plasma	$\bar{C}_p$	$mol/m^3$
Vasculature Surface Area per unit Volume	$\frac{S}{V}$	$1/m$
Vascular Permeability	$P_i$	$m/s$
Drugs Elimination Constant	$\beta_L$	$1/s$
Osmotic Reflection Coefficient for Drug-loaded MN	$\sigma_f$	-
Volumetric Flow Rates of Blood Plasma	$\varphi_B$	$1/s$

Volumetric Flow Rates of Interstitial Fluids	$\varphi_L$	1/s
Fractional Loading of the Magnetic Therapeutic Drug	$f_1$	-
Magnetic Flux Density Vector	<b>B</b>	T
Strength of Magnetic Field Vector	<b>H</b>	A/m
Vacuum Permeability of Magnetic Field	$\bar{\mu}_0$	H/m
Vacuum Permeability of Electric Field	$\bar{\varepsilon}_0$	F/m
Magnetization	$\bar{M}$	kA/m
Effective Magnetic Susceptibility	$\chi_{eff}$	-
Intrinsic Magnetic Susceptibility of MN	$\chi_2$	-
Magnetic susceptibility of blood	$\chi_1$	-
Drag Force Density	<b>F</b>	N/m <sup>3</sup>
Electric Field Vector	<b>E</b>	N/C
Current Density Vector	<b>J</b>	A/m <sup>2</sup>
Charge Density	$\rho^*$	C/m <sup>3</sup>
Lorentz Force Density	<b>f</b>	N/m <sup>3</sup>
Number of Wires	$N_i$	-
Distance Between the Wires	$\bar{R}$	cm
Intensity of the MF at the Source	$\gamma$	A
Number of Particles per unit Volume	$N$	-
Magnetic Permeability of Vacuum	$\bar{\mu}_0$	Hm <sup>-1</sup>
Heat Transfer Coefficient at the Blood/MN Interface	$h_h$	J/m <sup>2</sup> sK
Average Free Path of MN	$\lambda_a$	nm
Drag Coefficient	$f$	-

Particle Response Time	$\tau_p$	s
Heat Flux	$q_0$	$\text{J}/\text{m}^2\text{s}$
Relaxation to Retardation Time Parameter	$\lambda_1$	-
Retardation Parameter	$\lambda_2$	-
Volume Fraction of MN	$\phi$	-
Pressure	$\bar{p}$	$\text{F}/\text{m}^2$



## CHAPTER 1

### INTRODUCTION

#### 1.1 Introduction

This chapter presents the research background, problem statement, research objectives, scope of study, and importance of the research. The research background describes a summary of the research and discusses the simulation of TMDD. The problem statement describes the gap of the research and the proposed problems. Research objectives motivate the problems solved along with the scope and importance of the research.

#### 1.2 Research Background

Cancer is the leading cause of death worldwide and the disease of multiple etiologies. In stage 4 cancer, cells detach from the main cancerous tumor and go to another part of the body via the bloodstream or lymphatic system, also known as metastasis. They develop new tumors in other parts of the body, which are known as metastatic tumors. The new tumors contained the same type of cancer as the primary tumor has. Cancerous cells have the ability to spread to almost all parts of the body. For example,

1. Breast cancer most likely spread to the bones, lungs, liver, brain, and chest wall.
2. Lung cancer most commonly spread to the liver, bones, brain, and adrenal glands.
3. Prostate cancer has a tendency to move to the bones.
4. Rectal and Colon cancers have a tendency to spread to the lungs and liver.
5. It can spread to the space around the belly, which is called peritoneal carcinomatosis (Ceelen & Levine, 2015).
6. Cancer can also spread to muscle, skin, or other body organs but less frequently.

7. Cancer cells can also move to the lining around the lungs, which is called pleural cavity.

Despite advances in cancer treatment over the previous four decades, cancer detection and treatment continue to be a global healthcare concern (Mukherjee et al., 2020; Sur & Taipale, 2016). According to figures released by the American Cancer Society (ACS) in 2015, the number of cancer cases will rise to 21.8 million new cases by the end of 2030 (Siegel & Jemal, 2015).

The treatment does not cure cancer. It can, however, slow the tumor progression. The main problem of these conventional administered do not reach the actual site of the tumor (Soltani & Chen, 2012). The conventional treatment procedures such as chemotherapy, radiation, photodynamic therapy, hormonal therapy, and surgery, alone or a combination of treatments leave undesirable side effects on the patient. This has led to the urgent need for researchers to model and develop alternative methods for cancer treatment. Therefore, the TMDD has gained noteworthy interest among researchers due to its increased potential for the treatment of cancer and reduction of the side effects (Hamdipoor et al., 2018; Mukherjee et al., 2020).

### **1.2.1 Computational Models for TMDD**

Recent studies show that computational models and numerical simulations contribute significantly to the development of the TMDD (Saadat et al., 2020). Researchers are learning about the structural properties of metastatic tumors in order to improve medicine intake in the desired areas. Personalized computational models for specific forms of cancer and/or for an individual patient have received considerable attention (Shamsi et al., 2018; Kenjereš & Tjin, 2018; Kenjereš, 2008). The behavior of the drug-loaded MN inside the blood vessels is the primary goal of mathematical modeling of TMDD. MN carriers with suitable dimensions can provide applicable solutions for the drug delivery.

However, the thermophysical parameters of the blood change by adding the MN alone or in a mix with the drugs. Consequently, the environment may change drastically as the result. Our research results show that the MN-blood flow behaves differently from

normal blood flow. In particular, when the external magnet is applied, the vorticity of the flow increases. Our conjecture, supported by medical (experimental) research, is that the increased vorticity may harm the patient in the case of a long-term treatment. Thus, it is necessary control the blood flow. Large nanoparticles create a large TMDD zone where the MN flow moves fast to the target area. However, the large MN may damage the blood vessels and cause the blood leakage.

Magnetic hyperthermia, which involves heating MN with an alternating magnetic field, is another emerging cancer treatment approach. Drug compounds are released into the surrounding microenvironment of tumors when MN is heated at the nanoscale. At present, most of the models do not take into account the heating effects of MN. However, several studies have shown the significance of these effects (Clement et al., 2015). Our proposed model shows that under certain conditions, the large MN can cause a temperature increase of up to 2°C (from 37 to 39°C) over a relatively large region inside the vessel. Clearly, such an increase combined with the increased vorticity may lead to a negative impact on the patient (Bose & Banerjee, 2015).

The most important part of the design and mathematical modeling for improved therapeutic drug delivery methods is to get fundamental insights into an underlying principle of MN-blood flow when a strong non-uniform MF exists (Boutopoulos et al., 2020; Bose & Banerjee, 2015). Recent studies (Kenjeres et al., 2018; Russo et al., 2018; Mohammadian & Pourmehran, 2019; Nikookar et al., 2019; Manshadi et al., 2019; Saadat et al. 2020) show a variety of algorithms that are model and designed to solve the drug delivery problems specifically for lungs cancer.

### **1.2.2 Magnetic Force Density on Matter**

Macroscopic matter interacts with an external MF through the motion of free charges (electric currents) and the alignment of microscopic magnetic dipole moments (magnetization).

The total force called Lorentz force, acting on the charged particles is defined as:



$$\mathbf{F} = q(\mathbf{E} + \mathbf{V} \times \mathbf{B}), \quad (1.1)$$

where  $q$  the particles charge, and  $\mathbf{B}$  is the magnetic flux density vector.

Summing up all the charge particles contained in unit volume ( $V$ ) gives rise to the total force ( $\Delta\mathbf{F}$ ) acting on the volume:

$$\Delta\mathbf{F} = \rho^* \int_V (\mathbf{E} + \mathbf{V} \times \mathbf{B}) dV \quad (1.2)$$

where  $\rho^*$  is the charge density,  $\mathbf{J} = \rho^* \mathbf{V}$  is the current density vector.

$$d\mathbf{F} = (\rho^* \mathbf{E} + \mathbf{J} \times \mathbf{B}) dV \quad (1.3)$$

$$\mathbf{f} = \frac{d\mathbf{F}}{dV} = (\rho^* \mathbf{E} + \mathbf{J} \times \mathbf{B}) \quad (1.4)$$

According to Poisson and Maxwell-Ampère equations:

$$\rho^* = \bar{\epsilon}_0 (\nabla \cdot \mathbf{E}), \quad (1.5)$$

$$\mathbf{J} = \frac{1}{\bar{\mu}_0} \nabla \times \mathbf{B} - \bar{\epsilon}_0 \frac{\partial \mathbf{E}}{\partial t}, \quad (1.6)$$

where  $\bar{\epsilon}_0, \bar{\mu}_0$  are the vacuum permeability of electric and magnetic field.

$\rho^*$  and  $\mathbf{J}$  eliminates to:

$$\mathbf{f} = \bar{\epsilon}_0 (\nabla \cdot \mathbf{E}) \times \mathbf{E} + \left( \frac{1}{\bar{\mu}_0} \nabla \times \mathbf{B} - \bar{\epsilon}_0 \frac{\partial \mathbf{E}}{\partial t} \right) \times \mathbf{B}, \quad (1.7)$$

$$\mathbf{f} = \bar{\epsilon}_0 (\nabla \cdot \mathbf{E}) \times \mathbf{E} + \frac{1}{\bar{\mu}_0} (\nabla \times \mathbf{B}) \times \mathbf{B} - \bar{\epsilon}_0 \frac{\partial \mathbf{E}}{\partial t} \times \mathbf{B}, \quad (1.8)$$

The small current-induced due to the motion of charges produced a small magnetic field around itself. Thus, the magnetic Reynolds number is assumed small, and the electric field effect due to charge polarization can be ignored. Therefore, equation (1.8) is reduced as:

$$(\nabla \times \mathbf{B}) \times \mathbf{B} = (\mathbf{B} \cdot \nabla) \mathbf{B} - \frac{1}{2} \nabla B^2 \quad (1.9)$$

Substituting equation (1.9) into (1.8):

$$\mathbf{f} = \frac{1}{\bar{\mu}_0} [(\mathbf{B} \cdot \nabla) \mathbf{B} - \frac{1}{2} \nabla B^2] \quad (1.10)$$

where  $\mathbf{B} = \mu_0 \mathbf{H}$ .

Moreover, since the equilibrium magnetization is collinear with the local MF,  $\mathbf{M} = \left(\frac{M_{sat}}{H}\right) \mathbf{H}$ .  $\mathbf{M}$  is the material magnetization vector. Above certain strength of MF, the material magnetization saturates to a constant value  $M_{sat}$ . From equation (1.10), the Kelvin force takes the form (Tzirtzilakis, 2005):

$$\bar{\mu}_0 (\mathbf{H} \cdot \nabla) \mathbf{H} = \bar{\mu}_0 \left( \frac{1}{2} \nabla (\mathbf{H} \cdot \mathbf{H}) - \mathbf{H} \times (\nabla \times \mathbf{H}) \right), \quad (1.11)$$

or,

$$\bar{\mu}_0 (\mathbf{M} \cdot \nabla) \mathbf{H} = \bar{\mu}_0 \left( \frac{M_{sat}}{H} \right) \left( \frac{1}{2} \nabla (\mathbf{H} \cdot \mathbf{H}) - \mathbf{H} \times (\nabla \times \mathbf{H}) \right), \quad (1.12a)$$

Further simplification results:

$$\bar{\mu}_0 (\mathbf{M} \cdot \nabla) \mathbf{H} = \bar{\mu}_0 \left( \frac{M_{sat}}{H} \right) \nabla H^2 - \bar{\mu}_0 \left( \frac{M_{sat}}{H} \right) \mathbf{H} \times (\nabla \times \mathbf{H}), \quad (1.12b)$$

where  $\mathbf{J} = \nabla \times \mathbf{H}$ ,

$$\bar{\mu}_0 (\mathbf{M} \cdot \nabla) \mathbf{H} = \bar{\mu}_0 \left( \frac{M_{sat}}{H} \right) \nabla \mathbf{H}^2 - \bar{\mu}_0 \left( \frac{M_{sat}}{H} \right) \mathbf{H} \times \mathbf{J}, \quad (1.12c)$$

$$\bar{\mu}_0 (\mathbf{M} \cdot \nabla) \mathbf{H} = \bar{\mu}_0 M_{sat} \nabla \bar{H} - \left( \frac{M_{sat}}{H} \right) (\mathbf{B} \times \mathbf{J}), \quad (1.12d)$$

$$\bar{\mu}_0 (\mathbf{M} \cdot \nabla) \mathbf{H} = \bar{\mu}_0 M_{sat} \nabla \bar{H} + \left( \frac{M_{sat}}{H} \right) (\mathbf{J} \times \mathbf{B}), \quad (1.12e)$$

The first term in equation (1.12d) is FHD and the second is MHD, where  $(\mathbf{B} \times \mathbf{J}) = 0$ .

$$\bar{\mu}_0 (\mathbf{M} \cdot \nabla) \mathbf{H} = \bar{\mu}_0 M_{sat} \nabla \bar{H} = \bar{\mu}_0 \bar{M} \left( \frac{\partial \bar{H}}{\partial x} + \frac{\partial \bar{H}}{\partial y} \right), \quad (1.13)$$

If  $\mathbf{M} = \chi_{eff} \mathbf{H}$ , equation (12a) takes the form:

$$\bar{\mu}_0 (\mathbf{M} \cdot \nabla) \mathbf{H} = \frac{1}{2} \bar{\mu}_0 \chi_{eff} \nabla \mathbf{H}^2, \quad (1.14)$$

### 1.2.3 Magnetic Analysis of Blood

The most basic form of human blood contained three types of cells: red blood cells (RBC) or erythrocytes, white blood cells (WBC) or leukocytes, and blood platelets, all of which are suspended in a solution of three major protein components called blood plasma, which included fibrinogen, albumin, and globulin. Hemoglobin (Hb), an iron porphyrin protein, accounts for over 33% of RBC composition. In our bodies, Hb is primarily bound to Oxygen (O). This protein is responsible for oxygen transport from the lungs to blood vessels and carbon dioxide (CO<sub>2</sub>) transport from blood vessels to the lungs. In an oxygenated state, Hb exhibited the diamagnetic behavior, while it shows paramagnetic nature in deoxygenated state (Pauling & Coryell, 1936; Higashi et al., 1993). The orientation direction of normal erythrocytes in the presence of high MF is independent of the state of Hb in both oxygenated and deoxygenated situations. As they orient (their disk plane axis) parallel to the direction of an applied MF. However, the time it takes for

oxygenated and deoxygenated RBC to orient in the direction of high MF differs, with oxygenated RBC taking a significantly longer time than deoxygenated RBC. Blood flows demonstrate magnetization in the presence of an applied MF, according to the findings. The various properties of blood in mentioned in **Table 1.1**.

**Table 1.1** Various properties of blood.

Properties	RBC	WBC	Platelets	Plasma
Diameters ( $\mu\text{m}$ )	6-7.8	12-17	3.6	-
Magnetic Susceptibility (in Oxygenated)	Diamagnetic Nature ( $\chi_1 < 0$ )	Diamagnetic Behaviour in Plasma ( $\chi_1 < 0$ )	Neutral	Diamagnetic Behaviour ( $\chi_1 < 0$ )
Magnetic Susceptibility (in Deoxygenated)	Paramagnetic Nature ( $\chi_1 > 0$ )	-	Neutral	-

The magnetic susceptibility ( $\chi_1$ ) of RBC depends on the state of RBC as oxygenated and deoxygenated because the magnetic properties of RBC most certainly depend on the state in which Hb is present. If the state of RBC is oxygenated, it is expected to show diamagnetic nature. Otherwise, it is expected to show paramagnetic behavior in deoxygenated state (Haik et al., 1996; Haik et al., 1999).

Tzirtzilakis (2005) mention the value of  $\chi_1$  for oxygenated blood  $\chi_1 = -6.6 \times 10^{-7}$ , while for deoxygenated blood  $\chi_1 = 3.5 \times 10^{-6}$ . The magnetic sensitivity of WBC is unknown. However, some researchers claim that WBC is diamagnetic in plasma, its value is  $\chi_1 = -9.9 \times 10^{-6}$ , while for plasma  $\chi_1 = -7.7 \times 10^{-6}$  (Han & Frazier, 2006; Takayasu et al., 1982). Moreover, WBC is made up of two different elements, which are grouped in

various cells: granulocytes (neutrophil, eosinophil, and basophil), and agranulocytes (lymphocyte and monocyte). The sizes of these elements vary from  $6\mu\text{m}$  to  $15\mu\text{m}$ , and the overall size of WBC is approximately  $17\mu\text{m}$ . Recent research suggests that the blood platelets promote tumor growth and are crucial in cancer spreading. As a result, it (MN coated with platelet membranes) has demonstrated a great capability in eradicating cancer metastases (Geranpayehvaghei et al., 2021; Abrougui et al., 2020). The typical velocity of the blood flow in various blood vessels is given in **Table 1.2**.

**Table 1.2** The realistic velocities of blood flow and its nature in various blood vessels.

Blood Vessels	Vessel Diameters (cm)	Maximum Centerline Blood Velocities (cm/s)	Nature of Blood Fluids
Aorta	2.5	40	Newtonian
Arteries	0.4	10	
Arterioles	0.003	5	Non-Newtonian
Capillaries	0.0007	0.03	
Venules	0.002	1	
Veins	0.5	5	Newtonian
Vena Cava	3	15	

#### 1.2.4 Blood Magnetization

The Ferro Hydro Dynamics (FHD) model predicts that fluids exposed to MF magnetize. Magnetization is a material feature of fluids that determines how magnetized or affected the fluid is in the presence of the MF. The magnetization plays a vital role in the development of the blood vortices during the TMDD (Tzirtzilakis & Loukopoulos, 2005). The magnetization depends on the fluid temperature, density, and strength of MF at

the equilibrium condition. The linear magnetization in the isothermal conditions is given by:

$$\bar{M} = \chi_1 \bar{H}, \quad (1.15)$$

where  $\chi_1$  is the magnetic susceptibility of the blood and  $\bar{H}$  is the strength of magnetic field.

The dependence on the temperature is often approximated by (Matsuki et al., 1977):

$$\bar{M} = \bar{K}\bar{H}(\bar{T}_c - \bar{T}), \quad (1.16)$$

$\bar{K}$  is an experimental constant known as pyromagnetic coefficient, and  $\bar{T}_c$  is the Curie temperature.

The Langevin function describes magnetization of RBC as follows:

$$\bar{M} = mN \left[ \coth \left( \frac{\bar{\mu}_0 m \bar{H}}{k_B \bar{T}} \right) - \frac{k_B \bar{T}}{\bar{\mu}_0 m \bar{H}} \right], \quad (1.17)$$

where  $m$ ,  $N$ ,  $k_B$ , are the particle magnetization, the number of particles per unit volume, and the Boltzmann's constant.

### 1.2.5 Magnetic Field Analysis of Blood

In Bio Fluid Dynamics (BFD) and FHD problems, the MF configuration is the critical factor affecting the vorticity of the blood flow. The BFD problems combine FHD and MHD. The FHD model implies that the fluids subjected to an external MF exhibit magnetization whereas, the MHD model is of an electrically conducting fluid under the impact of the Lorentz force. The FHD is essential for the formation of vortices, while the Lorentz force reduces the blood flow and may suppress the vortex formation (Kenjeres & Tjin, 2018; Kenjeres, 2008; Loukopoulos & Tzirtzilakis, 2004; Tzirtzilakis & Loukopoulos,

2005). For the BFD flow under sharp gradients of the MF, the dominant force is magnetization. Hence, the FDH model applies to this scenario. In particular, this assumption is valid for the blood flow in vessels (10-20 cm) and the MF exceeding 0.5 T (Haik et al., 1999). These assumptions have been discussed in detail by (Tzirtzilakis, 2015).

In the literature, many methods have been applied to simulate the MF. However, the most popular is a simple procedure for the generation of the MF around a set of straight wires based on the Biot–Savart/Ampere’s law. The MF is given by (Kenjeres & Tjin, 2018):

$$\begin{aligned}\bar{B} &= \frac{\bar{\mu}_0 \gamma}{2\pi \bar{R}} \rightarrow \bar{B}_x = -\bar{\mu}_0 \sum_{i=1}^N \frac{(\bar{y} - \bar{b})}{(\bar{x} - \bar{a})^2 + (\bar{y} - \bar{b})^2}, \\ \bar{B}_y &= \bar{\mu}_0 \sum_{i=1}^N \frac{(\bar{x} - \bar{a})}{(\bar{x} - \bar{a})^2 + (\bar{y} - \bar{b})^2}, \\ \bar{B}(\bar{x}, \bar{y}) &= \sqrt{\bar{B}_x^2 + \bar{B}_y^2} = N_i \frac{\bar{\mu}_0 \gamma}{2\pi} \frac{1}{\sqrt{(\bar{x} - \bar{a})^2 + (\bar{y} - \bar{b})^2}},\end{aligned}\tag{1.18}$$

where  $\gamma$  is the magnetic field strength at the source,  $N_i$  the number of wires,  $\bar{R}$  the distance between the wires, and  $\bar{B} = \mu_0 \bar{H}$  is the magnetic field.

The above MF is suitable with the magnetic wire and permanent magnet scenario. Commercial devices, on the other hand, can generate MF with a different geometrical configuration.

### 1.3 Problem Statement

The MN increases the magnetic susceptibility of blood making the impact of the magnetic forces considerable even when the MF is considered relatively weak.

By considering several parameters such as sizes of drug-loaded MN, temperature, and concentration of drugs, the additional drag forces significantly change the complex

pattern of blood flow under a strong non-uniform MF. The existing two-phase models are usually one-way coupled, i.e., the blood flow has an impact on the MN flow. However, the inverse impact of the MN on the dynamics of the blood is not included.

The specific tumor microenvironment depending on the type of cancer and the patient makes it difficult to evaluate. Therefore, combining an external-based approach (various characteristics of a magnet, and therapeutic drugs loaded into the MN) with an internal-based technique (particular tumor site) can improve the drug efficiency.

#### **1.4 Research Objectives**

The goal of this research is to design and develop a computational model for determining the feasibility of delivering therapeutic drugs to the prescribed areas. Thus, for a better understanding of the potential of the TMDD, we simulate the impact of the MN (therapeutic drugs loaded particles and magnetic nanoparticles) on the blood flow. We present a new model based on a new two-phase two-way coupled approach. The main objectives of this research are:

- Study the behavior of the MN (therapeutic drugs loaded particles and magnetic nanoparticles) inside the blood vessels under a strong non-uniform MF.
- Investigate the impact of forces that develop as a result of an external MF. These forces are magnetization, which is caused by the MF orientation of erythrocytes, and Lorentz force, caused by the electric current generated by moving ions in the blood plasma. The MF generates complicated blood flow patterns. The Lorentz force lowers blood flow and suppresses the vortex development, while the magnetization produces vortices. The goal of the study is to simulate these combined effects.
- Investigate the temperature effects of the MF.
- Simulate the efficiency of the TMDD.



### **1.5 Scope of the Study**

In this work, the magnet is represented as a pointwise wire. The vessel walls are represented by a rigid (non-elastic) and non-porous two-dimensional rectangular channel. The large blood vessels such as the aorta, arteries, veins, vena cava are considered, and the blood in these vessels is treated as an incompressible Newtonian fluid. MN is assumed to have a negligible aggregation. Furthermore, the impact of dynamic viscosity is neglected, and the spherical shape of the MN (an important factor) is considered. Due to the small sizes of the particles, particle collisions with walls and particle-particle collisions are not considered in this work.

### **1.6 Importance of the Study**

TMDD is a powerful alternative to conventional drug delivery (Haverkort et al., 2009). Despite the fact that this concept was first proposed in 1960, it was only thoroughly examined in the late 1980s. It has not yet reached clinical use. As discussed earlier in this chapter, that 99% of the drugs administered do not reach the site of the tumor, and only 1% of drugs, or no drug receives by the tumor. Therefore, the tumor regrows (Soltani & Chen, 2012). The conventional procedure leaves undesirable side effects on the patient. This has led to the urgent need for researchers to model and develop alternative methods for cancer treatment. Therefore, the TMDD has gained remarkable interest among researchers due to its potential for the treatment of cancer.

According to data published by Deerasamee et al. (2001), liver, lung, colon/rectum cancers are the most common cancers among men in Thailand, whereas cervix and breast cancers are common in women. According to Agency for Research on Cancer (ARC), lung cancer is leading cancer in both men and women. In 2001, the rate of Cervix cancer was higher than breast cancer in women. Lately, it comes to the second-highest position in 2019 (Virani et al., 2017; Saenrueang et al., 2019).

Thus, as previously stated in this chapter, the global number of cancer cases will increase to 21.8 million new cases by the end of 2030 (Siegel & Jemal, 2015).

- The findings of this study indicate some side-effects that could arise during the treatment
- The model simulates an important impact of the magnet position, the size of drug-loaded MN and the required input of the MN
- The findings also revealed that the combined procedures (external and internal) effectively increased the medication concentration in tumorous locations.



## CHAPTER 2

### LITERATURE REVIEW

#### 2.1 Introduction

In this chapter, a comprehensive review of the computational models to assess the viability and predictability of the TMDD and entropy generation in MDJN is presented. Section 2.2 presents the overview of the TMDD. Section 2.3 presents the literature relevant to TMDD. The importance of MF intensity and various magnet parameters is discussed in Section 2.4. Furthermore, Section 2.5 discusses the significance of mathematical models and numerical simulations. In Section 2.6, the tumor microenvironment to improve therapeutically drugs transport is analyzed. Finally, a detailed discussion on closed-form solutions for the entropy generation in a mixed convection Poiseuille flow of Molybdenum Disulfide Jeffrey nanofluids (MDJN) is presented in Section 2.7.

#### 2.2 Overview

The most effective anti-cancer medications are doxorubicin (DOX) drugs. The usage of these medications results in the death of healthy cells as well. In TMDD, the drug is placed on the MN, injected near the tumor, and absorbed by the tumor through a high gradient MF created by an external or even implanted magnet. The endothelial cells of tumor vasculature are leaky in certain areas, and MNs smaller than these cells can extravasate out of these leaky arteries without harming normal cells.

During conventional delivery, a drug travels through the entire circulatory system of the patient. However, when a high concentration of the drug is required to treat a particular area of the patient's body, e.g. chemotherapy, the procedure may have undesirable side effects. The most sensitive areas are the bone marrow, hair, skin, gastrointestinal organs, and the immune system. Nevertheless, recent studies show that TMDD is a powerful alternative to conventional drug delivery (Haverkort et al., 2009). It

solves the main problem of chemotherapy, which is the inability to deliver the required drugs to the affected areas, reducing the toxic effects. A recent survey Mamun et al. (2020) observes that in TMDD, drug concentrations at the tumor are significantly higher, compared to drugs delivered by systemic delivery methods. Among the blood vessels, TMDD through arteries is particularly useful for cancer therapies. The hepatic artery is used for the treatment of liver tumors (Jeon et al., 2016), the femoral artery is used for treating hind limb tumors (Alexiou et al., 2011), and the carotid artery is used for brain tumor treatment (Chertok et al., 2010).

Although the approach reduces the side effects of anti-cancer treatment, it is a challenging and difficult process (Lee et al., 2017; Luong et al., 2017; Wei et al., 2017, Fernandez et al., 2018; Rosiere et al., 2018; Sun et al., 2018a; Sun et al., 2018b). A weak MF may not achieve the required targeting, whereas a strong MF may cause leakage from the vessels through the internal organs and generate undesirable vorticity which slows down the blood flow to dangerous levels (Widder et al., 1981; Goodwin et al., 2001). The particle size and the intensity of the MF are two important delivery parameters. A strong MF and large particle size may clog the blood vessels while a weak MF may not be able to deliver the drug.

### **2.3 Literature Review of TMDD**

Freeman, Arrott, and Watson first introduced TMDD in 1960. They propose that drug-loaded MN might inject into the blood vessels and attracted by an external magnetic field could be an alternative solution for controlled delivery of therapeutic drugs. Although this method was introduced in 1960 and explored gradually by the late 1980. It has not yet reached a clinical use.

Widder et al. (1981) conducted an experimental study of Yoshida sarcoma tumors in rats. Albumin microspheres (placebo microspheres and microspheres with 0.5 mg/kg doxorubicin) coated by magnetite  $\text{Fe}_3\text{O}_4$  (100-200nm) and doxorubicin (0.5-5 mg/kg) were injected. The external magnet (0.55 T) was held around the tumor for 30 min. The tumors

decreased on average by 83% and no deaths occurred for treated tumors. For placebo-treated animals, there were 80% deaths. The death rate for the third group treated by the same MN without the external magnet was 100%.

Lübbe et al. (1996a) and Lübbe et al. (1996b) conducted the first phase clinical trial of TMDD to deliver the anti-cancer drug 4'-epidoxorubicin to advanced solid tumors for 14 patients. The MN was 50-150 nm in diameter and coated with anhydroglucose polymer on the surface where the drug was reversibly adsorbed. External magnets arranged on the skin close to the tumor provided an MF of 0.5-0.8 T. The results of the treatment were considered positive for 50% of the patients. To improve the results, a stronger MF and larger MN (up to 1  $\mu\text{m}$  in diameter) were suggested. The discussion of these trials is in (Lübbe et al., 2001; Lübbe et al., 1999). Thereafter, Alexiou et al. (2000) and Alexiou et al. (2001) performed another extensive study on squamous cell carcinoma tumors in rabbits. They used MN (50-100 nm) bound with anticancer agents. The MF was increased to 1.0-1.7 T. Accumulation of the chemotherapeutic agents with a permanent remission of the tumors was detected by visual inspection with MRI combined with histology. Goodwin et al. (1999) show experimentally a high concentration of iron/carbon particles of 0.5-5  $\mu\text{m}$  diameters in the targeted areas in animal experiments. However, in many cases, large particles block the vessels causing a hemorrhage. Jain et al. (2003) recommended an MN of about 400-600 nm.

Nacev et al. (2011a), Lübbe & Bergemann (2005), Alexiou et al. (2000), and Alexiou et al. (2001) study TMDD using an advection-diffusion model verified by experimental data. They predict that targeting MN with a 2T MF is possible up to a depth of 20 cm in large blood vessels and up to 30cm in small vessels. The human clinical trials by Lübbe et al. (1996a), Lübbe et al. (2001), and Goodwin et al. (2001) detect the accumulation of MN by visual inspection with MRI (magnetic resonance imaging), combined with histology in vivo. Unfortunately, the quantitative evaluation of the concentration of MN was not performed since the MRI does not have the required resolution. The histology has been performed, but the velocity of the blood flow was not measured. Testing the required MF per nanoparticle relative to the Stokes force was

performed in-vitro and in-vivo experimentally by Widder et al. (1981), Ganguly et al. (2005), Xu et al. (2005), and Alexiou et al. (2000). In-vitro studies (Ganguly et al., 2005; Xu et al., 2005) confirm that the MN are captured even when the centerline DF exceeds the MF. In-vivo studies (Widder et al., 1981; Alexiou et al., 2000) confirm that when the DF exceeds the MF, TMDD is still possible. Nacev et al. (2011a) argue that a simple comparison of the DF and MF is not sufficient to derive a definite conclusion about the possibility of TMDD. Their example is an MF of 0.5 T acting on the MN (250 nm) and a DF which is 7 times higher than the MF. Similar non-trivial experimental results by Alexiou et al. (2000) and Alexiou et al. (2001) imply that the simulation of TMDD requires accurate models to consider the nanoscale effects, DF, the volume fraction, the size of the MN, and the temperature. Moreover, the conventional diffusion-convection approach (Nacev et al., 2011a; Grief & Richardson, 2005) seems to be oversimplistic.

An early work of Sud & Sekhon (1989) uses an analytical model for numerical analysis of the interaction between the MF and the blood flow in the multi-branching arterial system. Their results demonstrate that the rate of blood flow through the system was reduced by the MF. Kinouchi et al. (1996) include the Lorentz force into the Navier–Stokes equations. Their finite-element solution shows a reduction of the blood flow by 5–10% under a strong MF.

## **2.4 Magnet and Magnetic Fields**

To date, TMDD has been limited to either using external permanent magnets to target shallow tumors (Wilson et al., 2004; Liu et al., 2010; Raut et al., 2010; Pouponneau et al., 2011; Krukemeyer et al., 2012) or to implanting magnetic materials (wires, seeds, stents) to reach a deep tumor (Fernandez-Pacheco et al., 2007; Forbes et al., 2008, Cregg et al., 2012). Magnetic implants are promising for treating bone cancer. They can also be embedded in fatty tissue to treat obesity (Saatchi et al., 2017) and in the inner ear to treat deafness (Le et al., 2017). However, they are not suitable for every patient and every clinical condition. Potentially harmful procedures are often required for placing such

magnets (Donson, 2006). Therefore, the applications of these procedures remain limited (Hayden & Hafeli, 2006; Shapiro, 2009; Cao & Han, 2011).

Lübbe et al. (1996a), Nacev et al. (2011a, 2011b) and Nacev et al. (2015) use strong permanent magnets (20×40 cm) to reach deep tumors. A magnet is placed outside the patient's body up to 15 cm from the tumor, to create an appropriate MF. Several authors propose that a permanent magnet shaped as a solid cylinder or rectangle can produce the required MFs. Superparamagnetic particles constitute another solution (Kayal et al., 2011; Nacev et al., 2015; Rukshin et al., 2017; Sharifi et al., 2019).

To determine particle deposition efficiency, several CFD models have been developed. Several parameters have been analyzed to improve the deposition efficiency, including the MN size, magnet shapes such as wedge-shaped permanent magnets, rectangular coil magnets, magnet location, magnetic field strength, tube diameter, flow rate, and so on. (Xie et al., 2010; Pourmehran et al., 2016; Kenjeres et al., 2018; Russo et al., 2018; Mohammadian & Pourmehran, 2019; Nikookar et al., 2019; Saadat et al., 2020; Wang et al., 2020). It has been shown that increasing the size of the magnet (H=4 cm, D=2 cm) increases the deposition efficiency by 75.8% (Manshadi et al., 2019). Furthermore, doubling the magnetic field intensity from 0.25 to 1.25 T improved the efficiency of the delivery by 29%.

## 2.5 Numerical Simulation of TMDD

An early BFD model was introduced by Haik et al. (1996) and Haik et al. (1999). The model, including Ferro Hydro Dynamics (FHD) and Magnetic Hydro Dynamics (MHD), has been solved numerically and verified by experiments. The fluid exhibits magnetization and vortices generated by the external MF. However, the blood flow has been significantly slowed down. Loukopoulos & Tzirtzilakis (2004) present a viscous, steady-state two-dimensional, incompressible, laminar model (BFM) of a flow between two parallel plates. The FHD and magnetization are functions of the temperature. The energy equation includes the magnetocaloric effect. In particular, the model simulates a

vortex formed near the lower wall close to the operating magnetic device. Grief & Richardson (2005) propose a convection-diffusion model, which includes interactions and collisions between the red blood cells. The model includes Brownian diffusion, shear diffusion, and convection. Bali and Awasthi (2007) present graphically the velocity resistance to the blood flow for different MFs. Tzirtzilakis & Loukopoulos (2005) analyze a one-phase FHD/MHD steady-state finite-difference numerical model with an external MF. The model generates two vortices rotating in opposite directions. The vortices appear even for relatively small magnetic numbers such as  $M_{nF} \approx 100$ . The assumed MF is 8 T. The authors observe that in TMDD, a similar flow is generated by 1 T. Following this estimate, the forthcoming numerical experiments consider an MF in the range of 0.5-1 T.

Tzirtzilakis (2005) reports a 3D model consistent with the FHD and MHD, i.e., including magnetization and electrical conductivity of the blood. The application is a laminar, incompressible, three-dimensional, viscous flow of a Newtonian BMF. Blood is in a rectangular duct under a spatially varying MF. Note that a sharp MF generated by a magnetic wire allows neglecting the Lorentz force. For the BMF flow under sharp gradients of the MF in large blood vessels, the dominant force is magnetization. Hence, the FDH model applies to this scenario. In particular, this assumption is valid for the blood flow in vessels (10-20 cm) and the MF exceeding 0.5 T (Haik et al. 1999). These assumptions have been detailed by Tzirtzilakis (2015). Kenjereš (2008) and Kenjereš & Righolt (2012) present a numerical simulation of TMDD in a complex vascular system of a brain by a non-Newtonian model. The MN flow is simulated by the Lagrangian tracking of the spherical double-layer MN under the imposed MF across the arterial walls. The particles are characterized by the diameter of the outer and inner magnetic cores. The MN equation is coupled with the momentum equation of the blood flow, whereas the momentum equation for the blood flow is independent. Kenjereš (2014) develops another version of the model to simulate the local deposition of a low-density lipoprotein. The model shows promising results, i.e., in some cases the TMDD is ten-fold relative to the conventional delivery. Numerical simulation of TMDD in aerosols in the human upper and central respiratory systems under a non-uniform MF is presented by Kenjereš & Tjin (2017) and Rukshin et



al. (2017). The MN are tracked in the Lagrangian frame. The model estimates the distribution of the MN under a strong MF. Yue et al. (2011) develop a 3D model of a superparamagnetic cluster suspended in a Poiseuille flow. Their model includes the Stokes drag force, MF, and gravity. The numerical model of Habibi & Ghasemi (2011) shows a circulation in the region covered by the MF. Under certain conditions, the absorption of the 200-nm MN decreases significantly compared to 2000-nm particles since the MF is too weak to overcome the DF. However, this is not always the case since the TMDD also depends on the concentration of the MN and the strength of the magnet.

One-way coupled MN delivery model has been used for the stenosis aortic and vessel bifurcations by Larimi et al. (2014). Lagrangian particle tracking is performed. The numerical results show that the MF increases the volume fraction of the particles in the target region. However, for high Reynolds numbers the efficiency of the TMDD is low. Kandelousi & Ellahi (2015) apply the lattice-Boltzmann method. The results show that the MF affects the flow considerably. A backflow occurs near the MF region. However, a recent survey (Said et al., 2021) suggests that the single-phase method suffers from a lack of precise simulations of thermophysical features related to nanofluids.

Bose & Banerjee (2015) propose a two-phase one-way 2D model. The trajectories of the particles are obtained in the Lagrangian frame. The force balance equates the particles to the DF, magnetic force, the buoyancy force, the Brownian force, and the thermophoretic force. The external MF creates a strong recirculation zone near the location of the insert.

Tzirtzilakis (2015) presents a BFD/FHD model in an aneurysm. The blood is an electrically non-conducting, homogeneous, non-isothermal Newtonian magnetic fluid. The paper presents an analysis of the effects of the MF on the blood that may or may not include MN.

The solution includes the stream function-vorticity formulation. The curvilinear grid is obtained by a variant of the grid stretching adapted to the MF by the algebraic grid generation (Gordon & Thiel, 1982). Alshare & Tashtoush (2016) simulate

magneto-hemodynamics in stenosed arteries. Doubling the MF from 4 to 8 T increases the pressure drop by nearly 15%, but has a negligible impact on the wall shear stress. TMDD of pharmaceutical aerosols in the human upper and central respiratory is analyzed in (Kenjereš & Tjin, 2017). The airflow dynamics equations are based on the Eulerian approach, whereas the dynamics of the MN-phase are represented in the Lagrangian frame. The deposition of the drug can be significantly enhanced by the MF. The most effective enhancement has been observed for  $5 \times 10^{-4} \leq St \leq 10^{-1}$  with particles of diameter 0.3 and 5  $\mu\text{m}$ .

An interesting single-phase model of the nanofluid flow is designed to simulate the irrigation of a root canal in the human tooth as proposed by Ghalandari et al. (2019). An analytical single-phase model of the blood flow mixed with copper nanoparticles with a magnetic field is proposed in (Umadevi, 2021).

A recent two-phase model of TMDD for solid-liquid coupled BFD has been reported by Boutopoulos et al. (2020). The focus of their paper is an injection of MN in different locations of the artery. The model is based on the Navier-Stokes equations for the blood flow and the advection-diffusion equation for the MN. The experiments include different injecting scenarios. The model is one-way coupled, i.e., the blood flow affects the MN via the corresponding convection-diffusion terms. However, the MN does not have an impact on the blood flow. Therefore, the model is not capable of analyzing the possible impact of the size of the MN on the characteristics of the blood flow. Their model does not include the energy equation. Therefore, the analysis of the impact of the concentration and the size of the MN on the temperature of the blood flow is excluded.

This dissertation introduces a numerical, solid-liquid two-phase Euler-Euler BFD model. The governing equations include continuity, momentum, and temperature equations for blood and MN for a two-phase (solid-liquid) flow in a 2D rectangular channel. The problem is governed by coupled momentum and temperature equations of the blood flow and the MN. The numerical procedure invokes the stream function–vorticity formulation and an efficient numerical method on a finite-difference grid.

The model has been analyzed with reference to single-phase models (Tzirtzilakis, 2008; Bianco et al., 2009) and a two-phase model (Boutopoulos et al., 2020). Note that the two-phase model is based on balancing the hydrodynamic and magnetic forces, i.e.,  $v_p = v + v_{mag}$ , where  $v$  is the velocity of the fluid and  $v_{mag}$  is evaluated using the Stokes' drag law. In other words, the corresponding continuity, momentum, and energy equations of the solid phase are not included. In contrast, the proposed model includes the MN having a two-way momentum exchange. This includes the reverse impact of the MN on the blood flow. In particular, it is possible to analyze the impact of the size and the concentration of the MN on the blood flow. This simulates the vortices of the MN and the blood flow, independently. It has been shown that under certain conditions, the geometric structure of the MN flow is drastically different from that of the blood flow. Simulation of these effects is possible only with the proposed two-way coupled, two-phase model and its possible extensions. The formation, velocity, and size of the vortices have been evaluated and discussed.

The obtained result shows that the additional Lorentz force (MHD) reduces blood flow and suppresses the large vortices created by FHD flows. The MN flow, on the other hand, is not significantly affected, despite a minor disturbance. Another important result is therapeutic drug concentration. It has been observed that as we increase the drug concentration from 30% to 50%, the size of the vortices increases. The difference is insignificant when  $d=250$  nm. However, the TMDD zone grew dramatically when the size of MN (20,000) was increased while keeping the drug concentration as 50%.

It has been demonstrated that the size of the MN has an impact on the temperature of the blood. Under certain conditions, the MF acting on MN increases the blood temperature up to 2.1°C i.e. from 37 to 39.1°C. This cannot be simulated using the preceding one-way coupled single or double-phase models. Finally, a variety of engineering methodologies can be adapted to the simulation of TMDD. Recent surveys (Alsabery et al., 2020; Baghban et al., 2019; Granados-Ortiz et al., 2021; Afshari et al., in print) show a variety of algorithms that are designed to solve specific engineering problems. However,

the different temporal and spatial scales of the medical and engineering applications must be taken into account.

## 2.6 Tumor Microenvironments

One of the major issues of the MTDD is a necessary concentration of MN in case of a tumor located far from the magnetic source (deep tumor). The complex geometry of the tumor is an additional difficulty encountered by the MTDD treatment. As opposed to a healthy tissue, which is a fine network of capillaries, the region around the tumor is often characterized by irregular and poor blood supply that lessens the MTDD (Fukumura & Jain, 2007; Burke et al., 2000; Tozer et al., 2005).

The varieties of parameters having an impact on the MTDD are not fully understood (Burke et al., 2000; Gray et al., 1953). A particular drawback of the MN is the large size of the molecules, which are unable to diffuse through the tissue (Fournier, 2017; Saltzman, 2001).

The metastasis mentioned in Chapter 1 is a type of cancer in which the metastatic tumor has the same type of cancer as the primary tumor and requires the same treatment.

Nevertheless, it is difficult to specify the type of treatment required for metastatic tumors. All types of cancer cells can spread. It depends on a number of circumstances, including the type of cancer and how rapidly it grows. A metastatic tumor is made of a diverse set of extracellular, leaky vasculature, pathological, nonfunctional lymphatics, and structural features, which make them a challenging place for therapeutic drugs penetration.

Nacev et al. 2011b & 2013 analyze the range of MN diffusivity and the tissue resistance within the metastatic tumors using the Fiber-Matrix model and the Renkin Pore model. They found that metastatic breast cancers had a lower number of blood vessels, accumulated in irregular clusters that damaged the liver, and had a large distance between the nearest blood vessels. The TMDD through the dense extracellular networks is less

efficient than through the normal vessels (Fournier, 2017). Thus, the tissue morphology affects both the diffusion and convection.

Despite advances in the treatment of metastasis, many types of cancers remain a significant challenge, e.g., peritoneal carcinomatosis (Ceelen & Levine, 2015). Treatment by an intraperitoneal chemotherapy chemoperfusion is simulated by the convection-diffusion model in (Dewhirst & Secomb, 2017).

However, the complexities of the tumor and the nonfunctional lymphatics account for the additional difficulties for the convective-diffusive models (Chauhan et al., 2011; Au et al., 2016). The tumor growth compresses the lymphatic vessels at the center of the tumor that makes them unable to function properly (Padera et al., 2004; Jain et al., 2014). Due to interstitial fluids pressure the velocity of the fluid is close to zero at the center of the tumor (Dewhirst & Secomb, 2017; Soleimani et al., 2018; Chauhan et al., 2011; Liu et al., 2011). Soltani & Chen, 2012 conclude that 99% of the drugs administered do not reach the site of the tumor.

We assume that the volumetric flow rates of blood plasma and interstitial fluids out of the lymphatic vessels per unit volume of the tumor media are zero due to the complexity of tumor media and nonfunctional lymphatics. Moreover, the specific tumor microenvironment is difficult to quantify depending on the type of cancer and varies on the patient-to-patient conditions. Therefore, the external-based techniques would be more beneficial in regulating therapeutic effectiveness.

Dynamic Magnetic Shift (DMS) method has been developed to improve the therapeutic drug penetration in metastatic cancer (Nacev et al., 2011b, 2013). By adjusting the direction of the MF, they improve the convective mobility of MN. It has been concluded that the DMS might be useful in facilitating the therapeutic MN to reach poorly vascularized areas of metastatic tumors that are difficult to reach by diffusion alone. Shamsi et al. (2018) show that the successful TMDD to large tumors (5–10 mm) depends on the MF and the magnet-tumor distance, whereas these two parameters are less important

for delivery to small tumors (1-4 mm). The MN 200-300 nm work the best for the large tumors whereas for the small tumors the preferred size is 100-500 nm.

Yang & Vafai (2006) develop a model designed for a low-density lipoprotein (LDL) transport in the arterial wall coupled with the mass transport in the arterial lumen. This study analyzes the transmural transport in the onset and progression of atherosclerosis, as well as factors responsible for an increased arterial wall uptake of the LDL in hypertensive patients. Kenjeres (2014) proposes a model of the blood flow within a diseased (advanced atherosclerosis stage) carotid artery.

## 2.7 Entropy Generation in MDJN

Viscoelastic Jeffery fluids (JFs) belong to a rare type of the non-Newtonian fluids, which exhibit viscosity and elasticity at the same time. The JF becomes Newtonian when the relaxation and retardation times are negligible (Jena et al., 2016).

A Jeffery Nanofluids (JN) is characterized by a high heat transfer rate, and is becoming increasingly important in polymer, solution and metal industries. Furthermore, the nanofluids can be classified as Newtonian or non-Newtonian depending on the volume fraction, and characteristics of the nanoparticles: material, shape, size, etc. (Das et al., 2008).

Molybdenum Disulfide ( $\text{MoS}_2$ ) is a semiconductor inorganic compound having alternate layers of molybdenum and sulfur atoms. The compound, which is unreactive and unaffected by oxygen, is widely used as industrial lubricant. Important experimental research on the homogenous stable Newtonian  $\text{MoS}_2$  nanofluid is performed by Zhang et al. (2012). Physical properties of  $\text{MoS}_2$  are experimentally analyzed by (Gu et al., 2013; Kato et al., 2003; Zhang et al., 2012; Mao et al., 2014; Shen, 2008; Su et al., 2015; Zhang et al., 2016; McBride et al., 1976; Liu et al., 2014; Ding et al., 2015; Benavente et al., 2004). Mathematical models of Newtonian nanofluid (NN) are researched by Aaiza et al. (2015a), and Aaiza et al. (2015b).

Entropy generation is an important characteristic of a nanofluid. The entropy generation in micro channel steady-laminar forced-convection fluid flow is studied by Haddad et al. (2004). Mahmud & Fraser (2005) analyze the entropy generation in a porous channel with viscous dissipation. The entropy generation in a magnetohydrodynamic flow due to a rotating porous disk in a nanofluid is simulated by Rashidi et al. (2013). A comprehensive review of the entropy generation in a nanofluid is Mahian et al. (2013). Dalir (2014), provide a numerical solution for the entropy generation problem in a JF over a stretching sheet. Ellahi et al. (2016) present a model of an HFE-7100 nanofluid with varying shapes of the nanoparticles.

However, to the best of our knowledge, closed form solutions for entropy generation in a mixed convection Poiseuille flow of MDJN have not been reported. Therefore, we present an analytical approach to study a water-based MDJN. The effects of radiation on mixed convection are analyzed. Approximate solutions for the velocity and temperature are obtained. Graphs of the entropy, velocity and temperature display the relative impact of the input parameters. A JN has been compared with a second grade nanofluid (SGN) and a NN.

## CHAPTER 3

# A TWO-PHASE, TWO-WAY COUPLED MODEL OF TARGETED MAGNETIC DRUG DELIVERY FOR SMALL REYNOLDS NUMBERS

### 3.1 Introduction

In this chapter, the behavior of magnetic nanoparticles in a blood vessel is simulated by a two-phase (solid-liquid) flow in a 2D rectangular channel. The problem is governed by coupled momentum and temperature equations for the blood flow and for the MN. The numerical procedure invokes the stream function–vorticity formulation and an efficient numerical method on a finite-difference grid. The model, validated by experimental results, has been applied to analyze the formation of vortices relative to the magnetic force and the drag force, and the zones of TMDD where the velocity of the blood flow is low and the velocity of the MN flow is high toward the magnet. The model is capable of simulating the (reverse) impact of the MN on the blood flow, to evaluate the corresponding changes in the vorticity. The number, the size and the strength of the resulting vortices can be evaluated subject to the strength of the MF and the position of the magnet.

### 3.2 Mathematical Formulation

In this section a mathematical formulation for the drug-loaded MN transport in the blood vessel is given.



### 3.2.1 Governing Equations

Consider a viscous, unsteady, two-phase (two-way coupled) flow consisting of the MN and the blood in a 2D rectangular channel with length  $\bar{L}$  and height  $\bar{h}$  (**Figure 3.1**). The flow is assumed to be fully developed at the entrance of the channel. The upper and lower walls have a constant temperature. The magnetic source is a magnetic wire placed perpendicular to the  $(x,y)$ -plane at the point  $(a,b)$  near the lower wall. The governing equations of the two-phase flow are given with regard to the velocity  $\mathbf{V} = (\bar{u}, \bar{v})$  and the temperature  $\bar{T}$  of the blood and the particles. The subscript  $p$  indicates the parameters of the MN flow.

$$\nabla \cdot \mathbf{V} = 0, \quad (3.1)$$

$$\bar{\rho} \left( \frac{\partial \bar{u}}{\partial t} + \mathbf{V} \cdot \nabla \mathbf{V} \right) = -\nabla \bar{p} + \bar{\mu} \nabla^2 \mathbf{V} + \mathbf{F} + \bar{\mu}_0 \bar{M} \nabla \bar{H}, \quad (3.2)$$

$$\bar{\rho} \bar{c} \left( \frac{\partial \bar{T}}{\partial t} + \mathbf{V} \cdot \nabla \bar{T} \right) + \bar{\mu}_0 \bar{T} \frac{\partial \bar{M}}{\partial \bar{T}} \mathbf{V} \cdot \nabla \bar{H} = \bar{k} \nabla^2 T + \bar{Q}_p, \quad (3.3)$$

where the drag  $\mathbf{F}$  is given by:

$$\mathbf{F} = C_v \bar{\rho}_p \bar{F}_D (\mathbf{V}_p - \mathbf{V}), \quad (3.4)$$

and

$$\bar{Q}_p = C_v \bar{\rho}_p \bar{c}_p \bar{h}_v (\bar{T}_p - \bar{T}). \quad (3.5)$$

The solid phase, i.e., the MN in blood is simulated by the momentum and energy equations, assuming that the impact of the dynamic viscosity is negligible. The MN are assumed to be spheres with a uniform size and density. The fluid and the solid phases are electrically non-conductive. Therefore, the MF term is included in the momentum

equations (Nacev et al., 2011; Kenjereš & Tjin, 2017). The temperature of the fluid and the MN are affected by the MF and vice versa. Hence, the solid phase equations are given by:

$$\nabla \cdot \mathbf{V}_p = 0, \quad (3.6)$$

$$\bar{\rho}_p C_v \left( \frac{\partial \mathbf{V}_p}{\partial t} + \mathbf{V}_p \cdot \nabla \mathbf{V}_p \right) = -(1 - C_v) \mathbf{F} + C_v \bar{\mu}_0 \bar{M} \nabla H, \quad (3.7)$$

$$\bar{\rho}_p \bar{c}_p C_v \left( \frac{\partial \bar{T}_p}{\partial t} + \mathbf{V}_p \cdot \nabla \bar{T}_p \right) + C_v \bar{\mu}_0 \bar{T}_p \frac{\partial \bar{M}}{\partial \bar{T}_p} \mathbf{V}_p \nabla \bar{H} = -(1 - C_v) \bar{Q}_p, \quad (3.8)$$

where  $\bar{p}$  is the pressure,  $\bar{\rho}$  the density,  $\bar{\mu}$  the dynamic viscosity,  $\bar{c}$  the heat capacity,  $\bar{k}$  the thermal conductivity,  $C_v$  is the concentration of MN in the blood, and  $\bar{\mu}_0 = 4\pi \times 10^{-7} \text{ Hm}^{-1}$  is the magnetic permeability of vacuum (Rosen, 2004).

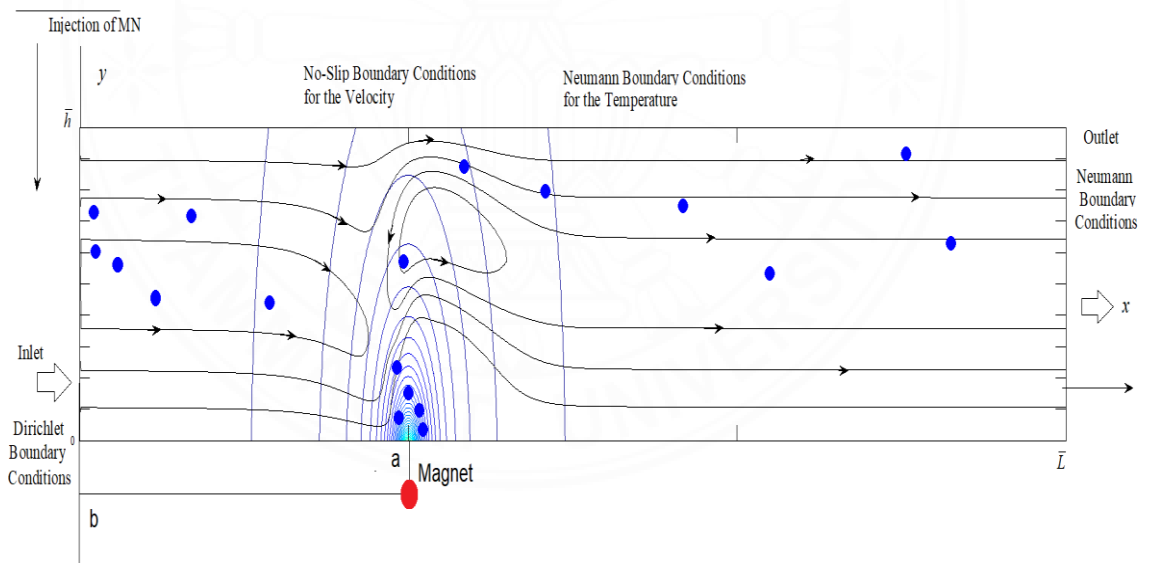


**Figure 3.1** Flow domain and boundary conditions.

The additional term  $\bar{\mu}_0 \bar{M} \nabla \bar{H}$  in the momentum equation is the MF per unit volume, whereas  $\bar{\mu}_0 \bar{T} \frac{\partial \bar{M}}{\partial \bar{T}} \mathbf{V} \cdot \nabla \bar{H}$  is the thermal power per unit volume due to the magnetocaloric effect.

### 3.2.2 Magnetic Field

Following Tzirtzilakis (2008) and Tzirtzilakis (2015) we consider a magnetic source (a current-carrying wire conductor) positioned perpendicular to the  $(x, y)$  plane.  $\bar{H}$  denotes the intensity of the MF given by:

$$\bar{H} = \sqrt{\bar{H}_x^2 + \bar{H}_y^2} \quad (3.9)$$

$\bar{M}$  is magnetization, approximated by (Matsuki et al, 1977).

$$\bar{M} = \bar{K} \bar{H} (\bar{T}_c - \bar{T}), \quad (3.10)$$

$\bar{K}$  is an experimental constant, and  $\bar{T}_c$  is the Curie temperature.

Following Tzirtzilakis (2008) and Tzirtzilakis (2015), we consider a magnetic source (a current-carrying wire conductor) positioned perpendicular to the  $(x, y)$  plane. The wire is at position  $(a, b)$  below the lower wall (**Figure 3.1**). The strength of the MF is defined by the magnetic induction given by  $\bar{B}(\bar{x}, \bar{y}) = \mu_0 \tilde{H} \equiv \mu_0 (\bar{H}_x, \bar{H}_y)$  (Tzirtzilakis, 2005), where:

$$\bar{H}_x = \frac{\gamma}{2\pi} \frac{(\bar{y} - \bar{b})}{(\bar{x} - \bar{a})^2 + (\bar{y} - \bar{b})^2}, \quad \bar{H}_y = -\frac{\gamma}{2\pi} \frac{(\bar{x} - \bar{a})}{(\bar{x} - \bar{a})^2 + (\bar{y} - \bar{b})^2}, \quad (3.11)$$

and where  $\gamma$  is the intensity of the MF at the source and  $(\bar{a}, \bar{b})$  is the position of the source.

### 3.2.3 Drag coefficient

Following (Bianco et al., 2009), the Stokes' resistance law for small  $\text{Re}_p$  and sub-micrometer particles is given by:

$$\bar{F}_D \approx f \frac{1}{\tau_p} = \frac{18\bar{\mu}}{d^2 \bar{\rho}_p C_c}, \quad (3.12)$$

where  $d$  is the diameter of the particle,  $f$  is the drag coefficient, and  $\tau_p$  is the particle response time. The Cunningham correction coefficient is given by:

$$C_c = 1 + \frac{2\lambda_a}{d} \left( 1.257 + 0.4e^{\frac{11d}{\lambda_a}} \right). \quad (3.13)$$

where  $\lambda_a$ , is the particle mean free path of the particles.

Further,

$$\text{Re}_p = \frac{d\bar{\rho}}{\bar{\mu}} \tilde{u}_0, \quad (3.14)$$

where  $\tilde{u}_0$  (tilde) denotes the average, and index 0 refers to the inlet boundary.

The drag coefficient is defined by:

$$f = \begin{cases} 1 & \text{if } \text{Re}_p \leq 1 \\ \text{Re}_p^{0.354} & \text{if } 1 < \text{Re}_p < 400 \end{cases} \quad (3.15)$$

### 3.2.4 Heat Transfer coefficient

The energy equation for spherical MN is given by  $\bar{h}_v = \frac{6\bar{h}_h}{d}$ , where  $\bar{h}_h$  is the heat transfer coefficient at the blood/MN interface (Ranz & Marshall 1952).

The Nusselt number  $Nu_p$  is given by (Ranz & Marshall 1952).

$$Nu_p \equiv \frac{\bar{h}_h d}{\bar{k}} = 2.0 + 0.6 Re_p^{1/2} Pr^{1/3}. \quad (3.16)$$

Hence,  $\bar{h}_h = \frac{\bar{k}}{d} (2.0 + 0.6 Re_p^{1/2} Pr^{1/3})$ .

### 3.3 Boundary and Initial Conditions

The boundary conditions are given by

$$\text{Inflow} \quad \bar{x} = 0, 0 \leq \bar{y} \leq \bar{h} : \quad \bar{u} = \bar{u}_p = \bar{u}_0(\bar{y}), \bar{v} = \bar{v}_p = 0; \bar{T} = \bar{T}_p = 37^0 C. \quad (3.17)$$

$$\text{Outflow} \quad \bar{x} = \bar{L}, 0 \leq \bar{y} \leq \bar{h} : \quad \frac{\partial \bar{R}}{\partial \bar{x}} = 0, R = \bar{u}, \bar{v}, \bar{T}, \bar{u}_p, \bar{v}_p, \bar{T}_p. \quad (3.18)$$

$$\text{Upper Boundary} \quad \bar{y} = \bar{h}, 0 \leq \bar{x} \leq \bar{L} : \quad \bar{u} = \bar{u}_p = 0; \bar{v} = \bar{v}_p = 0; \frac{\partial \bar{T}_w}{\partial \bar{y}} = \frac{\partial \bar{T}_p}{\partial \bar{y}} = 0. \quad (3.19)$$

$$\text{Lower Boundary} \quad \bar{y} = 0, 0 \leq \bar{x} \leq \bar{L} : \quad \bar{u} = \bar{u}_p = 0; \bar{v} = \bar{v}_p = 0; \frac{\partial \bar{T}_w}{\partial \bar{y}} = \frac{\partial \bar{T}_p}{\partial \bar{y}} = 0 \quad (3.20)$$

Initial Conditions

$$0 \leq \bar{x} \leq \bar{L}, 0 \leq \bar{y} \leq \bar{h} : \quad \bar{u} = \bar{v} = 0; \bar{u}_p = \bar{v}_p = 0; \bar{T} = \bar{T}_p = 37^0 C. \quad (3.21)$$

### 3.4 Dimensionless Equations

The following dimensionless variables are introduced.

$$\begin{aligned}
u &= \frac{\bar{u}}{\bar{u}_r}, \quad v = \frac{\bar{v}}{\bar{u}_r}, \quad \xi = \frac{\bar{x}}{h}, \quad \eta = \frac{\bar{y}}{h}, \quad t = \frac{\bar{t}\bar{\mu}}{\bar{\rho}\bar{h}^2}, \quad t_1 = \frac{\bar{t}_1\bar{\mu}}{\bar{\rho}d^2}, \quad p = \frac{\bar{p}}{\bar{\rho}\bar{u}_r^2}, \quad u_p = \frac{\bar{u}_p}{\bar{u}_{r1}}, \\
v_p &= \frac{\bar{v}_p}{\bar{u}_{r1}}, \quad H = \frac{\bar{H}}{\gamma}, \quad \bar{T}_p = (\bar{T}_p - \bar{T}_0) \frac{\bar{k}}{\bar{q}_0\bar{h}}, \quad T = (\bar{T} - \bar{T}_0) \frac{\bar{k}}{\bar{q}_0\bar{h}}.
\end{aligned} \tag{3.22}$$

$\bar{T}_0$  is the temperature of MN at the channel inlet,  $\bar{q}_0$  is the heat flux, and the other notations are self-explanatory.

Introduce the vorticity function  $J(\xi, \eta)$  and the stream function  $\psi(\xi, \eta)$  as follows.

$$\begin{aligned}
J(\xi, \eta) &= \frac{\partial v}{\partial \xi} - \frac{\partial u}{\partial \eta}, \quad J_p(\xi, \eta) = \frac{\partial v_p}{\partial \xi} - \frac{\partial u_p}{\partial \eta}, \\
u &= \frac{\partial \psi}{\partial \eta}, \quad u_p = \frac{\partial \psi_p}{\partial \eta}, \quad v = -\frac{\partial \psi}{\partial \xi}, \quad v_p = -\frac{\partial \psi_p}{\partial \xi}.
\end{aligned} \tag{3.23}$$

The pressure is eliminated from Equation (3.2). Substituting Equation (3.23) into Equations (3.1)-(3.3) and (3.6)-(3.8) yields:

$$\frac{\partial^2 \psi}{\partial \xi^2} + \frac{\partial^2 \psi}{\partial \eta^2} = -J, \tag{3.24}$$

$$\frac{\partial^2 \psi_p}{\partial \xi^2} + \frac{\partial^2 \psi_p}{\partial \eta^2} = -J_p, \tag{3.25}$$

$$\begin{aligned}
\frac{\partial J}{\partial t} &= \frac{\partial^2 J}{\partial \xi^2} + \frac{\partial^2 J}{\partial \eta^2} - \text{Re} \left( \frac{\partial J}{\partial \xi} \frac{\partial \psi}{\partial \eta} - \frac{\partial J}{\partial \eta} \frac{\partial \psi}{\partial \xi} \right) + C_v \beta_1 D_p \text{Re} (U_2 J_p - U_2^2 J) + \\
&\quad M_{\text{nf}} \text{Re} H \left( \frac{\partial H}{\partial \xi} \frac{\partial T}{\partial \eta} - \frac{\partial H}{\partial \eta} \frac{\partial T}{\partial \xi} \right),
\end{aligned} \tag{3.26}$$

$$\begin{aligned} \frac{\partial J_p}{\partial t} = & -\text{Re}_p d_o \left( \frac{\partial J_p}{\partial \xi} \frac{\partial \psi_p}{\partial \eta} - \frac{\partial J_p}{\partial \eta} \frac{\partial \psi_p}{\partial \xi} \right) - (1 - C_v) \text{Re}_p d_o \beta_1 (U_2 J_p - U_2^2 J) + \\ & \text{Re}_p d_o M_{\text{nf}_p} H \left( \frac{\partial H}{\partial \xi} \frac{\partial T_p}{\partial \eta} - \frac{\partial H}{\partial \eta} \frac{\partial T_p}{\partial \xi} \right), \end{aligned} \quad (3.27)$$

$$\begin{aligned} \text{Pr} \frac{\partial T}{\partial t} = & \frac{\partial^2 T}{\partial \xi^2} + \frac{\partial^2 T}{\partial \eta^2} - \text{PrRe} \left( \frac{\partial T}{\partial \xi} \frac{\partial \psi}{\partial \eta} - \frac{\partial T}{\partial \eta} \frac{\partial \psi}{\partial \xi} \right) + \\ & \text{RePr} C_v D_p \gamma_p \beta_2 (u_{r2} T_p - u_{r2}^2 T) + M_{\text{nf}} \text{PrReEc} H T_p \left( \frac{\partial H}{\partial \xi} \frac{\partial T_p}{\partial \eta} - \frac{\partial H}{\partial \eta} \frac{\partial T_p}{\partial \xi} \right) + \\ & \text{PrRe} \left\{ \left( \frac{\partial^2 \psi}{\partial \eta^2} - \frac{\partial^2 \psi}{\partial \xi^2} \right)^2 + 4 \left( \frac{\partial^2 \psi}{\partial \xi \partial \eta} \right)^2 \right\}, \end{aligned} \quad (3.28)$$

$$\begin{aligned} \frac{\partial T_p}{\partial t} = & -\text{Re}_p d_o \left( \frac{\partial T_p}{\partial \xi} \frac{\partial \psi_p}{\partial \eta} - \frac{\partial T_p}{\partial \eta} \frac{\partial \psi_p}{\partial \xi} \right) - (1 - C_v) \text{Re}_p d_o \beta_2 (T_p - T) + \\ & \frac{\text{Re}_p d_o M_{\text{nf}_p} \text{Ec}}{\gamma_1 U_2^2} H T_p \left( \frac{\partial H}{\partial \xi} \frac{\partial \psi_p}{\partial \eta} - \frac{\partial H}{\partial \eta} \frac{\partial \psi_p}{\partial \xi} \right). \end{aligned} \quad (3.29)$$

### 3.5 Grid Generation

The accuracy of the numerical algorithm in the regions with a strong MF requires an adaptive numerical grid. A curvilinear grid can be considered as a discrete version of mapping  $\xi = \xi(x, y), \eta = \eta(x, y)$  from the physical region in the coordinates  $(\xi, \eta)$  to a computational region in the new coordinates  $(x, y)$ ,  $0 \leq x, y \leq 1$ . We consider the particular case of a rectangular grid with stretching, i.e.,  $\xi \equiv \xi(x)$ ,  $\eta \equiv \eta(y)$  defined by:

$$\xi \equiv \xi(x) = x_0 \left( 1 + \frac{\sinh(\tau(x - \lambda))}{\sinh(\tau\lambda)} \right),$$

$$\eta \equiv \eta(y) = \frac{2\delta_1 - \delta_2 + (\delta_2 - 2\delta_1)\kappa_1^{(y-\delta_1)/(1-\delta_1)}}{(1 + 2\delta_1) \left( 1 + \kappa_1^{(y-\delta_1)/(1-\delta_1)} \right)}, \quad (3.30)$$

Where

$$\lambda = \frac{1}{2\tau} \ln \left| \frac{1 + (e^\tau - 1)(x_0 / x_{\max})}{1 + (e^{-\tau} - 1)(x_0 / x_{\max})} \right|,$$

$$\kappa_1 = \left( \frac{\delta_2 + 1}{\delta_2 - 1} \right), \quad \kappa_2 = \left( \frac{-2\delta_1 + \delta_2 + \eta(1 + 2\delta_2)}{2\delta_1 + \delta_2 - \eta(1 + 2\delta_2)} \right) \quad (3.31)$$

In the above expressions,  $x_{\max} = \bar{L}/h$  is the dimensionless length of the channel,  $x_0$  is the point where the grid clustering occurs, and  $\tau$  is a parameter controlling the rate of clustering toward the  $\xi$  direction. It varies from zero (no stretching) to 1, to produce a dense grid near  $\xi = x_0$ . Further,  $\delta_1$  and  $\delta_2$  are parameters to control stretching in the  $\eta$  direction. If  $\delta_1 = 0$ , the mesh is refined near  $\eta = 1$ , whereas, if  $\delta_1 = 0.5$ , the mesh is also refined near  $\eta = 0$  (Tzirtzilakis, 2008). Thus, the grid is clustered in the areas of large gradients of the MF. **Figure 3.2** illustrates the techniques.



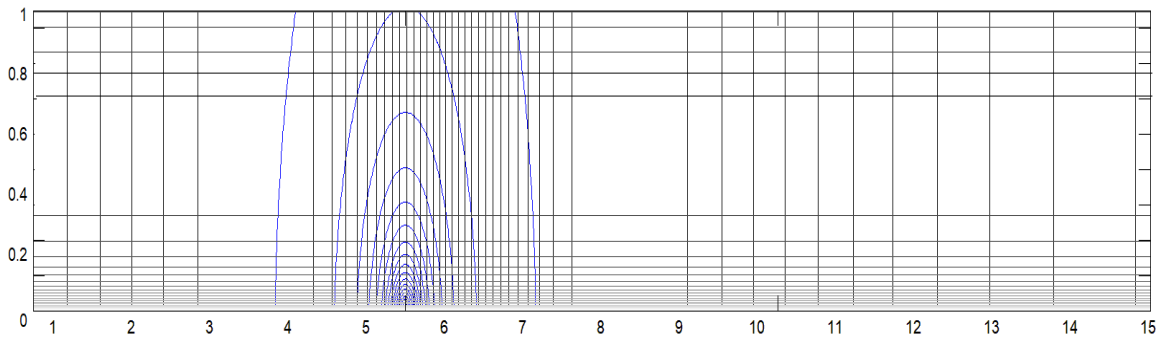


**Figure 3.2** Adaptive finite-difference grid.

Solving Equations (3.30) with regard to  $x(\xi)$ ,  $y(\eta)$  yields:

$$x \equiv x(\xi) = \lambda + \frac{1}{\tau} \sinh^{-1} \left( \left( \frac{\xi}{x_0} - 1 \right) \sinh(\tau\lambda) \right), \quad y \equiv y(\eta) = \delta_1 + \frac{(1-\delta_1) \ln \kappa_1}{\ln \kappa_1}. \quad (3.32)$$

The partial derivatives in (23)-(29) are replaced as follows.

$$\frac{\partial}{\partial \xi} = \frac{\partial}{\partial x} \frac{dx}{d\xi} = \frac{\partial}{\partial x} w_x, \quad \frac{\partial}{\partial \eta} = \frac{\partial}{\partial y} \frac{dy}{d\eta} = w_y \frac{\partial}{\partial y}, \quad (3.33)$$

$$\begin{aligned} \frac{\partial^2}{\partial \xi^2} &= \frac{\partial^2}{\partial x^2} \left( \frac{dx}{d\xi} \right)^2 + \frac{\partial}{\partial y} \frac{d^2x}{d\xi^2} = w_x^2 \frac{\partial^2}{\partial x^2} + w_\xi \frac{\partial}{\partial x}, \\ \frac{\partial^2}{\partial \eta^2} &= \frac{\partial^2}{\partial y^2} \left( \frac{dy}{d\eta} \right)^2 + \frac{\partial}{\partial y} \frac{d^2y}{d\eta^2} = w_y^2 \frac{\partial^2}{\partial y^2} + w_\eta \frac{\partial}{\partial y}. \end{aligned} \quad (3.34)$$

Some calculus yields

$$\frac{\partial^2 \psi}{\partial x^2} w_x^2 + w_y^2 \frac{\partial^2 \psi}{\partial y^2} + w_\xi \frac{\partial \psi}{\partial x} + w_\eta \frac{\partial \psi}{\partial y} = -J, \quad (3.35)$$

$$\frac{\partial^2 \psi_p}{\partial x^2} w_x^2 + \frac{\partial^2 \psi_p}{\partial y^2} w_y^2 + w_\xi \frac{\partial \psi_p}{\partial x} + w_\eta \frac{\partial \psi_p}{\partial y} = -J_p, \quad (3.36)$$

$$\begin{aligned} \frac{\partial J}{\partial t} = & w_x^2 \frac{\partial^2 J}{\partial x^2} + w_y^2 \frac{\partial^2 J}{\partial y^2} + w_\xi \frac{\partial J}{\partial x} + w_\eta \frac{\partial J}{\partial y} - \text{Re} w_x w_y \left( \frac{\partial J}{\partial x} \frac{\partial \psi}{\partial y} - \frac{\partial J}{\partial y} \frac{\partial \psi}{\partial x} \right) + \\ & C_v \beta_1 D_p \text{Re} (U_2 J_p - U_2^2 J) + M_{\text{nf}} \text{Re} H w_x w_y \left( \frac{\partial H}{\partial x} \frac{\partial T}{\partial y} - \frac{\partial H}{\partial y} \frac{\partial T}{\partial x} \right), \end{aligned} \quad (3.37a)$$

$$\begin{aligned} \frac{\partial J_p}{\partial t} = & -\text{Re}_p d_o w_x w_y \left( \frac{\partial J_p}{\partial x} \frac{\partial \psi_p}{\partial y} - \frac{\partial J_p}{\partial y} \frac{\partial \psi_p}{\partial x} \right) - \\ & (1 - C_v) \text{Re}_p d_o \beta_1 (U_2 J_p - U_2^2 J) + \\ & \text{Re}_p d_o M_{\text{nf}_p} H w_x w_y \left( \frac{\partial H}{\partial x} \frac{\partial T_p}{\partial y} - \frac{\partial H}{\partial y} \frac{\partial T_p}{\partial x} \right), \end{aligned} \quad (3.38a)$$

$$\begin{aligned} \text{Pr} \frac{\partial T}{\partial t} = & w_x^2 \frac{\partial^2 T}{\partial x^2} + w_y^2 \frac{\partial^2 T}{\partial y^2} + w_\xi \frac{\partial T}{\partial x} + w_\eta \frac{\partial T}{\partial y} - \\ & \text{Pr} \text{Re} w_x w_y \left( \frac{\partial T}{\partial x} \frac{\partial \psi}{\partial y} - \frac{\partial T}{\partial y} \frac{\partial \psi}{\partial x} \right) + \text{Re} \text{Pr} C_v D_p \gamma_p \beta_2 (u_{r2} T_p - u_{r2}^2 T) + \\ & M_{\text{nf}} \text{Pr} \text{Re} \text{Ec} H T_p w_x w_y \left( \frac{\partial H}{\partial x} \frac{\partial T_p}{\partial y} - \frac{\partial H}{\partial y} \frac{\partial T_p}{\partial x} \right) + \\ & \text{Pr} \text{Re} \left\{ \left( w_y^2 \frac{\partial^2 \psi}{\partial y^2} + w_\eta \frac{\partial \psi}{\partial y} - w_x^2 \frac{\partial^2 \psi}{\partial x^2} - w_\xi \frac{\partial \psi}{\partial x} \right)^2 + 4 \left( w_x w_y \frac{\partial^2 \psi}{\partial x \partial y} \right)^2 \right\}, \end{aligned} \quad (3.39a)$$

$$\begin{aligned} \frac{\partial T_p}{\partial t} = & -\text{Re}_p d_o w_x w_y \left( \frac{\partial T_p}{\partial x} \frac{\partial \psi_p}{\partial y} - \frac{\partial T_p}{\partial y} \frac{\partial \psi_p}{\partial x} \right) - (1 - C_v) \text{Re}_p d_o \beta_2 (T_p - T) + \\ & \frac{\text{Re}_p d_o M_{\text{nf}_p} \text{Ec}}{\gamma_1 U_2^2} H T_p w_x w_y \left( \frac{\partial H}{\partial x} \frac{\partial \psi_p}{\partial y} - \frac{\partial H}{\partial y} \frac{\partial \psi_p}{\partial x} \right), \end{aligned} \quad (3.40a)$$

The additional non-dimensional parameters are as follows.

$$\begin{aligned}
M_{nF} &= \frac{\bar{\mu}_0 \bar{K} \bar{H}_0^2 \bar{k}}{\bar{\rho} \bar{u}_r^2 \bar{q}_0 \bar{h}}, M_{nF_p} = \frac{\bar{\mu}_0 \bar{K} \bar{H}_0^2 \bar{k}}{\bar{\rho}_p \bar{u}_{r1}^2 \bar{q}_0 \bar{h}}, \beta_1 = \frac{1}{St} = F_D \frac{\bar{h}}{\bar{u}_r}, \beta_2 = \frac{6\bar{h}_v}{d} \frac{\bar{h}}{\bar{u}_r}, \\
U_2 &= \frac{\bar{u}_r}{\bar{u}_{r1}}, \gamma_1 = \frac{\bar{c}_p}{\bar{c}}, d_o = \frac{d}{\bar{h}}, D_p = \frac{\bar{\rho}_p}{\bar{\rho}}, Re = \frac{\bar{\rho} \bar{u}_r \bar{h}}{\bar{\mu}}, Pr = \frac{\bar{c} \bar{\mu}}{\bar{k}}, Ec = \frac{\bar{u}_r^2 \bar{k}}{c \bar{q}_0 \bar{h}},
\end{aligned} \tag{3.41}$$

where  $M_{nF}$  and  $M_{nF_p}$  are the magnetic numbers (the FHD effect) of the blood and MN, respectively.  $\beta_1, \beta_2$  control the energy transfer from the blood flow to the MN and vice versa.  $U_2$  is the ratio of the maximum velocity of the flow to the maximum velocity of the MN at the entrance.  $\gamma_p, d_o, D_p$  are the ratios of the heat capacity, size, and density of the MN to the heat capacity, channel height, and density of the blood, respectively.  $Re, Ec, St$  are the Reynolds number, the Peclet number, the Eckert number, and the Stokes number, respectively.

### 3.6 Numerical Method

The equations for the stream functions of the blood and the MN flow (3.35)-(3.36) are approximated by the standard finite-difference equations and solved by the block Gauss-Seidel method (Cervera et al., 1996). This is followed by the successive over-relaxation (SOR) as follows.  $\psi_{new}^{k+1} = \psi_{GS}^{k+1} \theta + (1-\theta) \psi^k$ , where  $\psi_{GS}^{k+1}$  is the numerical solution obtained by the block Gauss-Seidel method,  $\psi^k$  is the solution at the previous iteration step  $k$ , and  $\theta$  is the relaxation parameter. Note that Equations (3.35)-(3.36) depend implicitly on time due to  $J, J_p$  at the right-hand sides. Hence, the equations must be solved at every time step. The functions  $J, J_p$  are taken from the  $n$ -th time step. The numerical solution of Equations (3.37b)-(3.40b) is based on a similar procedure including the block Gauss-Seidel and the SOR. Writing (3.37a)-(3.40a) in the standard form yields:

$$\frac{\partial J}{\partial t} = A_1 \frac{\partial^2 J}{\partial x^2} + B_1 \frac{\partial^2 J}{\partial y^2} + C_1 \frac{\partial J}{\partial x} + D_1 \frac{\partial J}{\partial y} + E_1 J + F_1, \tag{3.37b}$$

$$\frac{\partial J_p}{\partial t} = C_2 \frac{\partial J_p}{\partial x} + D_2 \frac{\partial J_p}{\partial y} + E_2 J + F_2, \quad (3.38b)$$

$$\frac{\partial T}{\partial t} = A_3 \frac{\partial^2 T}{\partial x^2} + B_3 \frac{\partial^2 T}{\partial y^2} + C_3 \frac{\partial T}{\partial x} + D_3 \frac{\partial T}{\partial y} + E_3 J + F_3, \quad (3.39b)$$

$$\frac{\partial T_p}{\partial t} = C_4 \frac{\partial T_p}{\partial x} + D_4 \frac{\partial T_p}{\partial y} + E_4 J + F_4, \quad (3.40b)$$

where coefficients  $A_i, B_i, C_i, D_i$  and the right-hand-side  $F_i$  in each equation depend on the other unknowns and their partial derivatives. We apply the standard second-order finite-difference approximation to the second derivatives and the upwind first-order approximation to the first derivatives. For instance, (3.37b) is approximated as follows:

$$\begin{aligned} \frac{J_{i,j}^{n+1} - J_{i,j}^n}{\tau} = & A_{1,i,j}^n \frac{J_{i+1,j}^{n+1} - 2J_{i,j}^{n+1} + J_{i-1,j}^{n+1}}{\Delta x^2} + B_{1,i,j}^n \frac{J_{i,j+1}^n - 2J_{i,j}^{n+1} + J_{i,j-1}^{n+1}}{\Delta y^2} \\ & + C_{1,i,j}^n \frac{J_{i+1,j}^{n+1} - J_{i,j}^{n+1}}{\Delta x} + C_{1,i,j}^n \frac{J_{i,j}^{n+1} - J_{i-1,j}^{n+1}}{\Delta x} + D_{1,i,j}^n \frac{J_{i,j+1}^n - J_{i,j}^n}{\Delta y} \\ & + D_{1,i,j}^n \frac{J_{i,j}^{n+1} - J_{i,j-1}^{n+1}}{\Delta y} + E_{1,i,j} J_{i,j}^{n+1} + F(T_{i,j}^n, T_{p,i,j}^n, \psi^{n+1}, \psi_p^{n+1}), \end{aligned} \quad (3.37c)$$

where  $J_{i,j}^n = J_{i,j}(x_i, y_j, n\tau)$ ,  $\tau$  is the time step,  $\Delta x = \frac{1}{N}$ ,  $\Delta y = \frac{1}{M}$  are the spatial steps,  $x_i = i\Delta x$ ,  $y_j = j\Delta y$ ,  $i = \overline{1, N-1}$ ,  $j = \overline{1, M-1}$ ,  $N$  is the number of points in the  $x$  direction,  $M$  is the number of points in the  $y$  direction,  $C' = \frac{C+|C|}{2}$ ,  $C'' = \frac{C-|C|}{2}$ ,  $D' = \frac{D+|D|}{2}$ ,  $D'' = \frac{D-|D|}{2}$ .

For  $i=0, N$  and  $j=0, M$  (3.37c) is replaced by the boundary conditions. The resulting tri-diagonal matrix is inverted by the Thomas algorithm. The first-order upwind differences

in (3.37b) result in the first-order approximation, however, the corresponding matrix is diagonally dominant. Consequently, the Thomas algorithm is stable (Bortoli et al., 2015).

The system (3.37b)-(3.40b) is solved by the following iterative algorithm.

1. Calculate  $\psi^{n+1,l+1}$  and  $\psi_p^{n+1,l+1}$  by solving (3.35)-(3.36), where  $J^{n+1,l}$  and  $J$  are taken from the previous iteration  $l$ .
2. Substitute  $\psi^{n+1,l+1}$ ,  $\psi_p^{n+1,l+1}$  into (3.35b)-(3.40b). Find  $J^{n+1,l+1}$  and  $J_p^{n+1,l+1}$ , where  $T^{n+1,l}$   $T_p^{n+1,l}$  are taken from the previous iteration  $l$ .
3. Substitute  $\psi^{n+1,l+1}$ ,  $\psi_p^{n+1,l+1}$ ,  $J^{n+1,l+1}$ ,  $J_p^{n+1,l+1}$ . Find  $T^{n+1,l+1}$ ,  $T_p^{n+1,l+1}$ .
4. The convergence is established when:

$$\Delta = \max_{i,j,U} |U^{l+1} - U^l| < \varepsilon,$$

where  $U = J, J_p, \psi, \psi_p, T, T_p$ , and  $\varepsilon$  is the required accuracy.

5. If  $\Delta \geq \varepsilon$  return to step 1.

Numerical experiments to reach the grid independent solution are shown in **Table 3.1**. The sample tests are

Case 1:  $d = 250$ ,  $\bar{u}_{r_1} = 3.8$ ,  $St \approx 3.56 \times 10^{-5}$ ,  $Re \approx 250$ ,  $Re_p \approx 9.8 \times 10^{-4}$ ,  $f = 1$ .

Case 2 :  $d = 800$ ,  $\bar{u}_{r_1} = 3.8$ ,  $St = 1.14 \times 10^{-4}$ ,  $Re \approx 250$ ,  $Re_p \approx 3.1 \times 10^{-3}$ ,  $f = 1$ .

Case 3 :  $d = 20000$ ,  $\bar{u}_{r_1} = 3.8$ ,  $St = 2.8 \times 10^{-2}$ ,  $Re \approx 250$ ,  $Re_p \approx 1.0$ ,  $f = 1.1$ .

**Table 3.1** shows the difference  $\Delta_{N \times M} = \max_{i,j,U} |U_{N \times M} - U_{2N \times 2M}|$  for solutions obtained on nested grids. For cases 1-3 the grid  $801 \times 81$  provides a grid-independent solution. The grid independence test has been performed for every experiment presented in Section 3.6.

**Table 3.1** Grid-independence test.

No. of grid points in the $x$ and $y$ direction	Case 1 $\Delta_{N \times M}$	Case 2 $\Delta_{N \times M}$	Case 3 $\Delta_{N \times M}$
201 $\times$ 21	$2.1 \times 10^{-4}$	$4.1 \times 10^{-3}$	$4.9 \times 10^{-3}$
401 $\times$ 41	$3.1 \times 10^{-4}$	$4.8 \times 10^{-3}$	$5.1 \times 10^{-3}$
801 $\times$ 81	$2.6 \times 10^{-5}$	$3.5 \times 10^{-5}$	$1.1 \times 10^{-5}$
1601 $\times$ 161	$1.1 \times 10^{-7}$	$2.4 \times 10^{-6}$	$1.8 \times 10^{-6}$

### 3.7 Results and Discussion

Testing hydrodynamic models of the TMDD is hampered by a lack of available data. Up to now, the measurements of the MN flow inside the vessels during the TMDD are not available. However, several experimental studies performed to measure the temperature of the nanofluid have been published. Therefore, the model is validated by 1) comparing with the preceding models, 2) comparing with the published results of the measurements of the temperature of the ferro/nanofluids.

The numerical experiments with the blood flow follow Nacev et al. (2011). A magnet is located at a certain distance below the vessel.  $\text{Fe}_3\text{O}_4$  MN are used for TMDD.

#### 3.7.1 Validation of the model

We compare the proposed two-phase two-way model (TPM) with a single-phase model (SPM<sub>1</sub>) of Tzirtzilakis (2008), and the double-phase, one-way coupled model of Boutopoulos et al. (2020) (OW).

Consider Case 1:  $\text{Re} = 250$ ,  $\beta_2 \approx 4$ ,  $\text{St} \approx 3.56 \times 10^{-4}$ ,  $C_v = 0.001$ , and  $d=250$ . Since  $C_v$  is small, the single-phase and the double-phase models show similar results. **Figure 3.3**

displays the streamlines and the contour lines of the magnitude of the velocity  $|u^2 + v^2|$  for the steady-state solution obtained by the TPM. **Figure 3.4** shows the profile of  $|v|$  for  $x = 5$  (position of the magnet). The numerical experiments show that the difference between the solutions for the TPM and the reference models does not exceed  $10^{-4}$ .

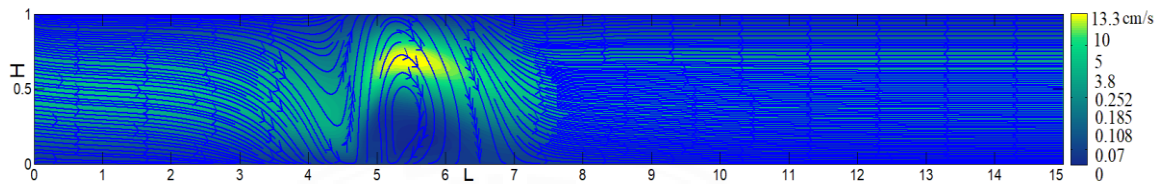


**Figure 3.3** Blood flow, Case 1. The reference models generate similar solutions for

$$C_v = 0.001.$$

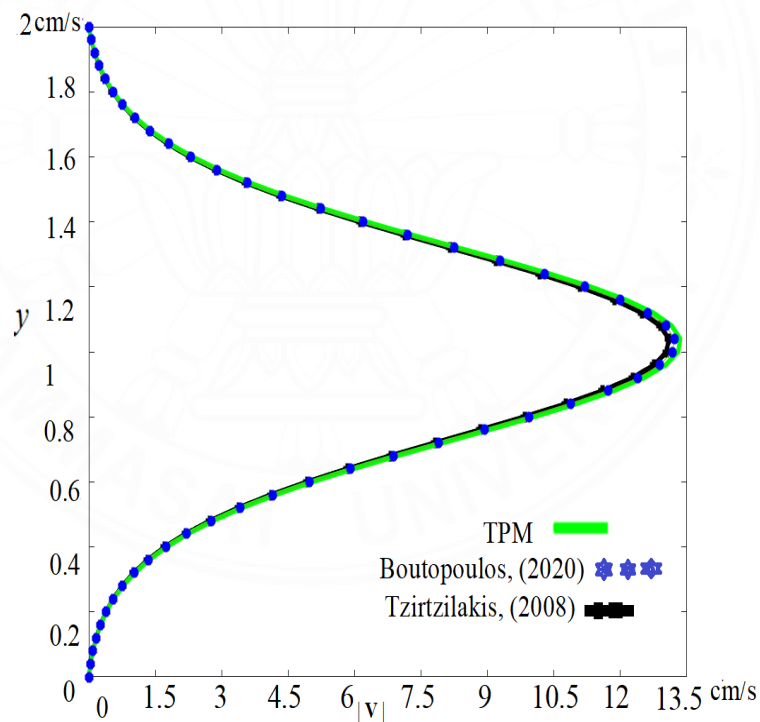
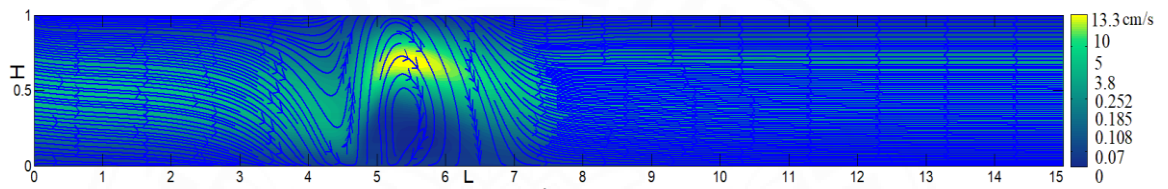
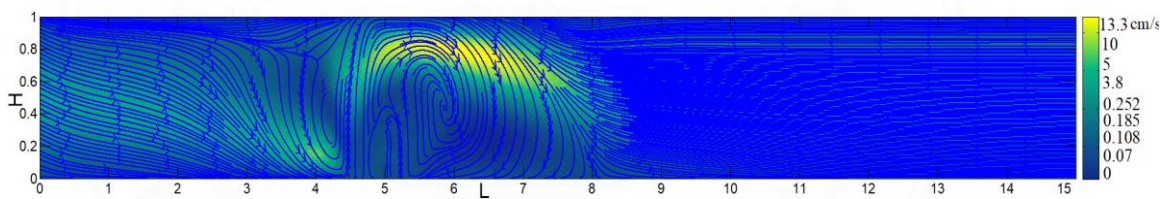


**Figure 3.4** Case 1: Magnitude of the velocity for SPM<sub>1</sub>, OW, and TPM.

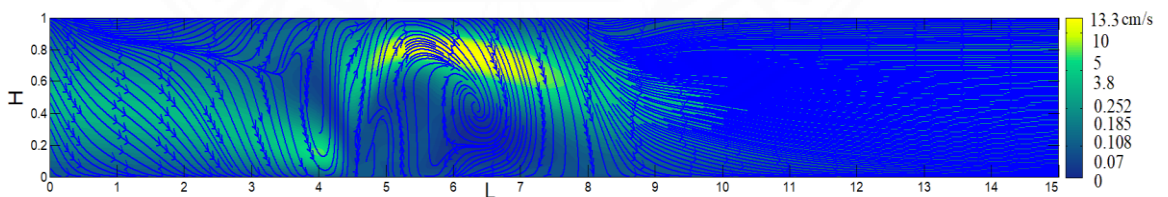
The above tests are considered as a partial validation of the model. However, for large  $C_v = 0.03$  the proposed model shows different results. As an example, consider Case 2:  $\beta_2 \approx 2$ ,  $St = 2.8 \times 10^{-2}$ ,  $Re = 250$ , and  $C_v = 0.03$ . **Figure 3.5** (a, b, and c) show the steady-state solutions for  $d = 20000$  for SPM<sub>1</sub>, OW, and TPM. **Figure 3.6** shows the profile of  $|v|$  for  $x = 5$ . Clearly, in the case of a high concentration of MN, the results obtained by the proposed model are different since the MN have a reverse impact on the dynamics of the blood flow. For instance, the maximum difference between the solution by SPM<sub>1</sub> and the proposed model for  $x = 5$  is about 0.9 cm/s.



a) SM1, Tzirtzilakis, (2008)



b) OW, Boutopoulos et al. (2020) (OW)



c) TPM

**Figure 3.5** Blood flow, Case 2. The reference models vs. TPM.



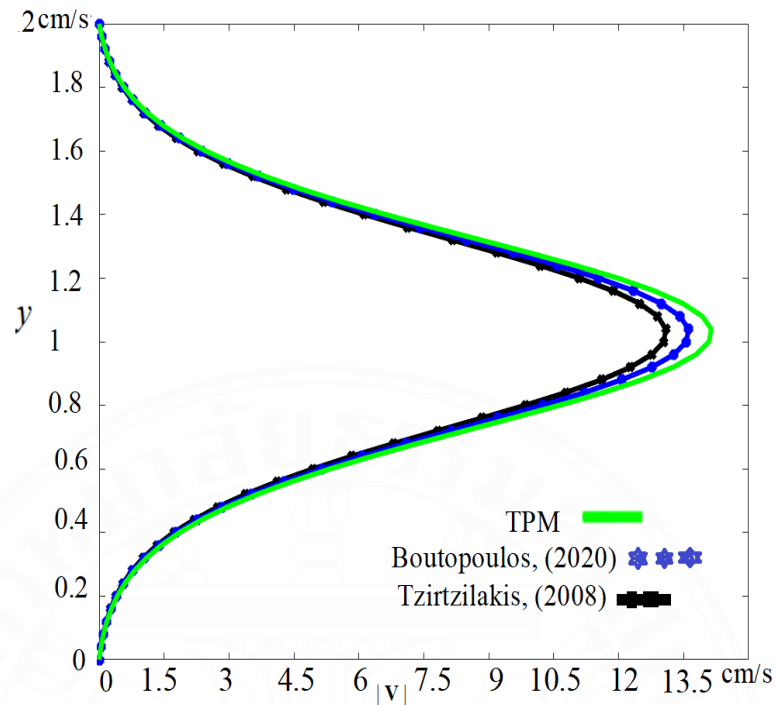


**Figure 3.6** Case 2: Magnitude of the velocity for SPM<sub>1</sub>, OW, and TPM

Wen & Ding (2004) experimentally evaluated the average Nusselt number using a straight copper tube with 970 mm length,  $4.5 \pm 0.02$  mm inner diameters, and  $6.4 \pm 0.05$  mm outer diameter in the laminar regime. The setup consists of four units: the flow loop, the measuring and control unit, the heating unit, and the cooling part. The flow loop further included four sections: the pump with a built-in flow meter, the test section, the reservoir, and the collection tank. The test section consists of a straight copper tube heated by a silicon rubber flexible heater linked to a DC power supply. The nanofluid flows through the copper tube. Thermocouples are used to measure the temperature at the inlet flow and the outlet flow. The Nusselt number is defined by:

$$\text{Nu} = \frac{\bar{h}(y)h_c}{k}, \quad (3.42)$$

where  $h_c$  is the diameter of the tube, and  $\bar{h}$  is the local heat transfer parameter given by:

$$\bar{h} = \frac{q}{T_w - T_m}, \quad (3.43)$$

where  $\bar{T}_m(\bar{y})$  is the mean temperature for a two-phase fluid,  $\bar{T}_w(\bar{y})$  is the temperature of the wall, and  $q$  is convective heat transfer. The boundary and initial conditions of the experimental setup are replicated. The flow of water (mixed with  $\text{Al}_2\text{O}_3$ ) is characterized by  $C_v = 0.04$ ,  $\bar{q} = 1000$ , and  $d = 250$ . The results obtained by the  $\text{SM}_1$ , OW, and a single phase model of Bianco et al. (2009) ( $\text{SM}_2$ ) and the proposed TPM are compared. **Table 3.2** shows the average Nusselt number obtained by numerical simulations vs. the experimental data. Note that the original Boutopoulos et al. (2020) model does not include the temperature equation. Hence, the temperature is simulated by the one-phase version of Equation (3.3), where  $\bar{\rho} = 996 \text{ kg/m}^3$ ,  $\bar{c} = 4180 \text{ J/kgK}$ .

**Table 3.2** Average Nusselt number of the proposed model,  $\text{SPM}_1$ ,  $\text{SPM}_2$  vs. Experiments.

Re	Proposed TPM	$\text{SM}_1$ Tzirtzilakis, (2008)	OW Boutopoulos et al. (2020)	$\text{SM}_2$ Bianco et al. (2009)	Experiments Wen & Ding, (2004)
250	5.75	4.89	4.99	6.88	5.80
270	7.8707	7.01	7.45	7.75	8
300	8.0682	7.66	7.88	7.85	8.13

The average least square error for  $\text{SM}_1$  is 4.8%, for OW is 3.3%, and for  $\text{SM}_2$  is 3.4%. The TPM shows the least square error of about 5%. Therefore, the accuracy of the proposed TPM is comparable with the preceding models when the MF is not applied.

Our second test is performed on the experimental results obtained by Abadeh et al., (2020) for the flow of nanofluids ( $\text{Fe}_3\text{O}_4$ ) with  $C_v \in [0.005, 0.01]$ ,  $d = 250$  through a circular tube a straight tube under constant and alternative magnetic fields. The experimental setup consists of electrical, mechanical, and controlling devices similar to

Wen & Ding (2004), including the source of the MF. A straight circular copper tube (2700 mm) with 7.7 mm outer and 0.7 mm inner diameters has a thermal conductivity of 385 W/mK. Six wires have been installed to produce an MF of about 0.13 T. The average Nu obtained by the reference models and the proposed TPM is displayed in **Table 3.3** for different Reynolds numbers.

**Table 3.3** Average Nusselt number. Numerical models vs. Experimental data.

Re	Proposed TPM	SM <sub>1</sub> Tzirtzilakis, (2008)	OW Boutopoulos et al. (2020)	Experiments Abadeh et al. (2020)
250	5.95	5.50	5.78	6.31
270	6.8707	6.05	6.30	6.99
300	8.0821	7.55	7.66	7.90

The average least square error for SM<sub>1</sub> is 12%, for OW is 8.3%, and for TMP is 5.7%. Clearly, the proposed model shows a better accuracy when applied to the MN-water flow under the impact of the MF.

### 3.7.2 Numerical Experiments and Discussion

Following Nacev et al. (2011) a magnet is located at 5, 10, and 15 cm below the wall. The MF, characterized by  $\bar{B} = 0.5 T$  and  $\bar{B} = 1.0 T$ , is applied to the Fe<sub>3</sub>O<sub>4</sub> MN. These MN are characterized by magnetization  $\bar{M} \approx 100$  kA/m and a diameter of 250, 800, and 20,000 nm. Note that the diameter of human blood vessel ranges from 7  $\mu$ m in the capillaries to 3 cm in the vena cava. The numerical simulations are performed for  $\bar{h} = 2.0$  cm and  $\bar{L} = 30$  cm. This is a typical diameter and a length of the large blood vessel considered by the reference BFD. The MN and the blood enter the vessel at the left

boundary. The left boundary condition for  $\bar{u}$  is a parabola such that  $\max(\bar{u}) = \bar{u}_{r_1}$  at the centerline and  $\bar{u} = 0$  at the walls. The density of the MN and the blood are  $\bar{\rho} = 1050 \text{ kg/m}^3$  and  $\bar{\rho}_p = 5200 \text{ kg/m}^3$ , respectively. The dynamic viscosity of the blood is  $\bar{\mu} = 3.2 \times 10^{-3} \text{ kg/(ms)}$ . The Reynolds number  $\text{Re}_p \approx 9.8 \times 10^{-4}$  and  $\text{Re}_p \approx 3.1 \times 10^{-3}$ , for  $d=250$  and  $800$ , respectively. The drag factor  $f=1$ . When  $d = 20000$ ,  $\text{Re}_p \approx 1.0$  and  $f=1.1$ . Consider the thermal conductivity  $\bar{k} = 2.2 \times 10^{-3} \text{ J/(msK)}$ , the heat capacity of the MN and the blood are  $\bar{c} = 14.65 \text{ J/kgK}$  and  $\bar{c}_p = 670 \text{ J/kgK}$ , respectively. Hence the Prandtl number is  $\text{Pr} = \frac{\bar{c}\bar{\mu}}{\bar{k}} \approx 21$ .

The parameters to control the transfer of momentum and energy between the MN and the blood are given by (Giresha et al., 2017).

$$\beta_1 = \bar{F}_D \frac{\bar{h}}{\bar{u}_r} = \frac{18\bar{\mu}}{d^2\bar{\rho}C_c} \frac{\bar{h}}{\bar{u}_r}, \beta_2 = \bar{h}_v \frac{\bar{h}}{\bar{u}_r} = \frac{6h_h}{d} \frac{\bar{h}}{\bar{u}_r}. \quad (3.44)$$

Therefore,  $\beta_1 \propto \frac{1}{\bar{u}_r}$ ,  $\beta_2 \propto \frac{1}{\bar{u}_r}$ .

The magnetic numbers characterize the blood and the MN flow under the impact of the MF (Tzirtzilakis, 2004)

$$\text{M}_{\text{nf}} = \frac{\bar{M}\bar{B}\bar{h}^2\bar{\rho}}{\bar{\mu}^2\text{Re}^2} \propto \frac{\bar{M}\bar{B}\bar{h}^2}{\text{Re}^2}, \text{M}_{\text{nf}_p} = \frac{\bar{M}\bar{B}d^2\bar{\rho}^2}{\bar{\mu}^2\bar{\rho}_p\text{Re}_p^2} \propto \frac{\bar{M}\bar{B}d^2}{\text{Re}_p^2}. \quad (3.45)$$

Finally,  $\text{St} = \frac{d^2\bar{\rho}_p C \bar{u}_r}{18\bar{\mu} \bar{h}}$ . Hence,  $\text{St} \propto d^2\bar{u}_r$ . Substituting  $\bar{u}_r = \frac{\text{Re}\bar{\mu}}{h\bar{\rho}}$  yields  $\text{St} \propto d^2 \text{Re}$ .

### 3.7.2.1 Impact of the Reynolds Number

The following examples analyze the flow patterns generated by the MF and the DF.

The vorticity of the blood flow is an important factor that affects the patient during and after the TMDD. It has long been established that the vorticity of the blood flow is the cause of the cardiac dysfunction. Moreover, the blood vortices indicate physiological changes in the surrounding system, and can provide early indications of the long-term cardiac outcome (Pedrizzetti et al., 2014). The effects of MF on microcirculation and microvasculature are not clear or widely explored. However, many studies indicate that MFs could trigger either vasodilation or vasoconstriction (McKay et al., 2007, Contijoch et al., 2020). In the context of this work, we also refer to hemolysis. That is the mechanical damage of the red blood cells due to an excessively high stress induced by high gradients in the blood flow (Bletsos et al., 2021). Many studies have been performed to experimentally detect vascular inconsistencies. The medical research shows that the preferred vascular blood flow mode is laminar (Pedrizzetti et al., 2014). However, during the TMDD, the blood flow is affected by the MF and the exchange of the momentum and the energy between the MN and the flow. Given that cancer chemotherapy requires from 3 to 6 months, there is a serious concern regarding the long-term effects of the TMDD on the vascular system. Hence, the numerical analysis of the coupled blood-MN flow may become indispensable, to study the patterns of the coupled blood-MN flow.

Consider three cases of the two-phase blood-MN flow characterized by  $C_v \approx 0.001$  and  $\bar{M} \approx 10000$ ,  $\lambda_a = 200 \mu\text{m}$ , and the Cunningham correction coefficient  $C_c \approx 4$  (Kenjereš & Tjin, 2017).

The magnet is located at  $(a,b)=(10, 10)$  and  $\bar{B}=0.5$ . **Figure 3.7** shows the streamlines of the blood and MN flow along with the contour lines. The vorticity function for the steady-state flow with varying entrance velocity is in the midline of the left boundary.

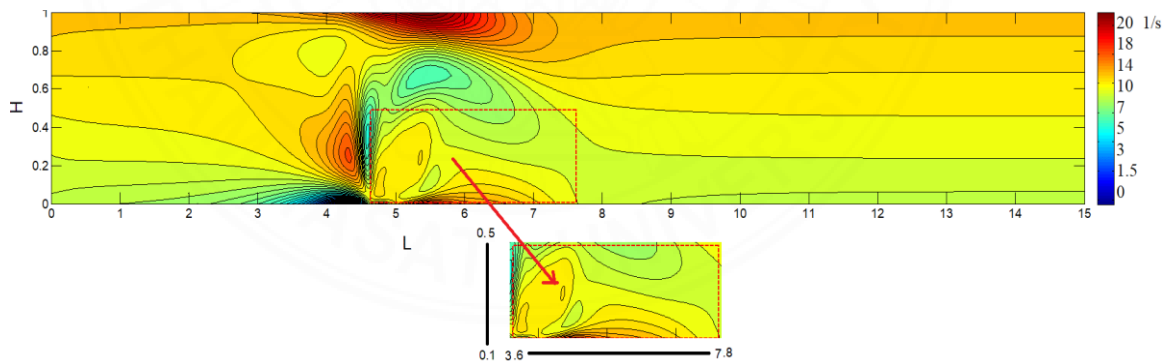
Case 1:  $\bar{u}_r = 3.8 \times 10^{-2}$ . In this case,  $Re \approx 25$ ,  $Re_p \approx 9.8 \times 10^{-4}$ ,  $St \approx 3.56 \times 10^{-4}$ ,  $M_{nF} \approx 3281$ . This setup complies with the data published by Nacev et al. (2011). The circulation starts at  $t_c \approx 13$  min and reaches the steady state at  $t_s \approx 1.5$  h. The MF

generates a lower-wall vortex. The blood near the upper wall responds, creating backflow. The velocity in the lower part of the vortex is minimal which makes TMDD possible (**Figure 3.7 (a and b)**). The velocity at the upper part of the vortex reaches 30 cm/s due to the impact of the MF.

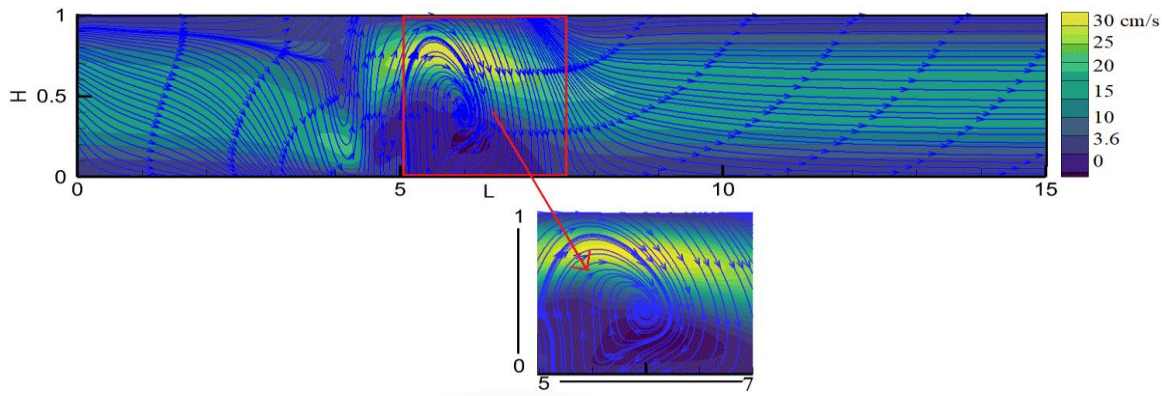
Case 2:  $\bar{u}_r \approx 7.6 \times 10^{-2}$  corresponds to  $Re \approx 50$ ,  $Re_p \approx 4.1 \times 10^{-3}$ ,  $St \approx 7.12 \times 10^{-4}$ , and  $M_{nF} \approx 820$ . In this case, the size of the regions where the velocity is low or close to zero (the TMDD regions) decreases (**Figure 3.7b**).

Case 3: Finally for  $\bar{u}_r \approx 15 \times 10^{-2}$ ,  $Re \approx 100$ ,  $Re_p \approx 1.0 \times 10^{-2}$ ,  $St \approx 1.42 \times 10^{-3}$  and  $M_{nF} \approx 205$ . There is a further decrease in the size of the TMDD regions (**Figure 3.7c**).

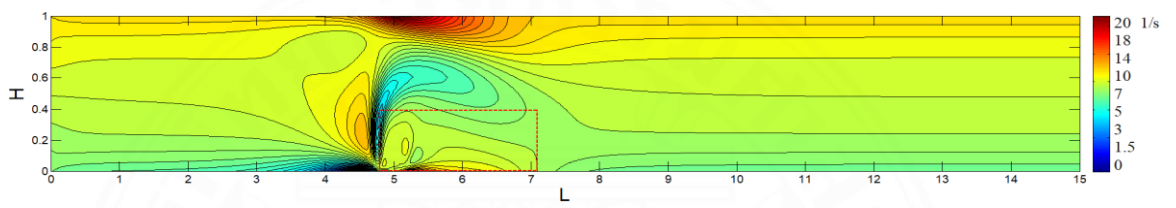
The graphs in **Figure 3.7** show that the DF works against the MF, decreasing the efficiency of TMDD. Clearly, to improve the dynamics of the blood flow, the magnet has to be placed closer to the TMDD zone. Alternatively, the intensity of the MF must be increased. Further, the contour plots of the vorticity function in **Figure 3.7 (a1, b1, and c1)** show that the vorticity increases as the  $Re$  increases. However, the vorticity plot for the smallest  $Re \approx 25$  has the most complex geometry (**Figure 3.7 (a1, b1, and c1)**).



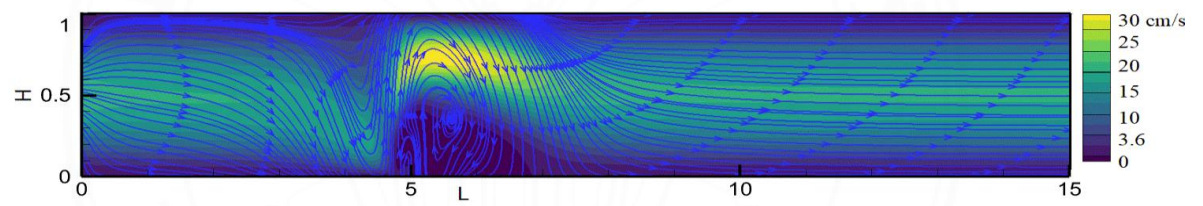
a1)



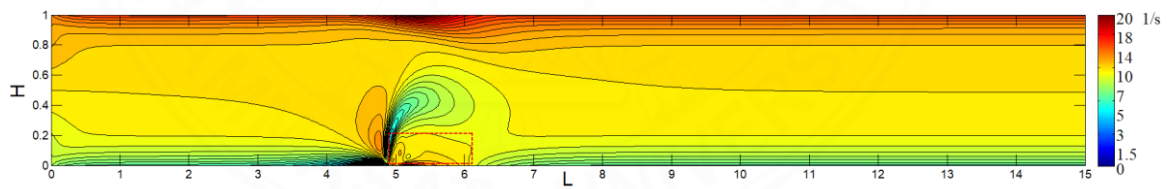
a2)



b1)



b2)



c1)



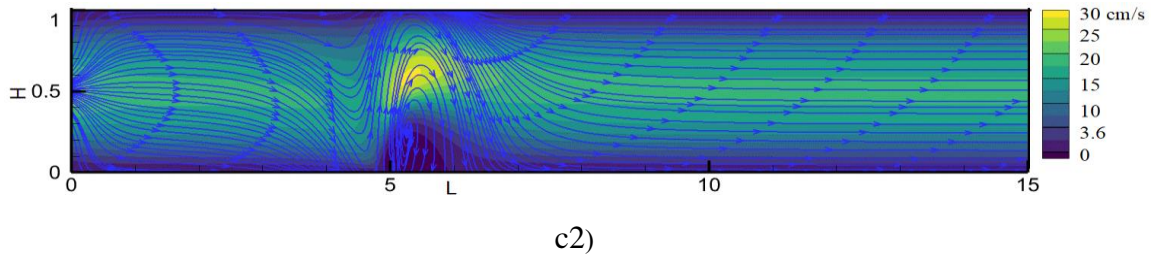


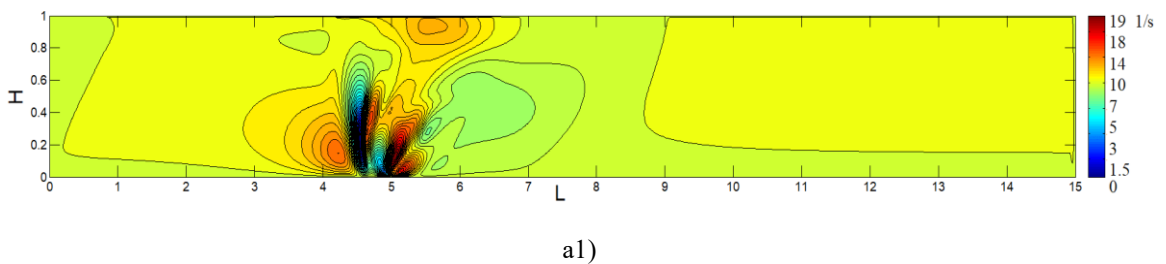
**Figure 3.7** Blood flow,  $B = 0.5$ ,  $d = 250$ ,  $C_v = 0.001$ . a)  $Re=25$ , b)  $Re=50$ , c)  $Re=100$ ;  
1) contour lines of the vorticity function, 2) streamline plot.

The streamlines of the flow and the contour lines of the vorticity function for the steady-state flow are shown in **Figure 3.8**.

Case 1: The MN flow creates four vortices with the antiparallel velocity vectors near the position of the magnet ( $x = 5$ ). The TMDD zones, characterized by the low magnitude of the MN flow, are near  $x = 5$  and  $x = 6.5$ . The maximum MN velocity is about 28 cm/s.

Case 2: The topological structure of the MN flow is approximately the same as in Case 1 (**Figure 3.8b**). However, the TMDD zone becomes smaller.

Case 3: **Figure 3.8c** shows the generation of the new vortices. A double-vortex is observed on the left side of the vessel in **Figure 3.8c2**. The area of the TMDD zones is small. However, the area of the regions with the large horizontal velocity is also getting smaller. Observe that the magnetic numbers for the blood flow and MN decrease as the Stokes number increases with an increase of  $Re$  as follows. Case 1:  $M_{nF} = 3281, M_{nF_p} \approx 6677$ ,  $St \approx 3.56 \times 10^{-4}$ ; Case 2:  $M_{nF} \approx 820, M_{nF_p} \approx 677$ ,  $St \approx 7.12 \times 10^{-4}$ ; Case 3:  $M_{nF} \approx 205, M_{nF_p} \approx 67$ ,  $St \approx 1.42 \times 10^{-3}$ .





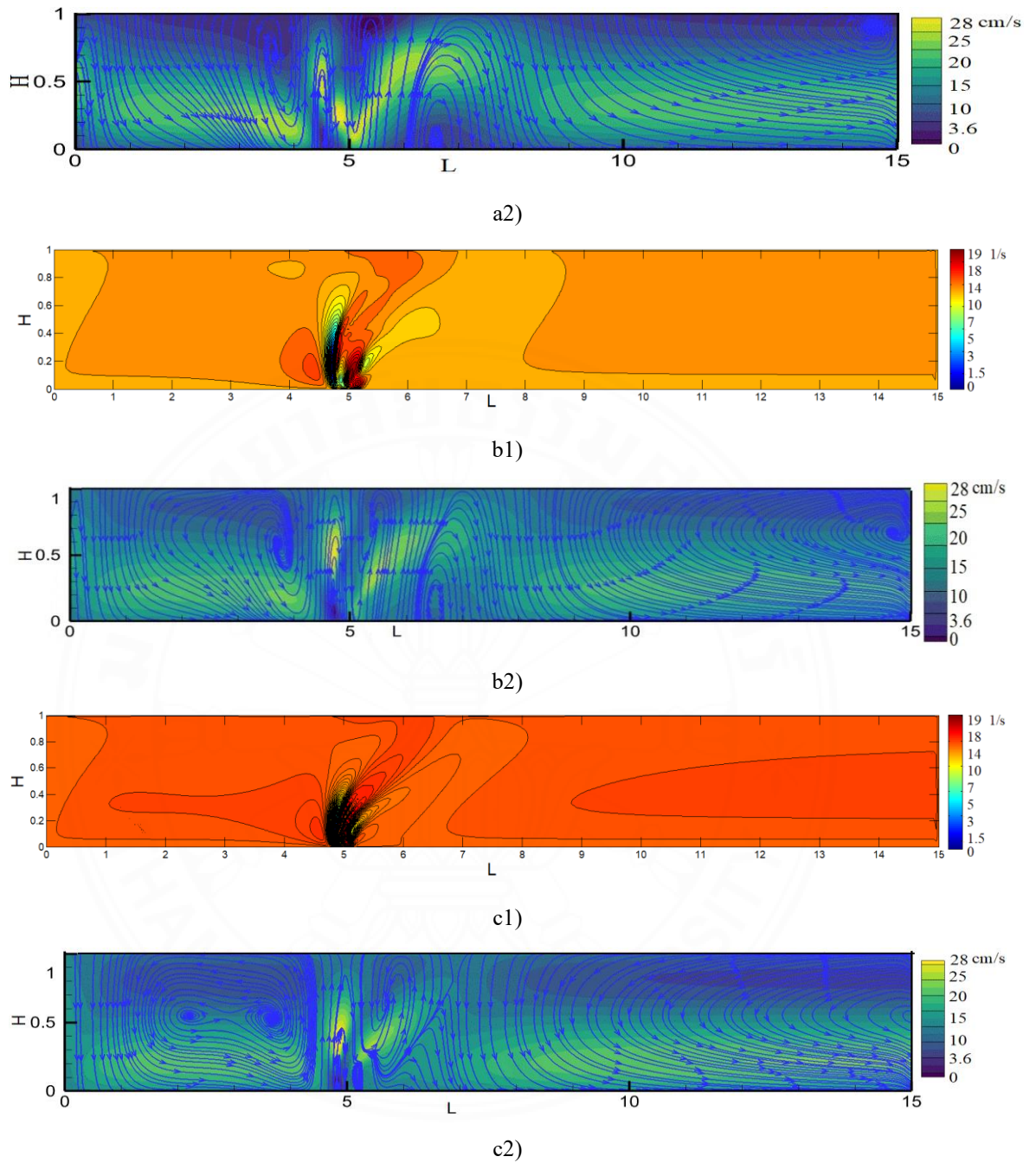


**Figure 3.8** MN flow:  $B = 0.5$ ,  $d = 250$ ,  $C_v = 0.001$ . a)  $Re=25$ , b)  $Re=50$ , c)  $Re=100$ ; 1) contour lines of the vorticity function, 2) streamline plots.

Although the Stokes number for the numerical experiments is relatively small, e.g., the maximum  $St \approx 1.42 \times 10^{-3}$ , the solid phase MN does not follow the streamlines of the blood flow due to the impact of the MF.

### 3.7.2.2 Impact of the Magnetic Field

In order to evaluate the impact of MF, consider  $Re_p \approx 9.8 \times 10^{-4}$  and  $Re = 250$ . The vertical position of the magnet is 15 cm, 10 cm, and 5 cm below the wall. The topology of the blood and MN flows is visualized in **Figures 3.9-3.12**. We consider that the TMDD is efficient if the blood velocity is low whereas the MN velocity towards the magnet is high.

When  $B = 0.5$ , the magnet located at 15 cm does not have a significant impact on the MN. As a result, the flow becomes laminar with the exception of the region affected by the MF (see **Figure 3.9a**). Moving the magnet closer to the vessel expands the region of blood circulation. The TMDD zone where the velocity is close to zero increases. The topological pattern of the flow remains approximately the same for  $b=10$  (**Figure 3.9b**). Moving the wire closer ( $b=5$ ) creates 3 vortices with a maximum velocity of about 15 cm/s.

The TMDD zone expands significantly. **Figure 3.10** displays the streamlines of the MN flow for  $B = 0.5$ . Clearly, the MF attracts the MN to the region of the TMDD. However, the topology of the flow is complex. It does not follow the streamlines of the blood flow when the impact of the MF is strong (**Figure 3.10**).

When  $B = 1.0$ , the source, located at 10 and 15 cm below the vessel (**Figures 3.11 (a and b)**), generates blood flow topologically similar to that shown in **Figures 3.9 (a and b)**. However, the TMDD region becomes considerably larger. When  $B = 1.0$   $b=5$  (**Figure 11c**), the impact of the MF is the most significant. However, the topology of the flow is complex and is characterized by an increased vorticity.

**Figure 3.12** for  $B=1.0$  shows how the MF works against the DF. The topology of the MN flow in **Figure 3.12** is characterized by 4 large vortices. The magnetic numbers

increase from  $M_{nF} = 3281$  to  $M_{nF_p} \approx 6677$  when  $B = 0.5$ , to  $M_{nF} \approx 6562, M_{nF_p} \approx 13354$  when  $B = 1.0$ . **Figure 3.12c** shows that an MF with a high intensity positioned close to the blood vessel has a strong impact on the vorticity of the blood flow. The evaluation of its impact on the patient and the negative effects of the vorticity versus the positive results of the TMDD is an open problem. This requires further experimental research outside the scope of this paper. However, the proposed model can be used as a second opinion to evaluate possible side effects.

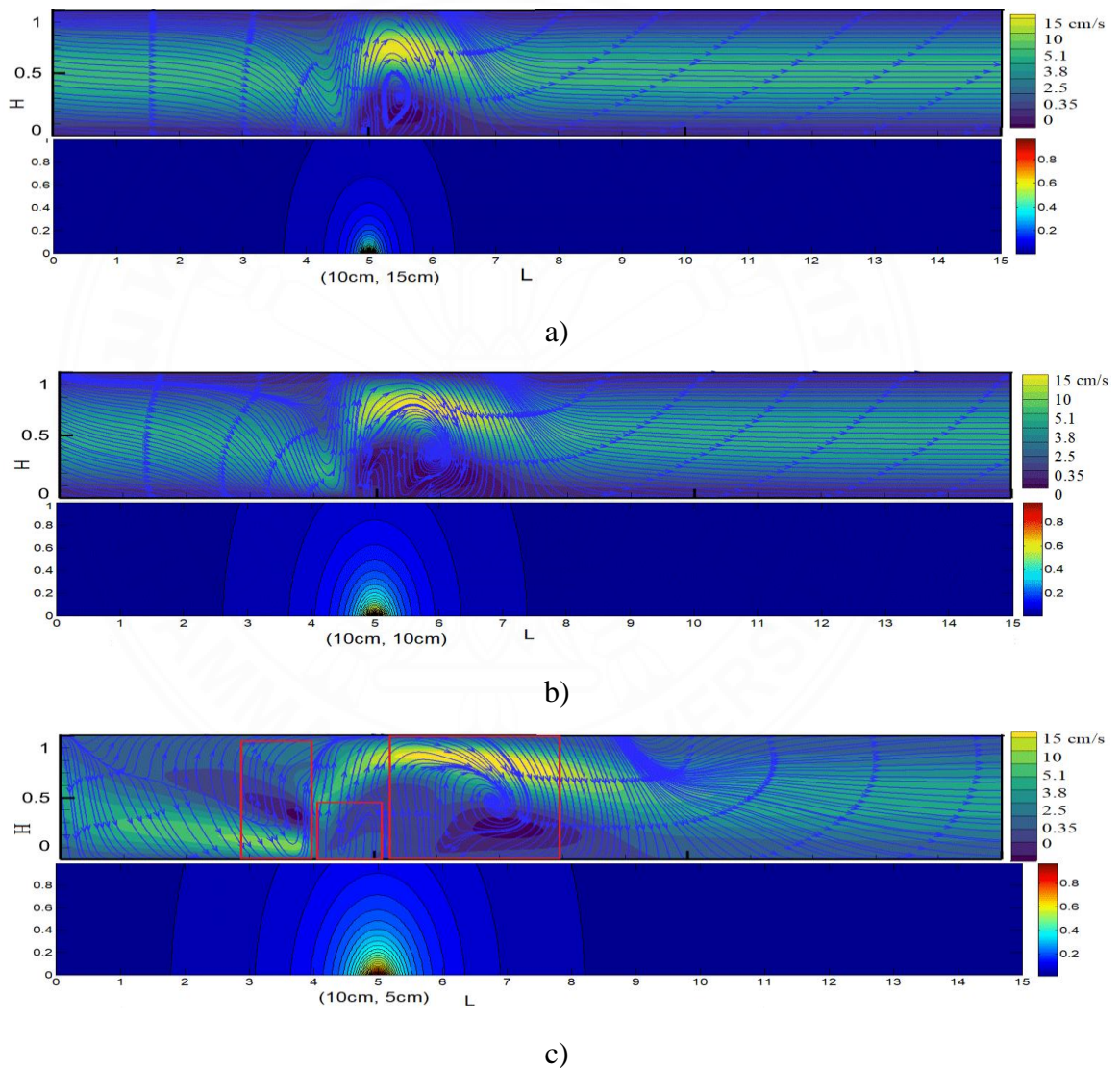
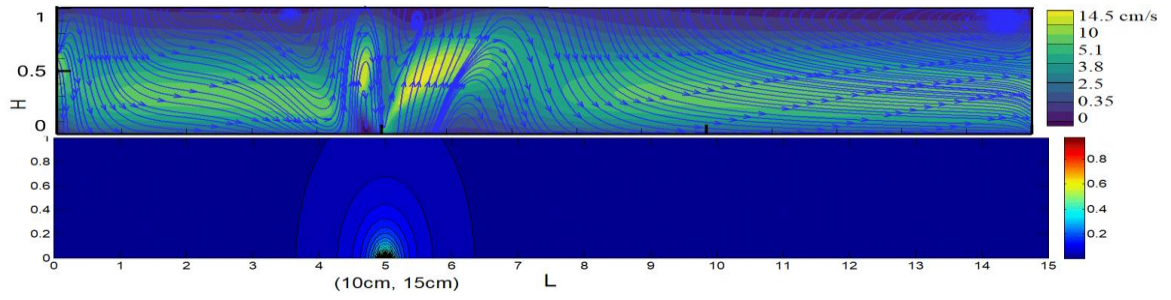
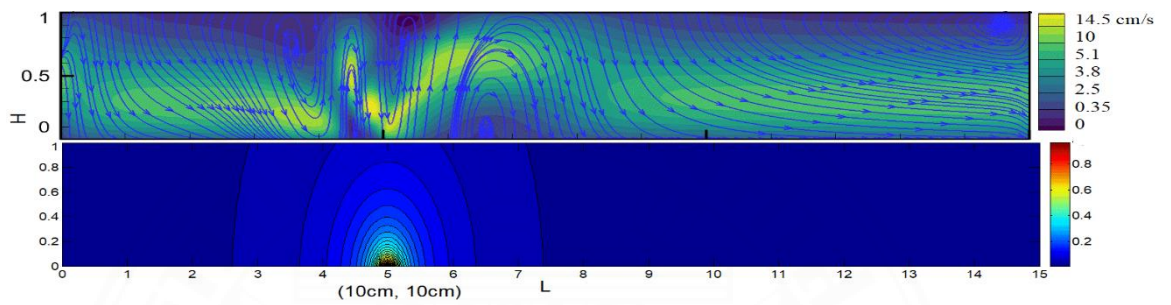


**Figure 3.9** Streamlines of the blood flow:  $B = 0.5$  a)  $b=15$ , b)  $b=10$ , c)  $b=5$ .

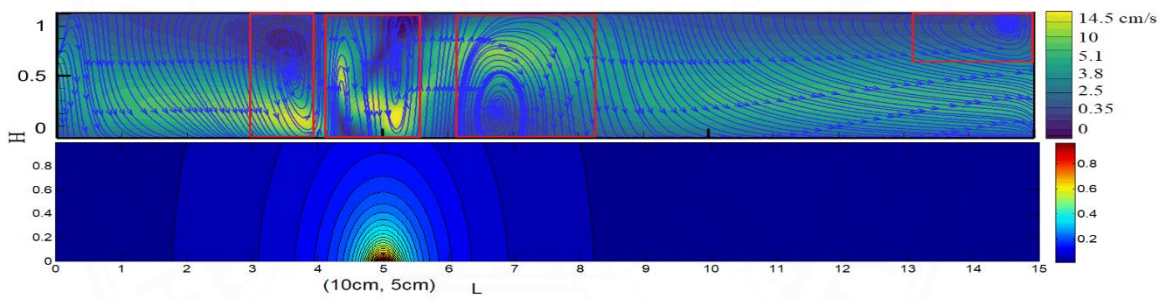




a)

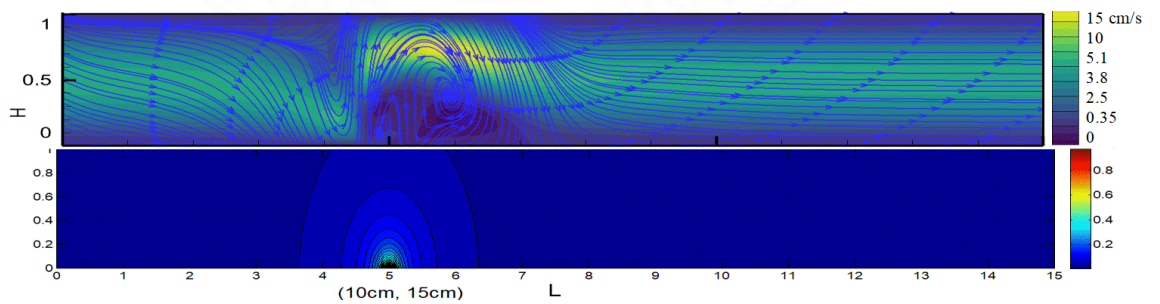


b)

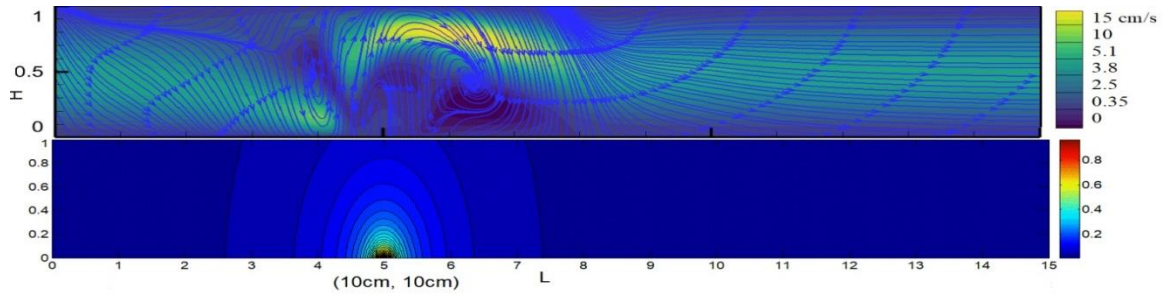


c)

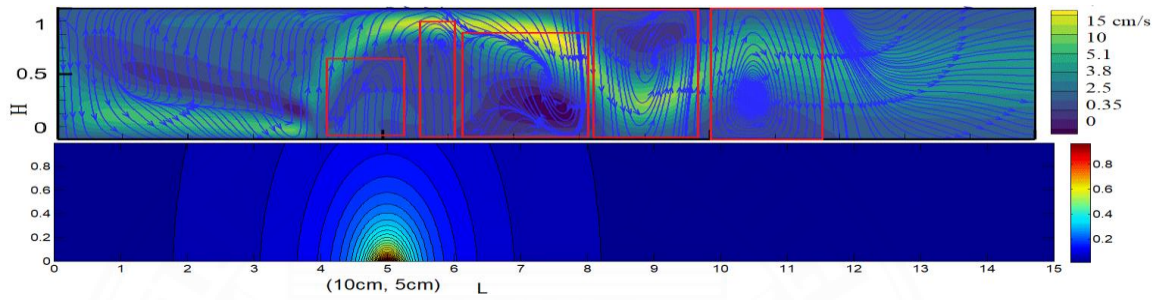
**Figure 3:10** Streamlines of the MN flow:  $B = 0.5$ , a)  $b=15$ , b)  $b=10$ , c)  $b=5$ .



a)

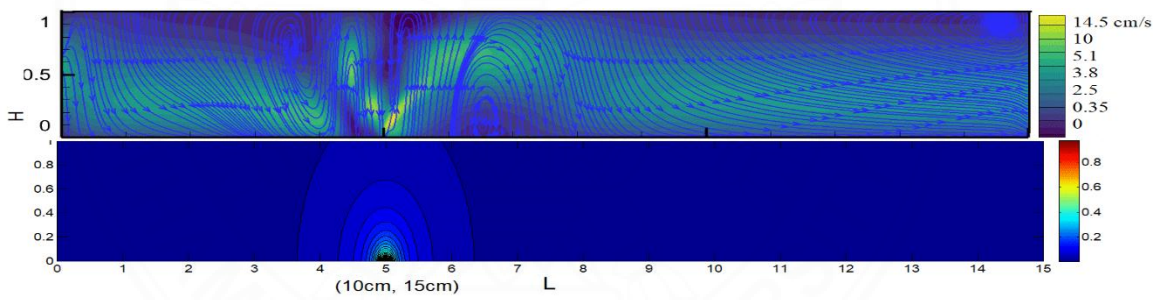


b)

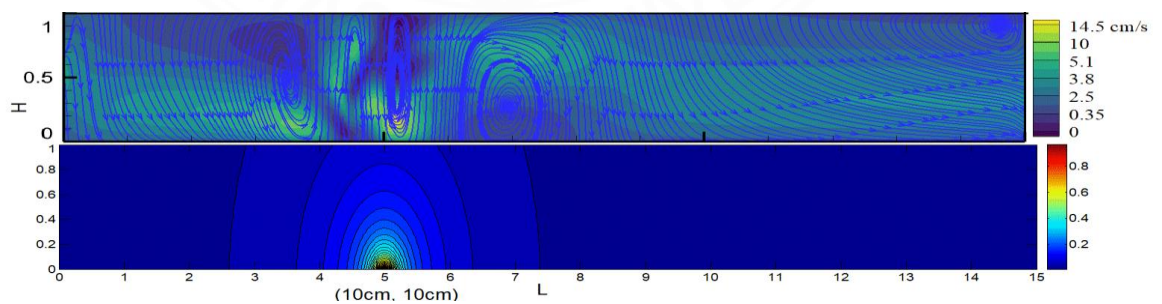


c)

**Figure 3.11** Streamlines of the blood flow:  $B = 1.0$ , a)  $b=15$ , b)  $b=10$ , c)  $b=5$ .



a)



b)

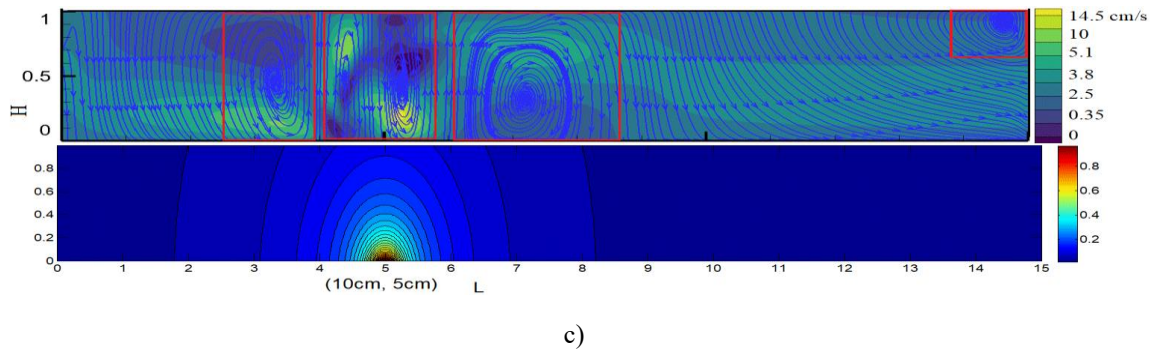


**Figure 3.12** Streamlines of the MN flow:  $B = 1.0$ , a)  $b=15$ , b)  $b=10$ , c)  $b=5$ .

### 3.7.2.3 Impact of the Size of the MN on the Blood Flow

Consider  $(a,b)=(10, 10)$ ,  $C_v = 0.04$ ,  $B = 0.5$ , and  $Re \approx 250$ . Consider 3 cases.

Case 1:  $d = 250$ ,  $\bar{u}_r = 3.8$ ,  $St \approx 3.56 \times 10^{-5}$ ,  $Re_p \approx 9.8 \times 10^{-4}$ ,  $f = 1$ .

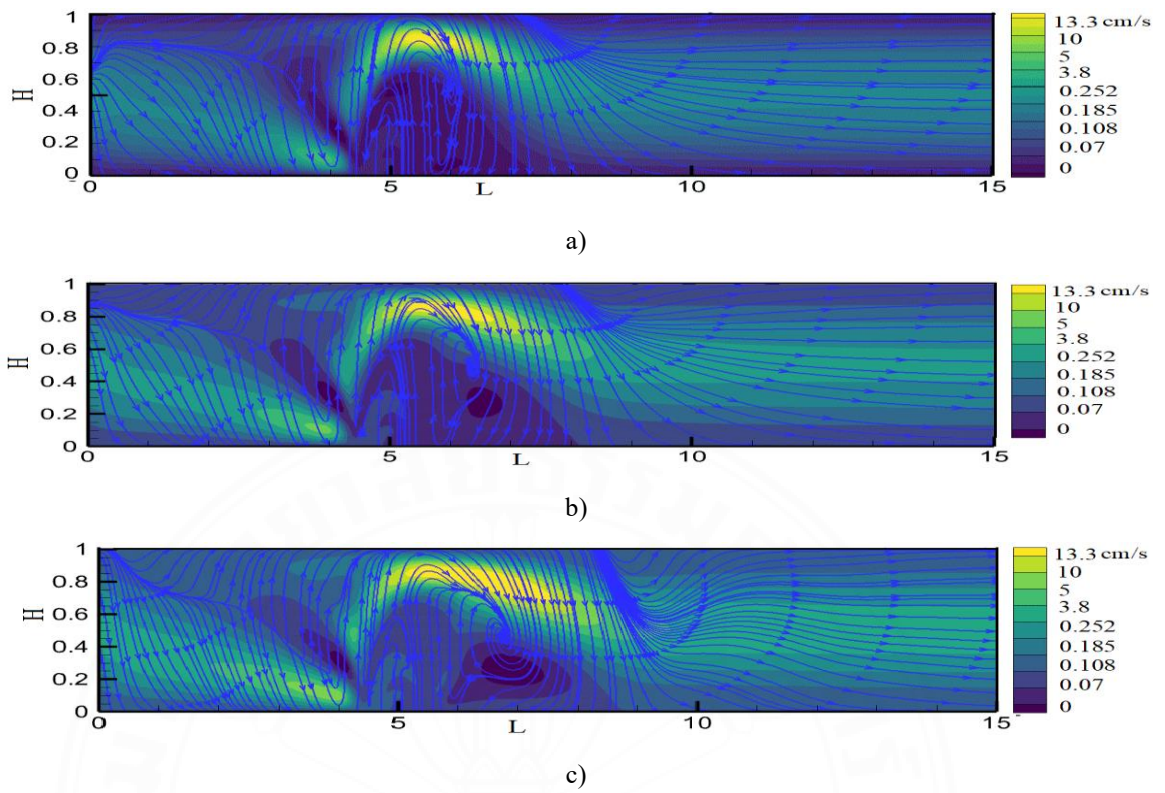
Case 2 :  $d = 800$ ,  $\bar{u}_r = 3.8$ ,  $St = 1.14 \times 10^{-4}$ ,  $Re_p \approx 3.1 \times 10^{-3}$ ,  $f = 1$ .

Case 3 :  $d = 20,000$ ,  $\bar{u}_r = 3.8$ ,  $St = 2.8 \times 10^{-2}$ ,  $Re_p \approx 1.0$ ,  $f = 1.1$ .

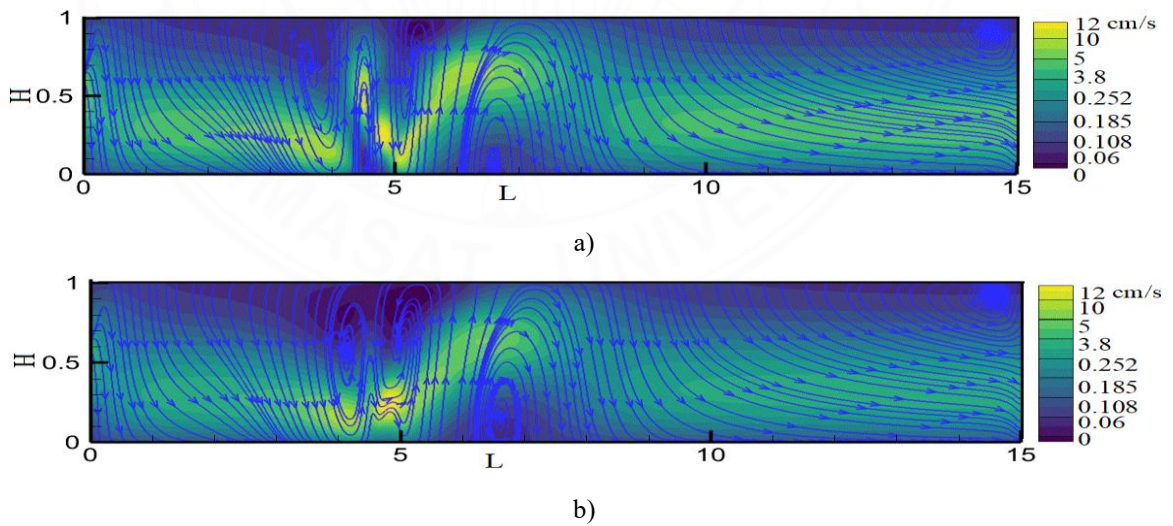
The magnetic numbers  $M_{nF} = 3281$ ,  $M_{nF_p} \approx 6677$ . The streamlines of the blood flow for Cases 1, 2, and 3 are shown in **Figure 3.13**. Clearly, the size of the MN has a significant impact on the blood flow. The circulation is characterized by vortices nearby the magnet and the backflows. The TMDD zone does not change significantly. However, the region having the maximum velocity of about 13 cm/s (yellow highlight) grows as the size of the MN increases. The region has increased by approximately 35%.

**Figure 3.14b** ( $d=800$ ) shows three well-defined vortices, whereas **Figure 3.14c** ( $d=20000$ ) shows two vortices moving in the opposite (clockwise and anticlockwise) directions. The MN flow is toward the TMDD regions with a maximum velocity of about 12 cm/s near the position of the magnet. The blood/MN flow in **Figures 3.13c** and **3.14c** may be suitable for TMDD for the particular Reynolds numbers.





**Figure 3.13** Streamlines of the blood for different sizes of the MN: a)  $d = 250$ , b)  $d = 800$ , c)  $d = 20000$ ,  $t_s \approx 1.0$ .



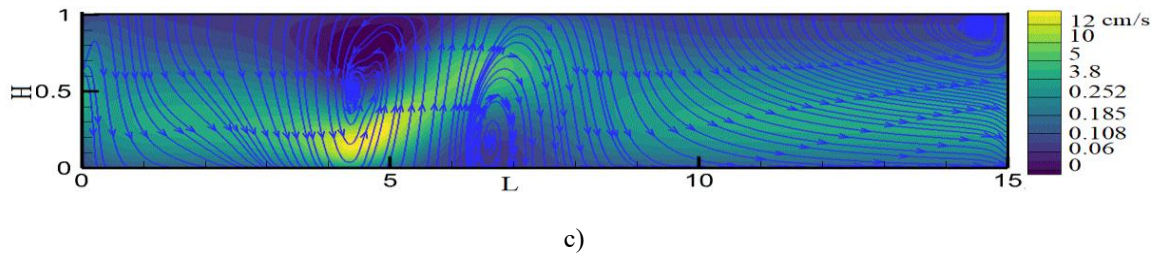


**Figure 3.14** Streamlines of the MN for different sizes of MN:

a)  $d=250$ , b)  $d=800$ , c)  $d=2000$ .

### 3.7.2.4 Impact of the Size of the MN on the Temperature

Consider  $Re=25$ ,  $B = 0.5$ , and  $C_v = 0.04$ . The initial temperature is  $T(x, y, 0) = 37$

. The boundary conditions are  $T(x, y, t) \Big|_{\text{left boundary}} = 37^\circ C$ ,  $\frac{\partial T}{\partial n} \Big|_{\text{other boundaries}} = 0$ .

Further,  $Re_p \approx 0.01$ ,  $Re = 250$ ,  $u_r = u_{r1} = 3.8$ ,  $Pr = 25$ ,  $Ec = 4.2 \times 10^{-5}$ ,  $M_{nF} = 3281$ , and  $M_{nF_p} \approx 6677$ .

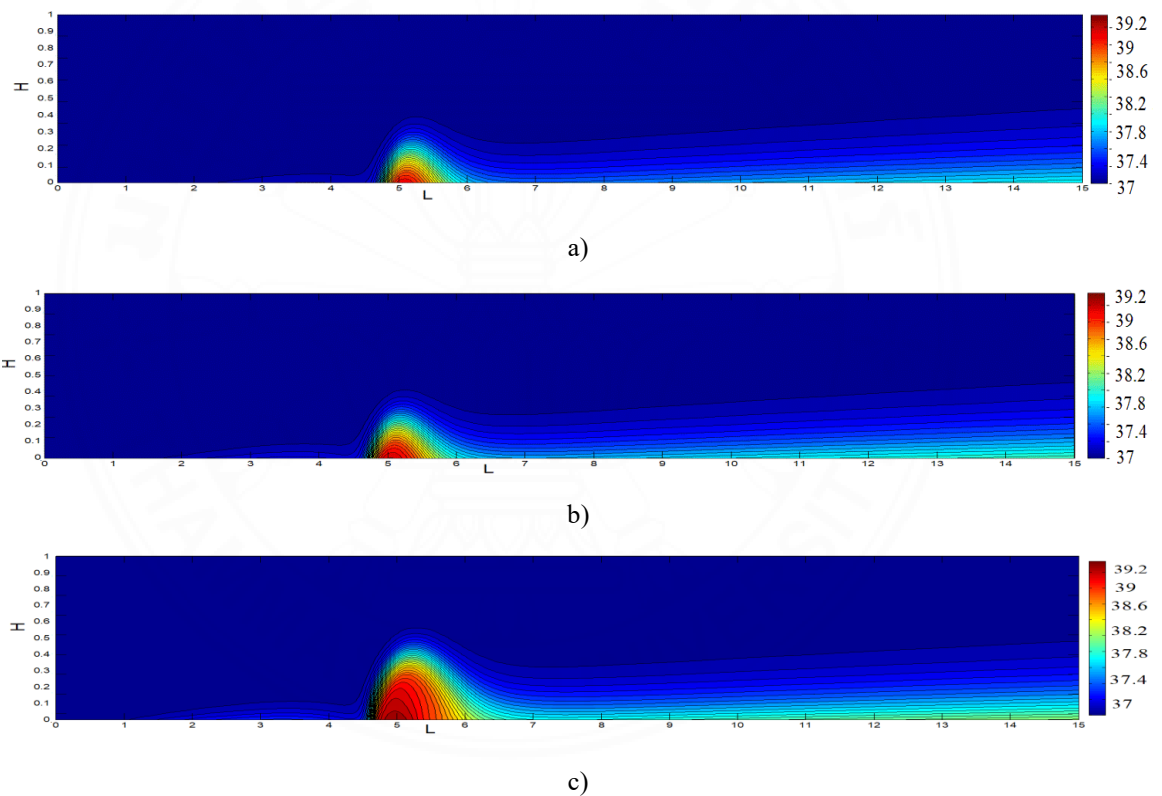
The thermal conductivity of blood increases with an increase in the size of the MN. Recall that the exchange of the energy between the blood and the MN is proportional to parameter  $\beta_2$  (see Equations (3.38a)-(3.39a)). This parameter is evaluated by (Gireesha et al., 2017) as follows:

$$\beta_2 = \frac{6\bar{k}}{d^2} \left( 2.0 + 0.6Re_p^{1/2} Pr^{1/3} \right) \frac{\bar{h}}{\bar{u}_r} \quad (3.46)$$

Hence, the exchange is proportional to  $1/d^2$ . The impact of the size of the MN on the temperature profile is illustrated in **Figures 3.15** and **3.16**. The temperature increases in the vicinity of the strong MF due to the magnetocaloric effect and the energy exchange defined by Equation (3.44). The maximum increase in temperature inside the lower vortex is  $2.1^\circ C$ , from  $37$  to  $39.1^\circ C$ . The case of  $\beta_2 = 0$  in **Figure 3.15a** (magnetocaloric effect)



complies with the results of Tzirtzilakis (2008). For  $d=250$ , the temperature starts increasing in the MF region at  $t \approx 13$  min and reaches approximately  $39.1^\circ\text{C}$  at the steady state,  $t \approx 1.5$  h. When  $d=800$ , the temperature reaches a maximum of about  $39.1$  at  $t \approx 1.5$  whereas  $d=20000$  requires only 0.5 h. The maximum temperature of the MN reaches approximately  $38.8^\circ\text{C}$  with negligible differences in the second digit after the decimal point for different  $d$  (**Figure 3.16**). Such a temperature increase may have a negative impact on long-term treatments such as chemotherapy. As an example, we refer to the effects of the MRI with the MF and 4 T (Schenck et al. 1992; Yamamoto et al. 2004). The patients report sensations of nausea, vertigo, metallic taste, or sleepiness after treatments.



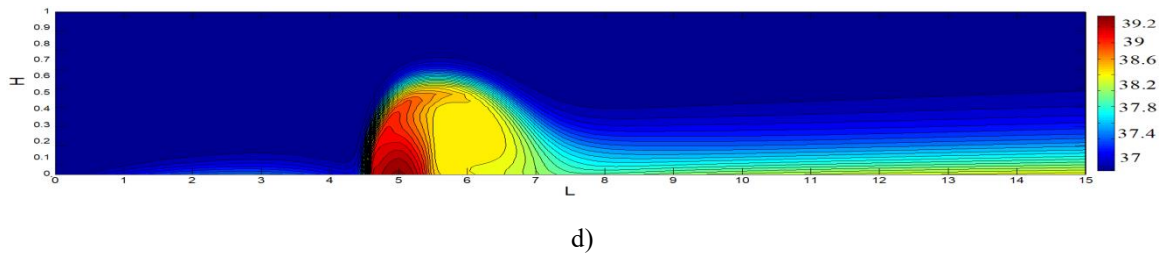


**Figure 3.15** Temperature of the blood flow: a)  $\beta_2 = 0$ , b)  $d=250$ , c)  $d=800$ , d)  $d=20000$ .

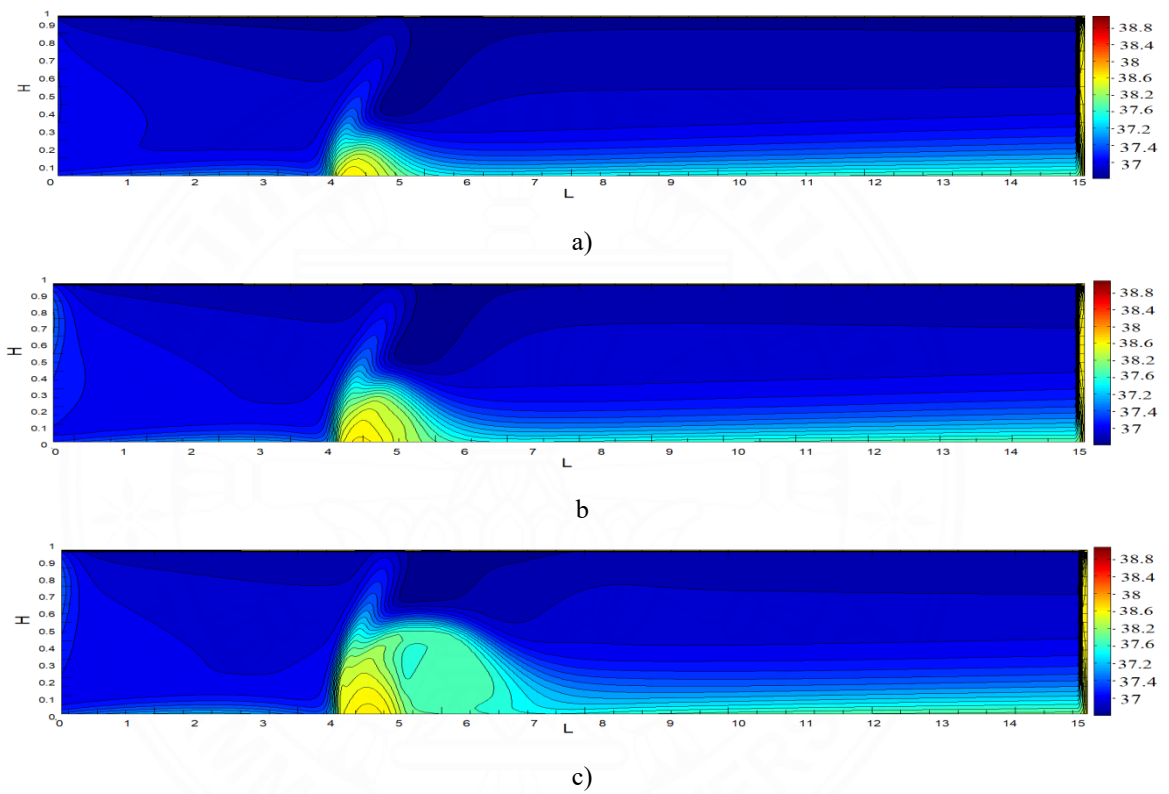


**Figure 3.16** Temperature of the MN flow: a)  $d=250$ , b)  $d=800$ , c)  $d=20000$ .

**Table 3.4** Parameters encountered in TMDD.

Parameters	Symbol	Non-Dimensional Parameter Range	Dimensional Parameter Ranges
Maximum Entrance Blood Velocities	$\bar{u}_r$	-	3-15
Maximum Entrance MN Velocities	$\bar{u}_{r1}$	-	3-15
Vessel Height	$\bar{h}$	1	$0.2 \leq \bar{h} \leq 2.0$
Vessel Length	L	15	$3 \leq L \leq 40$
Magnetic Field Strength	$\bar{B}$	-	$0.5 \leq \bar{B} \leq 5$
Magnetization	$\bar{M}$	-	$\bar{M} = 448$
Distance in x-direction from Magnet	$\bar{a}$	1.5-5	3-10
Distance in y-direction from Magnet	$\bar{b}$	$-0.01 \leq b \leq -0.1$	$3 \leq b \leq 15$
Average Free Path of MN	$\lambda_a$	-	200
Density of Blood	$\bar{\rho}$	-	1050
Density of MN	$\bar{\rho}_p$	-	5200
Normal Body Temperature	$\bar{T}$	-	37
Dynamic Viscosity of Blood	$\bar{\mu}$	-	$3.2 \times 10^{-3}$

Thermal Conductivity of Blood	$\bar{k}$	-	$2.2 \times 10^{-3}$
Heat Capacity of Blood	$\bar{c}$	-	14.65
Heat Capacity of MN	$\bar{c}_p$	-	670



## CHAPTER 4

### A THREE-LAYER MODEL OF MAGNETIC TARGETED DRUG DELIVERY

#### 4.1 Introduction

In this chapter, a three-layer mathematical model for the mass transport of drug-loaded magnetic nanoparticles (MN) from blood vessel (artery) to endothelial membrane and tissue for magnetic targeted drug delivery (MTDD) is proposed. The mass transport equations are coupled with the momentum equation of the blood flow and the drug-loaded MN. The blood and tumor vessels are notoriously leaky. The numerical procedure employs the stream function–vorticity formulation and an efficient pseudo transient numerical method on a finite-difference grid. The model validated by existing experimental results has been applied to analyze the impact of magnetic force (MF), and the position of the magnet for accumulation of the MN in the required regions (tumor). The concentration of MN is controlled by the variable magnetic field, which has been shown much promise for an efficient MTDD.

#### 4.2 Mathematical Formulation

A three layers mathematical formulation is developed for the description of drug-loaded MN transport in the blood vessel (artery), coupled with the mass transport in the three layers blood vessel, endothelial membrane and tissue (**Figure 1**).

##### 4.2.1 Governing Equations

For this purpose, we consider viscous, unsteady, two phase flow consisting of the drug-loaded MN and the blood in a three layer rectangular channel with length  $\bar{L}$  and height  $\bar{h}$  (**Figure 1**). The flow is assumed to be fully developed at the entrance of the artery

wall, and only the drug-loaded MN moves out of the blood vessel to endothelium membrane and tissue (Nacev et al., 2011b). The volumetric blood flow rates out of the artery-tissue are assumed zero. The governing equation of the two-phase flow is given with regard to the velocity  $\mathbf{V} = (\bar{u}, \bar{v})$  of the blood and the particles (Tzirtzilakis, 2005). The subscript  $p$  indicates the parameters of the MN flow.

$$\nabla \cdot \mathbf{V} = 0, \quad (4.1)$$

$$\bar{\rho} \left( \frac{\partial \bar{\mathbf{u}}}{\partial t} + \mathbf{V} \cdot \nabla \mathbf{V} \right) = -\nabla \bar{p} + \bar{\mu} \nabla^2 \mathbf{V} + \mathbf{F} + \bar{\mu}_0 (\mathbf{M} \cdot \nabla) \mathbf{H}, \quad (4.2)$$

The drag force used to solve this problem is the same as defined in previous Chapter 3 in equation (3.4), while the only  $\bar{\rho}_{mp} = \bar{\rho}_p$ , and  $\bar{\rho}_{mp}$  is therapeutic drug-loaded MN.

The solid phases, i.e., the MN in blood are simulated by the momentum equation, assuming that the impact of the dynamic viscosity is negligible. Hence, the solid phase equations are given by:

$$\nabla \cdot \mathbf{V}_p = 0, \quad (4.3)$$

$$\bar{\rho}_{mp} C_v \left( \frac{\partial \mathbf{V}_p}{\partial t} + \mathbf{V}_p \cdot \nabla \mathbf{V}_p \right) = -(1 - C_v) \mathbf{F} + C_v \bar{\mu}_0 \mathbf{V}_{vp} (\mathbf{M} \cdot \nabla) \mathbf{H}, \quad (4.4)$$

where  $\mathbf{V}_{vp}$  is the volume of MN.

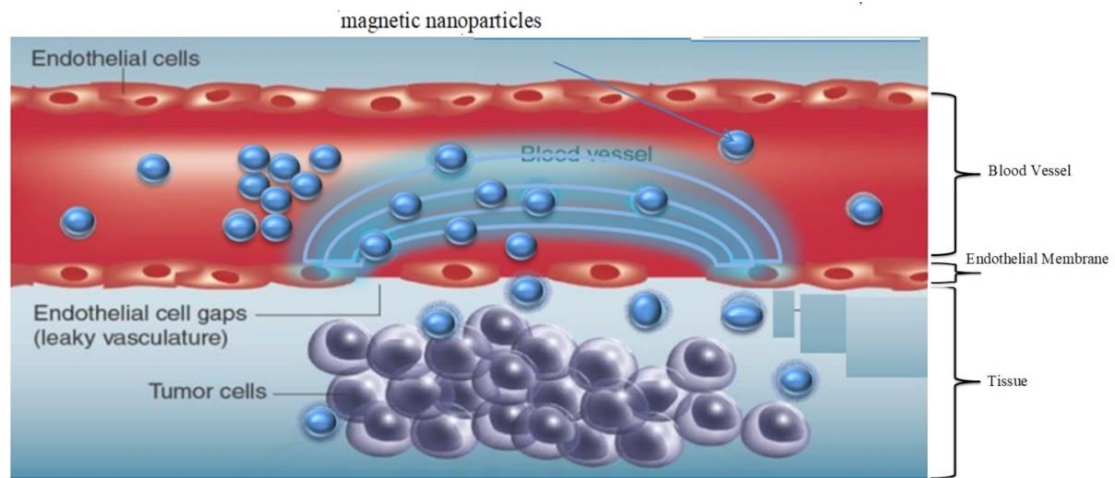


**Figure 4.1** Blood vessel, endothelial membrane and tissue.

#### 4.2.2 Magnetic Field

Following Tzirtzilakis (2005), and Bose & Banerjee (2015), the magnetic source placed perpendicular to the  $(x, y)$  plane and  $\vec{H}$  is derived from same equations (3.9) and (3.11) as in previous Chapter 3.

Nevertheless, magnetization is the calculation of how much the MF affects the blood and MN. For isothermal case, magnetization is described by the simplest equations (Tzirtzilakis, 2005; Bose & Banerjee, 2015).

$$\vec{M} = \chi_1 \vec{H}, \quad (4.5)$$

$$\vec{M} = \chi_{eff} \vec{H}, \quad \chi_{eff} = \left[ \chi_2 / (1 + (\chi_2/3)) \right], \quad (4.6)$$

where  $\chi_2$  are the magnetic susceptibility of the MN.

#### 4.2.3 Therapeutic Drugs Concentration

For MTDD, the nanoparticles containing magnetic core is given by

$$\bar{\rho}_{mp} = \bar{\rho}_{p(core)} (\bar{d}_m)^3 + \rho_{shell} (1 - \bar{d}_m)^3, \quad (4.7a)$$

where  $\bar{d}_m$  is the ratio of magnetic-core ( $\bar{d}$ ) and total diameters ( $\bar{d}_{mp}$ ) of MN, defined as  $d_m = \bar{d} / \bar{d}_{mp}$ . For  $d_{mp} = 1$ , we have fully MN, whereas, for  $d_{mp} = 0$ , we have magnetically neutral nanoparticles. The shell is a mixture of medical therapeutic drugs and carriers. The shell density (Kenjeres & Tjin, 2018) is given by:

$$\rho_{shell} = \left( \frac{f_1}{\rho_{drug}} + \frac{1-f_1}{\rho_{carrier}} \right)^{-1}, \quad (4.7b)$$

where  $f_1$  is the fractional loading of the magnetic therapeutic drug within the shell layer. In the present work, the magnetic core is made from the ferromagnetic nanoparticles ( $\text{Fe}_3\text{O}_4$ ), with the density of  $\bar{\rho}_{p(core)} = \bar{\rho}_p = 5200 \text{ kg/m}^3$ , magnetic susceptibility  $\chi_2 = 20$ , and saturation magnetization  $\bar{M}_{sat} = 448 \text{ kA/m}$ . The shell carrier is biodegradable, which can be poly(lactide-co-glycolide) (PLGA) or poly(ethylene) glycol (PEG). The densities of PLGA and PEG are  $\bar{\rho}_{carrier} = 1300 \text{ kg/m}^3$  and  $\bar{\rho}_{carrier} = 1126 \text{ kg/m}^3$ . The fractional loading of the medical therapeutic drug is taken to be  $f_1 = 30\%$ , which corresponds to an antitucular drugs, with a typical density of  $\bar{\rho}_{drug} = 1610 \text{ kg/m}^3$ .

#### 4.2.4 Drag coefficient

The associated drag coefficient is different from Chapter 3 due to the drug-loaded MN contributed in a different way in Stokes' resistance law:

$$\bar{F}_D \approx f \frac{1}{\tau_p} = \frac{18\bar{\mu}}{\bar{d}_{mp}^2 \bar{\rho}_{mp} C_c}, \quad (4.8)$$

The Cunningham correction coefficient is also changed to:



$$C_c = 1 + \frac{2\lambda_a}{\bar{d}_{mp}} \left( 1.257 + 0.4e^{-\frac{11\bar{d}_{mp}}{\lambda_a}} \right). \quad (4.9)$$

Similarly,

$$\text{Re}_p = \frac{\bar{d}_{mp}\rho}{\mu} \tilde{u}_0, \quad (4.10)$$

Hence, other terms in equations (4.8) and (4.10) are defined the same as in previous Chapter 3.

#### 4.2.5 Mass Transport Through Blood Vessel

Following buongiorno (2006) and Nacev et al. (2011),  $\bar{C}_M(\bar{x}, \bar{y}, \bar{t})$  denotes the concentration of drug-loaded MN inside the blood vessel.

$$\frac{\partial \bar{C}_M}{\partial \bar{t}} + \nabla \cdot (\mathbf{V} \bar{C}_M + \mathbf{V}_p \bar{C}_M) = (\nabla \cdot D_{Tot} \nabla \bar{C}_M), \quad (4.11a)$$

where  $\mathbf{V}_p = (\bar{u}_p, -\bar{v}_p)$ , and  $D_{Tot}$ , is the total diffusion coefficient in blood (DCB), which is the sum of Brownian diffusion (BD) and scattering diffusion (SD)  $D_{Tot} = D_B + D_S$ .

The negative sign with  $(-\bar{v}_p)$  shows the downward pull of magnetic force on drug-loaded MN. The BD is written as:

$$D_B = \frac{\bar{\rho} k_B T}{3\pi\bar{\mu}\bar{d}_{mp}}, \quad (4.11b)$$

where  $k_B$ ,  $T$ , are the Boltzmann constant and the normal body temperature. For 250 nm sizes of drug-loaded MN at body temperature (37°C), the diffusion coefficient is  $D_B \approx 7 \times 10^{-11} \text{ m}^2/\text{s}$ , and the SD causes due to the collision of drug-loaded MN with the

RBC is approximately  $D_S \approx 10^{-11} - 10^{-10} \text{ m}^2/\text{s}$  (Nacev et al., 2011). Here,  $C_v$  strongly depends on  $C_M$  for drug-loaded MN concentration such that  $C_v = \bar{C}_M \mathbf{V}_p$ . Therefore, Equation (4.11) is strongly coupled with Equations (4.2) and (4.4).

#### 4.2.6 Mass Transport Through Endothelium Membrane

In endothelium membrane, only the mass transport of drug-loaded MN within the membrane is derived by the reduced concentration equation:

$$\frac{\partial \bar{C}_{MM}}{\partial t} + \nabla \cdot (\mathbf{V} \bar{C}_{MM} + \mathbf{V}_p \bar{C}_{MM}) = D (\nabla \cdot D_{Tot} \nabla \bar{C}_{MM}), \quad (4.12a)$$

where  $\mathbf{V} = (0, -\bar{v})$ ,  $\mathbf{V}_p = (0, -\bar{v}_p)$ , and  $D$  is the Renkin reduced diffusion coefficient (RRDC) for endothelium membrane diffusivity (EMD). Moreover,  $D$  is the ratio of diffusion coefficient in the membrane (DCM) to the total DCB, which is defined as:

$$D = \frac{D_M}{D_B + D_S} = \frac{D_M}{D_{Tot}}, \quad (4.12b)$$

where  $D_M$  is the DCM, and the value of  $D$  varies between 0 and 1. As the value decreases toward zero, the drug-loaded MN stays inside the blood vessel, while the drug-loaded MN begins to leave the blood vessel and enters the membrane when the value decreases toward unity.

The value of  $D_M$  depends on the pores inside the endothelium membrane. If the diameters of pores are known, the DCM can be calculated by the following correlation:

$$D_M = D_B (1 - \alpha^2) (1 - 2.1044\alpha + 2.089\alpha^3 - 0.948\alpha^5), \quad (4.12c)$$

where  $\alpha = \bar{d}_{mp} / \bar{d}_{pore}$ , and  $\bar{d}_{pore}$  the average diameter of the endothelial pores. For normal pores diameters,  $\alpha \approx 1 \Rightarrow D_M \approx 0 \Rightarrow D \approx 0$ . The diameters of drug-loaded MN should be smaller than pores diameter. The normal and leaky cell pore sizes are 60 nm and 600 nm.

#### 4.2.7 Mass Transport Through Tissue

Unlike the healthy tissue which is a fine network of capillaries. The region around the tumor is often characterized by irregular and poor blood supply that reduces the concentration of drugs. The dynamics of tumor is supposed to be modeled by the source term in reaction–diffusion equation.

$$\frac{\partial \bar{C}_{MT}}{\partial \bar{t}} + \nabla \cdot (r_F \mathbf{V} \bar{C}_{MT} + r_p \mathbf{V}_p \bar{C}_{MT}) = D_\tau (\nabla \cdot D_{Tot} \nabla \bar{C}_{MT}) + \varphi_s, \quad (4.13a)$$

where  $\mathbf{V} = (0, -\bar{v})$ ,  $\mathbf{V}_p = (0, -\bar{v}_p)$ , and  $D_\tau$  is the RRDC for tissue diffusivity (TD) compared to blood.  $r_F$  is the retardation factor accounting for the resistance of convective transport of drug-loaded MN due to the reflection by porous tissue. In tissue, the retardation effect is negligible; therefore,  $r_F \approx 1$  (Baxter & Jain, 1990, 1991).  $\varphi_s$  is the source term.

Further, the RRDC for TD is the ratio of diffusion coefficient in the tissue (DCT) to the total DCB.

$$D_\tau = \frac{D_T}{D_{Tot}}, \quad (4.13b)$$

where  $D_T$  is the DCT, which is calculated by the Fiber Matrix Model (Fournier, 2012).

$$D_T = D_B \exp \left[ - \left( 1 + \frac{\bar{d}_{mp}}{\bar{d}_f} \right) \nu^{1/2} C_F^{1/2} \right] = D_B \exp \left[ - \left( 1 + \frac{\bar{d}_{mp}}{\bar{d}_f} \right) \phi^{1/2} \right], \quad (4.13c)$$

where  $\bar{d}_f$  is the diameter of long fiber cylinder,  $\nu$  is specific volume of the fiber,  $C_F$  is the fiber concentration, and  $\varphi$  is the volume fraction of tissue fibers. The TD is highly dependent upon the sizes of MN and extracellular spacing (Nacev et al., 2011).

The source term in equation (13a) is the addition of the tissue vascular, lymphatic, and cellular contributions (Jain & Stylianopoulos, 2010; Sefidgar et al., 2014; Carlier et al., 2017).

$$\varphi_s = \left[ \frac{P_i S}{V} (\bar{C}_p - \bar{C}_{MT}) + \varphi_B (1 - \sigma_f) \bar{C}_p \right] - \varphi_L C_{MT} - \beta_L \bar{C}_{MT}, \quad (4.13d)$$

where the terms in the bracket accounts for the tissue vascular contribution and the last two terms are the lymphatic and cellular contributions.  $\beta_L$  the drugs elimination constant (1/s)

,  $\frac{S}{V}$  is the vasculature surface area per unit volume (1/m),  $P_i$  vascular permeability

(m/s) which is calculated by  $P_i = \frac{D_M}{hD_B}$ .

$\sigma_f$  is the osmotic reflection coefficient for drug-loaded MN.  $\bar{C}_p$  is assumed zero due to the small concentration of drug in plasma (Steuperaert et al., 2017).  $\varphi_B, \varphi_L$  are the volumetric flow rates of blood plasma and interstitial fluids out of the lymphatic vessels per unit volume of the tumor media. Due to the absence of functional lymphatic inside tumor,  $\varphi_L$  are set to zero. After substituting all the parameters in equation (13c), the source term is reduced as:

$$\varphi_s = - \left( \frac{P_i S}{V} + \beta_L \right) \bar{C}_{MT} = -\varphi_p \bar{C}_{MT}, \quad (4.13e)$$

**Table 4.1** Model parameter values.

Parameter	Symbol	Condition	Value
Brownian Diffusion	$D_B$	-	$1 \times 10^{-14} - 1 \times 10^{-12}$
Scattering Diffusion	$D_S$	-	$3.5 \times 10^{-11} - 6 \times 10^{-10}$
Diffusion Coefficient (in Membrane)	$D_M$	Normal Cell if $\bar{d}_{mp} = \bar{d}_{pore}$ or $\bar{d}_{mp} > \bar{d}_{pore}$	0
		Leaky or Tumor cell if $\bar{d}_{mp} < \bar{d}_{pore}$	$-1.5 \times 10^{-12}$
Diffusion Coefficient (in Tissue)	$D_T$	Normal Cell if $\bar{d}_{mp} = \bar{d}_{pore}$ or $\bar{d}_{mp} > \bar{d}_{pore}$	0
		Leaky or Tumor cell if $\bar{d}_{mp} < \bar{d}_{pore}$	$-1.2 \times 10^{-14}$
Total Diffusion Coefficient (in Blood)	$D_{Tot} = D_B + D_S$	-	$1 \times 10^{-14} - 6 \times 10^{-10}$
Boltzmann Constant	$k_B$	-	$1.380649 \times 10^{-23}$ J
Diameter of Endothelial Pores	$\bar{d}_{pore}$	Normal Cell	60
		Leaky or Tumor cell	300
Diameter of drug-loaded MN	$\bar{d}_{mp}$	1. ( $\bar{d}_{mp} < \bar{h}$ ) 2. ( $\bar{d}_{mp} < \bar{d}_{leaky\ pore}$ )	$10 \leq \bar{d}_{mp} \leq 7000$
		Normal Cell	20

Diameter of Long Fiber Cylinder	$\bar{d}_f$	Leaky or Tumor Cell	100
Volume Fraction of Tissue Fibers	$\varphi$	Normal Cell	-
		Leaky or Tumor Cell	0.66
Drugs Elimination Constant	$\beta_L$	-	$7.32 \times 10^{-4}$
Vasculature Surface Area per unit Volume	$\frac{S}{V}$	-	$2 \times 10^4$
Magnetic-core of MN	$d_m$	-	
Density of Magnetic-core of MN	$\bar{\rho}_{p(core)}$	-	5200
Density of Anti-Tubercular Drug	$\bar{\rho}_{drug}$	-	1610
Density of Shell Carrier PLGA	$\bar{\rho}_{carrier}$	-	1300
Density of Shell Carrier PEG	$\bar{\rho}_{carrier}$	-	1126
Fractional Loading of the Magnetic Therapeutic Drug	$f_1$	-	30%

### 4.3 Boundary and Initial Conditions

At all the external boundaries of the vessel-tissue, the normal diffusive flux is set to zero, and MN enters the channel with constant vessel inlet concentration. The boundary conditions (BCs) are as follow:

$$\begin{aligned} \text{Inflow} \quad \bar{x} = 0, 0 \leq \bar{y} \leq \bar{h}: \quad & \bar{u} = \bar{u}_p = \bar{u}_0(\bar{y}), \bar{v} = \bar{v}_p = 0; \\ & \bar{C}_M = \bar{C}_0(\bar{y}), \mathbf{n} \cdot (D\nabla \bar{C}_i) = 0, \bar{C}_i = \bar{C}_{MM}, \bar{C}_{MT}. \end{aligned} \quad (4.14)$$

$$\begin{aligned} \text{Outflow} \quad \bar{x} = \bar{L}, 0 \leq \bar{y} \leq \bar{h}: \quad & \frac{\partial \bar{R}}{\partial \bar{x}} = 0, \mathbf{n} \cdot (D\nabla \bar{C}_i) = 0, \\ & R = \bar{u}, \bar{v}, \bar{T}, \quad \bar{C}_i = \bar{C}_M, \bar{C}_{MM}, \bar{C}_{MT}. \end{aligned} \quad (4.15)$$

$$\text{Upper Wall} \quad \bar{y} = 0, 0 \leq \bar{x} \leq \bar{L}: \quad \bar{u} = \bar{u}_p = 0; \bar{v} = \frac{\partial \bar{v}_p}{\partial \bar{y}} = 0. \quad (4.16)$$

$$\text{Lower Wall} \quad \bar{y} = \bar{h}, 0 \leq \bar{x} \leq \bar{L}: \quad \bar{u} = \bar{u}_p = 0; \bar{v} = \frac{\partial \bar{v}_p}{\partial \bar{x}} = 0. \quad (4.17)$$

$$\begin{aligned} \text{Initial Conditions} \quad 0 \leq \bar{x} \leq \bar{L}, 0 \leq \bar{y} \leq \bar{h}: \quad & \bar{u} = \bar{v} = 0; \bar{u}_p = \bar{v}_p = 0; \\ & \bar{C}_M = \bar{C}_0; \bar{C}_{MM} = \bar{C}_{MT} = 0 \quad \text{at } t = 0. \end{aligned} \quad (4.18)$$

$\bar{u}_0(\bar{y})$  is the velocity at the inflow boundary, and is the total flux of MN and  $\bar{C}_0$  is the initial constant concentration.

The concentration at the interior boundaries between artery lumen, and endothelial membrane, and the endothelial membrane and tissue, satisfy the condition: the mass transport of MN that leaves one domain enters another (no MN concentration is lost or created). Therefore, the BCs are

$$\text{Upper Wall} \quad \mathbf{n} \cdot (D_{Tot} \nabla \bar{C}_M) = 0, \mathbf{n} \cdot (\mathbf{V}_p \bar{C}_i) = \mathbf{J}_i, \bar{C}_i = \bar{C}_{MM}, \bar{C}_{MT}. \quad (4.19)$$

$$\text{Lower Wall} \quad \mathbf{n} \cdot (D_\tau \nabla \bar{C}_{MT}) = 0, \mathbf{n} \cdot (\mathbf{V}_p \bar{C}_i) = \mathbf{J}_i, \bar{C}_i = \bar{C}_M, \bar{C}_{MM}. \quad (4.20)$$

The total flux of MN out of the artery lumen to endothelium membrane and tissue is equal to the convective flux created by the MF and MN leave only when the MF pulls them to the region of infection. The flow domain and boundary conditions are shown in **Figure 2**.

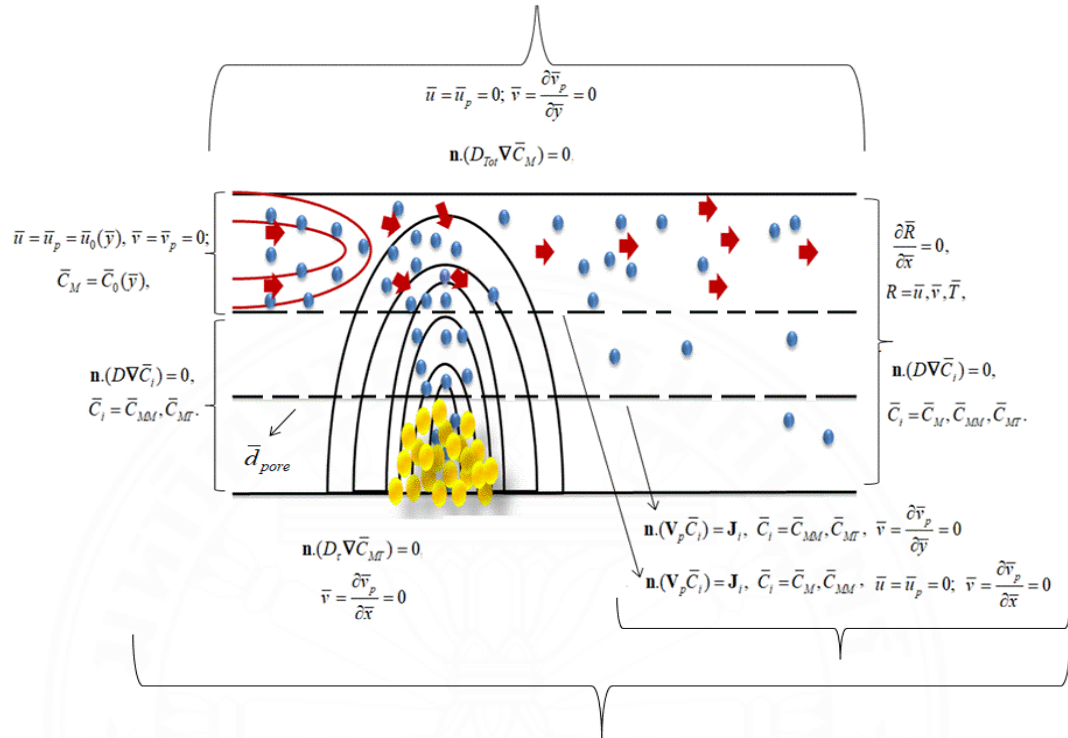


**Figure 4.2** Flow domain and boundary conditions.

#### 4.4 Special Case: MHD

For the special case: uniform magnetic field throughout the channel is considered. Two types of magnetic forces will act on the MN-blood as it flows under the influence of an external MF. The first is the magnetization force, which occurs when erythrocytes are oriented with MF, and the second is the Lorentz force (see Aaiza et al., 2016). The Lorentz force ( $\mathbf{J} \times \mathbf{B}$ ) arises due to the electric current generated by moving ions in blood plasma, where  $\mathbf{J} = \sigma(\mathbf{V} \times \mathbf{B})$ , and  $\sigma = 0.7 \text{ S/m}$  is electrical conductivity of the blood.



Consequently, the Lorentz force will only occur if the velocities of the moving ions are perpendicular to the plane of an external MF. Hence, the systems of the governing equations are: (Tzirtzilakis, 2005)

$$\nabla \cdot \mathbf{V} = 0, \quad (4.21)$$

$$\bar{\rho} \left( \frac{\partial \bar{u}}{\partial t} + \mathbf{V} \cdot \nabla \mathbf{V} \right) = -\nabla p + \bar{\mu} \nabla^2 \mathbf{V} + \mathbf{F} + \bar{\mu}_0 \bar{M} \nabla H - \bar{\sigma} \bar{B}^2 \mathbf{V}, \quad (4.22)$$

The electric conductivity of magnetic nanoparticles is determined by the temperature of the surrounding environment ( $\text{Fe}_3\text{O}_4$ ). It has a conducting nature at room temperature, but an insulator at temperatures below 120K (-153.15°C). T=310K is a normal body temperature. It is, however, prepared for TMDD. Although, drugs bind to the surface of MN, its electric conductivity may change. In this case, we also considered electrically conductive  $\text{Fe}_3\text{O}_4$  MN ( $\sigma_p = 12000\text{S/m}$ ) (see Aaiza et al. 2016). Thus, the solid phase equations are given by:

$$\nabla \cdot \mathbf{V}_p = 0, \quad (4.23)$$

$$\rho_p C_v \left( \frac{\partial \mathbf{V}_p}{\partial t} + \mathbf{V}_p \cdot \nabla \mathbf{V}_p \right) = -(1 - C_v) \mathbf{F} + C_v \bar{\mu}_0 \bar{M} \nabla H - C_v \bar{\sigma}_p \bar{B}^2 \mathbf{V}_p, \quad (4.24)$$

#### 4.5 Dimensionless Equations

In this problem, the same dimensionless variables equation (3.22) as in previous Chapter together with equation (3.24) are used to transform the continuity, momentum and concentration equations (4.1)-(4.4) and (4.11)-(4.24) into:

$$C_M = \frac{\bar{C}_M}{C_0}, C_{MM} = \frac{\bar{C}_{MM}}{C_0}, C_{MT} = \frac{\bar{C}_{MT}}{C_0}. \quad (4.25)$$

almost all notations are self-explanatory,  $\bar{H}_r$  is the strength of the MF at  $(a, b)$ . Mapping in equations (3.30) and (3.34) are derived the same as in Chapter 3, some calculus yields (3.30)-(3.34)

$$\frac{\partial u}{\partial x} w_x + \frac{\partial u}{\partial y} w_y = 0, \quad (4.26a)$$

$$\frac{\partial v}{\partial x} w_x + \frac{\partial v}{\partial y} w_y = 0, \quad (4.26b)$$

$$\frac{\partial u_p}{\partial x} w_x + \frac{\partial u_p}{\partial y} w_y = 0, \quad (4.27a)$$

$$\frac{\partial v_p}{\partial x} w_x + \frac{\partial v_p}{\partial y} w_y = 0, \quad (4.27b)$$

$$\begin{aligned} \frac{\partial u}{\partial t} = w_x^2 \frac{\partial^2 u}{\partial x^2} + w_y^2 \frac{\partial^2 u}{\partial y^2} + w_\xi \frac{\partial u}{\partial x} + w_\eta \frac{\partial u}{\partial y} - \text{Re} w_x w_y \left( u \frac{\partial u}{\partial x} + v \frac{\partial u}{\partial y} \right) + \\ C_v \beta_1 D_p \text{Re} (U_2 u_p - U_2^2 u) + M_{\text{nF}} \text{Re} H w_x \left( \frac{\partial H}{\partial x} \right) - M_{\text{nM}} H^2 u, \end{aligned} \quad (4.28a)$$

$$\begin{aligned} \frac{\partial v}{\partial t} = w_x^2 \frac{\partial^2 v}{\partial x^2} + w_y^2 \frac{\partial^2 v}{\partial y^2} + w_\xi \frac{\partial v}{\partial x} + w_\eta \frac{\partial v}{\partial y} - \text{Re} w_x w_y \left( u \frac{\partial v}{\partial x} + v \frac{\partial v}{\partial y} \right) + \\ C_v \beta_1 D_p \text{Re} (U_2 v_p - U_2^2 v) + M_{\text{nF}} \text{Re} H w_y \left( \frac{\partial H}{\partial y} \right) - M_{\text{nM}} H^2 v, \end{aligned} \quad (4.28b)$$

$$\begin{aligned} \frac{\partial u_p}{\partial t} = & -\text{Re}_p d_o w_x w_y \left( u_p \frac{\partial u_p}{\partial x} + v_p \frac{\partial u_p}{\partial y} \right) - (1 - C_v) \text{Re}_p d_o \beta_1 (U_2 u_p - U_2^2 u) + \\ & \frac{1}{2} V_{vp} \text{Re}_p d_o M_{nF_p} H w_x \left( \frac{\partial H}{\partial x} \right) - \text{Re}_p d_o M_{nM_p} H^2 u_p, \end{aligned} \quad (4.29a)$$

$$\begin{aligned} \frac{\partial v_p}{\partial t} = & -\text{Re}_p d_o w_x w_y \left( u_p \frac{\partial v_p}{\partial x} + v_p \frac{\partial v_p}{\partial y} \right) - (1 - C_v) \text{Re}_p d_o \beta_1 (U_2 v_p - U_2^2 v) - \\ & \frac{1}{2} V_{vp} \text{Re}_p d_o M_{nF_p} H w_y \left( \frac{\partial H}{\partial y} \right) - \text{Re}_p d_o M_{nM_p} H^2 v_p, \end{aligned} \quad (4.29b)$$

$$\begin{aligned} \frac{\partial C_M}{\partial t} = & \frac{U_2}{Pe} \left( w_x^2 \frac{\partial^2 C_M}{\partial x^2} + w_y^2 \frac{\partial^2 C_M}{\partial y^2} + w_\xi \frac{\partial C_M}{\partial x} + w_\eta \frac{\partial C_M}{\partial y} \right) - \\ & w_x \frac{\partial C_M}{\partial x} (U_2 u + u_p) + w_y \frac{\partial C_M}{\partial y} (U_2 v + v_p), \end{aligned} \quad (4.30a)$$

$$\begin{aligned} \frac{\partial C_{MM}}{\partial t} = & D \frac{U_2}{Pe} \left( w_x^2 \frac{\partial^2 C_{MM}}{\partial x^2} + w_y^2 \frac{\partial^2 C_{MM}}{\partial y^2} + w_\xi \frac{\partial C_{MM}}{\partial x} + w_\eta \frac{\partial C_{MM}}{\partial y} \right) + \\ & (U_2 v + v_p) w_y \frac{\partial C_{MM}}{\partial y}, \end{aligned} \quad (4.30b)$$

$$\begin{aligned} \frac{\partial C_{MT}}{\partial t} = & D_\tau \frac{U_2}{Pe} \left( w_x^2 \frac{\partial^2 C_{MT}}{\partial x^2} + w_y^2 \frac{\partial^2 C_{MT}}{\partial y^2} + w_\xi \frac{\partial C_{MT}}{\partial x} + w_\eta \frac{\partial C_{MT}}{\partial y} \right) + \\ & (U_2 v + v_p) w_y \frac{\partial C_{MT}}{\partial y} - S_0 C_{MT} \end{aligned} \quad (4.30c)$$

The additional the non-dimensional parameters are as follows:

$$M_{nF} = \frac{\bar{\mu}_0 \chi_1 \bar{H}_0^2}{\bar{\rho} \bar{u}_r^2}, M_{nF_p} = \frac{\bar{\mu}_0 \chi_2 \bar{H}_0^2}{\bar{\rho}_{mp} \bar{u}_{r1}^2}, M_{nM} = \frac{\bar{\mu}_0^2 \bar{H}_0^2 \bar{h}^2 \bar{\sigma}}{\bar{\mu}}, M_{nM_p} = \frac{\bar{\mu}_0^2 \bar{H}_0^2 \bar{d}^2 \bar{\sigma}_p}{\bar{\mu}},$$

$$Pe = \frac{\bar{h} \bar{u}_r}{D_{Total}}, d_o = \frac{\bar{d}_{mp}}{\bar{h}}, D_p = \frac{\bar{\rho}_{mp}}{\bar{\rho}}, S_o = \frac{\bar{h}^2 \varphi_p}{D_{Total}}.$$

where  $M_{nF}$  and  $M_{nF_p}$ , and  $M_{nM}$  and  $M_{nM_p}$  are the magnetic number (FHD and MHD) of the blood and drug-loaded MN, respectively.  $d_o, D_p$  are the ratios of the size, and density of the drug-loaded MN to the channel height, and density of the blood, respectively.  $Pe$  is the Peclet number, and  $S_o$  source constant respectively.

#### 4.6 Numerical Method

The continuity Equations (4.26)–(4.27) of the flow are transformed to stream functions similar to the previous Chapter 3 by substituting Equation (3.23) into Equations (4.26)–(4.30). Following the procedures in the previous Chapter 3, the equations for the stream functions of the blood and the MN flow (4.26)–(4.30) are approximated by the standard finite-difference equations and solved by the block Gauss-Seidel method (M. Cervera et al., 1996). This is followed by the successive over-relaxation (SOR) as follows.  $\psi_{new}^{k+1} = \psi_{GS}^{k+1} \theta + (1 - \theta) \psi^k$ , where  $\psi_{GS}^{k+1}$  is the numerical solution obtained by the block Gauss-Seidel method,  $\psi^k$  is the solution at the previous iteration step  $k$ , and  $\theta$  is the relaxation parameter. Note that Equations (34)–(35) depend implicitly on time due to  $u, u_p$  at the right-hand sides. Hence, the equations must be solved at every time step. The functions  $u, u_p$  are taken from the  $n$ -th time step. The numerical solution of Equations (4.28b)–(4.30b) is based on a similar procedure including the block Gauss-Seidel and the SOR. Writing (4.28a)–(4.30a) in the standard form yields:

$$\frac{\partial u}{\partial t} = A_1 \frac{\partial^2 u}{\partial x^2} + B_1 \frac{\partial^2 u}{\partial y^2} + C_1 \frac{\partial u}{\partial x} + D_1 \frac{\partial u}{\partial y} + E_1 u + F_1, \quad (4.28c)$$

$$\frac{\partial v}{\partial t} = A_2 \frac{\partial^2 v}{\partial x^2} + B_2 \frac{\partial^2 v}{\partial y^2} + C_2 \frac{\partial v}{\partial x} + D_2 \frac{\partial v}{\partial y} + E_2 v + F_2, \quad (4.28d)$$

$$\frac{\partial u_p}{\partial t} = C_3 \frac{\partial u_p}{\partial x} + D_3 \frac{\partial u_p}{\partial y} + E_3 u + F_3, \quad (4.29c)$$

$$\frac{\partial v_p}{\partial t} = C_4 \frac{\partial v_p}{\partial x} + D_4 \frac{\partial v_p}{\partial y} + E_4 v + F_4, \quad (4.29d)$$

$$\frac{\partial C_M}{\partial t} = A_5 \frac{\partial^2 C_M}{\partial x^2} + B_5 \frac{\partial^2 C_M}{\partial y^2} + C_5 \frac{\partial C_M}{\partial x} + D_5 \frac{\partial C_M}{\partial y} + E_5 C_M + F_5, \quad (4.30a)$$

$$\frac{\partial C_{MM}}{\partial t} = A_6 \frac{\partial^2 C_{MM}}{\partial x^2} + B_6 \frac{\partial^2 C_{MM}}{\partial y^2} + C_6 \frac{\partial C_{MM}}{\partial x} + D_6 \frac{\partial C_{MM}}{\partial y} + E_6 C_{MM} + F_6, \quad (4.31b)$$

$$\frac{\partial C_{MT}}{\partial t} = A_7 \frac{\partial^2 C_{MT}}{\partial x^2} + B_7 \frac{\partial^2 C_{MT}}{\partial y^2} + C_7 \frac{\partial C_{MT}}{\partial x} + D_7 \frac{\partial C_{MT}}{\partial y} + E_7 C_{MT} + F_7, \quad (4.31c)$$

where coefficients  $A_i, B_i, C_i, D_i$  and the right-hand-side  $F_i$  in each equation depend on the other unknowns and their partial derivatives. As in the previous Chapter 3, we apply the standard second-order finite-difference approximation to the second derivatives and the upwind first-order approximation to the first derivatives. For instance, (4.28b) is approximated as follows

$$\begin{aligned} \frac{u_{i,j}^{n+1} - u_{i,j}^n}{\tau} = & A_{1,i,j}^n \frac{u_{i+1,j}^{n+1} - 2u_{i,j}^{n+1} + u_{i-1,j}^{n+1}}{\Delta x^2} + B_{1,i,j}^n \frac{u_{i,j+1}^n - 2u_{i,j}^{n+1} + u_{i,j-1}^{n+1}}{\Delta y^2} \\ & + C_{1,i,j}^n \frac{u_{i+1,j}^{n+1} - u_{i,j}^{n+1}}{\Delta x} + C_{1,i,j}^m \frac{u_{i,j}^{n+1} - u_{i-1,j}^{n+1}}{\Delta x} + D_{1,i,j}^m \frac{u_{i,j+1}^n - u_{i,j}^n}{\Delta y} + \\ & D_{1,i,j}^n \frac{u_{i,j}^{n+1} - u_{i,j-1}^{n+1}}{\Delta y} + E_{1,i,j} u_{i,j}^{n+1} + F(H_{i,j}^n, \psi^{n+1}, \psi_p^{n+1}), \end{aligned} \quad (4.28e)$$

where  $u_{i,j}^n = u_{i,j}(x_i, y_j, n\tau)$ . Similar as previous Chapter 3,  $\tau$  is the time step,  $\Delta x = \frac{1}{N}$ ,  $\Delta y = \frac{1}{M}$  are the spatial steps,  $x_i = i\Delta x$ ,  $y_j = j\Delta y$ ,  $i = \overline{1, N-1}$ ,  $j = \overline{1, M-1}$ ,  $N$  is the number of points in the  $x$  direction,  $M$  is the number of points in the  $y$  direction,  $C' = \frac{C+|C|}{2}$ ,  $C'' = \frac{C-|C|}{2}$ ,  $D' = \frac{D+|D|}{2}$ ,  $D'' = \frac{D-|D|}{2}$ .

The iterative algorithm is used to solve the system of Equations (4.28b)-(4.30b) using the steps outlined in the previous Chapter 3. The convergence is established when:

$$\Delta = \max_{i,j,U} |U^{l+1} - U^l| < \varepsilon,$$

#### 4.7 Results and Discussion

The magnetic numbers for blood and drug-loaded MN are given by:

$$M_{nF} = \frac{\bar{h}^2 \bar{\rho} \bar{\mu}_0 \chi_1 \bar{H}_0^2}{\bar{\mu}^2 \text{Re}^2} \Rightarrow \frac{\bar{h}^2 \bar{\rho} \bar{B}^2 \chi_1}{\bar{\mu}_0 \bar{\mu}^2 \text{Re}^2}, M_{nFp} = \frac{d_{mp}^2 \bar{\rho}^2 \bar{\mu}_0 \chi_2 \bar{H}_0^2}{\bar{\mu}^2 \bar{\rho}_{mp} \text{Re}_p^2} \Rightarrow \frac{d_{mp}^2 \bar{\rho}^2 \chi_2 \bar{B}^2}{\bar{\mu}^2 \bar{\mu}_0 \bar{\rho}_{mp} \text{Re}_p^2}, \quad (4.32)$$

$$M_{nM} = \frac{\bar{h}^2 \bar{\sigma} \bar{\mu}_0^2 \bar{H}_0^2}{\bar{\mu}} \Rightarrow \frac{\bar{h}^2 \bar{\sigma} \bar{B}_0^2}{\bar{\mu}}, M_{nMp} = \frac{d_{mp}^2 \bar{\sigma}_p \bar{\mu}_0^2 \bar{H}_0^2}{\bar{\mu}} \Rightarrow \frac{d_{mp}^2 \bar{\sigma}_p \bar{B}^2}{\bar{\mu}}, \quad (4.33)$$

In this work, we consider the Newtonian nature of blood. Thus, our data fit on aorta, arteries, veins and vena cava. The actual velocities and its nature in different blood vessels are mentioned in **Table 1.1**.

##### 4.7.1 Impact of the Magnetic Field Intensity (FHD and MHD):

In order to evaluate the impact of MF, consider  $(a,b)=(10, 10)$ ,  $\bar{u}_\eta = 3.8$ ,  $C_v = 0.004$ ,  $\text{Re}_p \approx 3.6 \times 10^{-2}$ ,  $\text{Re} = 25$ , and  $\text{St} \approx 2.47 \times 10^{-4}$ . Consider 5 cases.

Case 1: For FHD,  $B = 8$ ,  $M_{nF} = 52500$ ,  $M_{nF_p} \approx 265287$ ,  $M_{nM} = 0$ ,  $M_{nM_p} \approx 0$ .

Case 2: For MHD,  $B = 2$ ,  $M_{nF} = 0$ ,  $M_{nF_p} \approx 0$ ,  $M_{nM} = 4.0 \times 10^{-3}$ ,  $M_{nM_p} \approx 1.42 \times 10^{-9}$ .

Case 3: For FHD and MHD,  $B = 2$ ,  $M_{nF} = 13125$ ,  $M_{nF_p} \approx 165804$ ,  $M_{nM} = 4.0 \times 10^{-3}$ ,  $M_{nM_p} \approx 1.42 \times 10^{-9}$ .

Case 4: For FHD and MHD,  $B = 5$ ,  $M_{nF} = 32812$ ,  $M_{nF_p} \approx 221000$ ,  $M_{nM} = 2.5 \times 10^{-2}$ ,  $M_{nM_p} \approx 8.9 \times 10^{-9}$ .

Case 5: For FHD and MHD,  $B = 8$ ,  $M_{nF} = 52500$ ,  $M_{nF_p} \approx 265287$ ,  $M_{nM} = 6.4 \times 10^{-2}$ ,  $M_{nM_p} \approx 2.2 \times 10^{-8}$ .

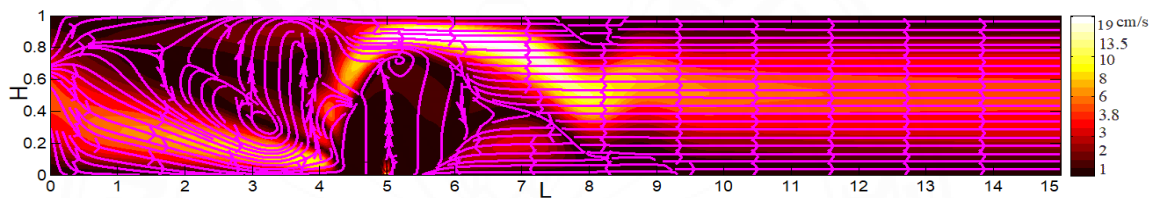
The magnet wire is 10 cm below the wall in a vertical position. **Figure 4.3-4.4** depicts the pattern of the blood and drug-loaded MN flows. For same magnetic field strength, we compare case 1 for FHD flows (**Figure 4.3a**) with case 5 for combined effects of FHD and MHD flows (**Figure 4.3e**) and found that the additional Lorentz force (MHD) reduces blood flow and suppresses the large vortices created by FHD flows. As a result, the total number of vortices produced by the combined effects of FHD and MHD flows is the same (see cases 3 to 5 in **Figures 4.3c-e**).

Conversely, when the magnetic field strength increases, the number of vortices increases (case 1 in **Figure 4.3a**).

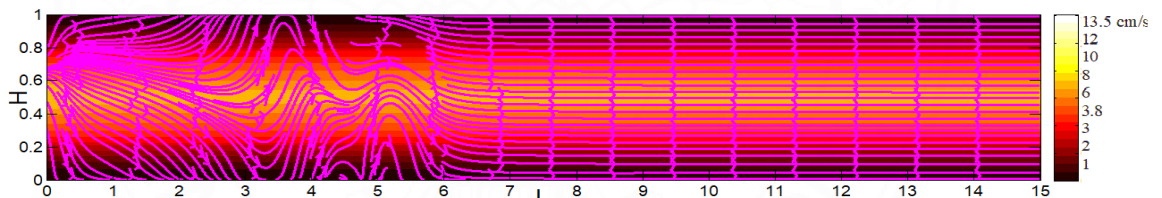
Furthermore, we investigated case 2 for MHD flow. Clearly, there is a disturbance near the magnetic source (**Figure 4.3b**). Nevertheless, when the magnetic field gradient is strong and non-uniform, FHD effects are important, whereas MHD effects are dominant when the magnetic field gradient is uniform. Magnetization has no impact on blood when it is exposed to a uniform magnetic field and  $M_{nF} = 0$ ,  $M_{nF_p} \approx 0$ . Nevertheless, the MN increases the magnetic susceptibility of blood by several orders, making magnetic forces (FHD) more powerful (see **Figures 3.3-3.6**).

**Figure 4.4** shows how the MF works against the DF. MN flow is affected in the same way that blood flow is affected by FHD and MHD (**Figures 4.4a-e**). However, it is characterized by two large vortices. We also examined case 2 for MHD flow and noticed that the flow is not significantly affected, although there is a minor disturbance. Due to the small particle sizes, the magnetic number ( $M_{nm,p}$ ) for MN flow is relatively low. MN, on the other hand, has a higher electrical conductivity than blood (**Figure 4.4b**).

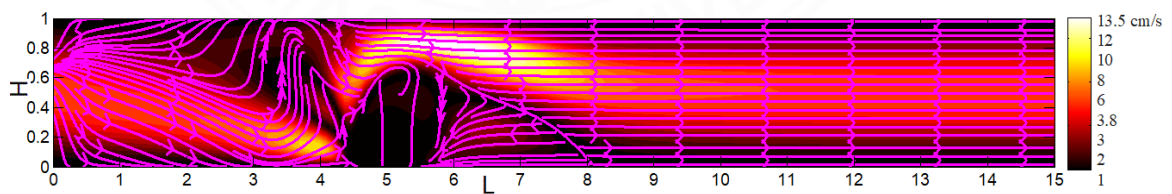
The abovementioned results presented in Figs. 6 and 7 coincide with results concerning the effect of MHD and FHD forces presented in the studies (Tzirtzilakis, 2005; Xenos & Tzirtzilakis, 2013; Raptis, 2014).



a)

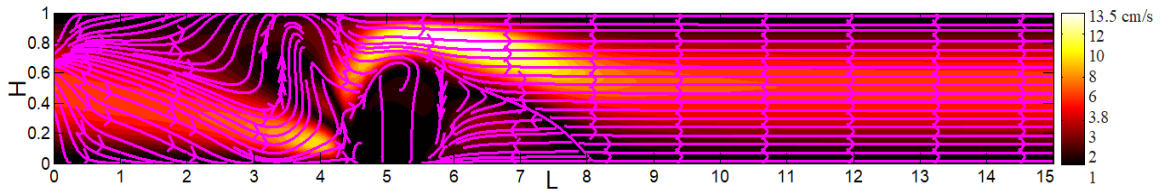


b)

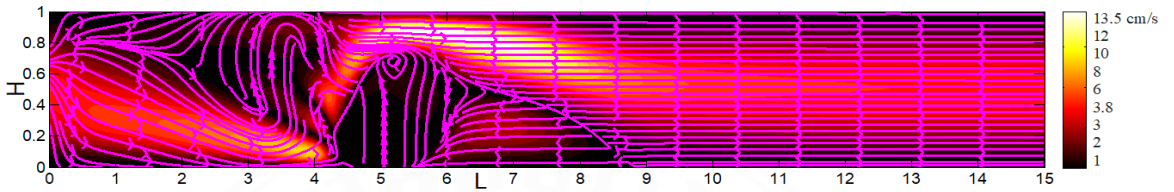


c)



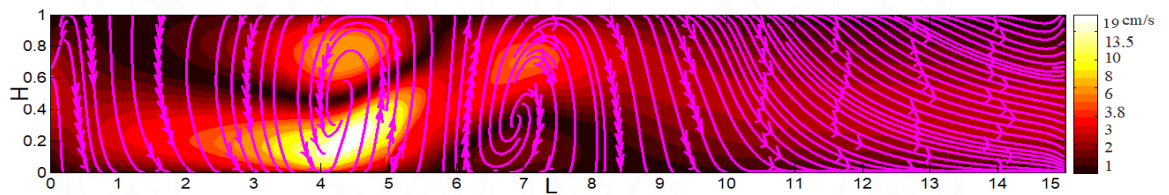


d)

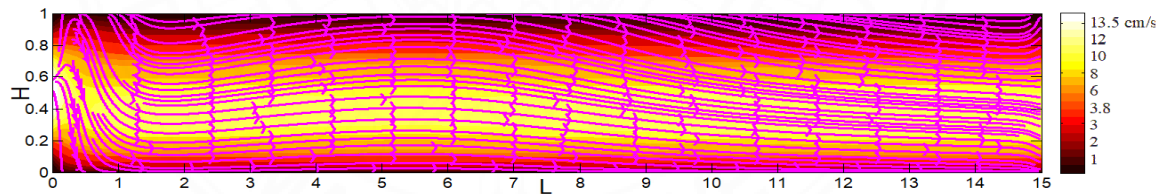


e)

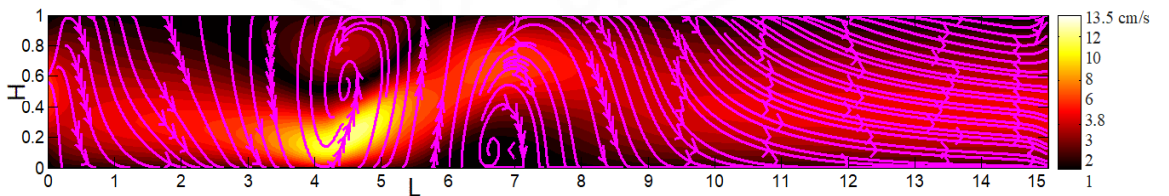
**Figure 4.3** Streamlines of the blood flow: a) FHD, b) MHD, c)  $B=2$ , d)  $B=5$ , e)  $B=8$ .



a)



b)



c)

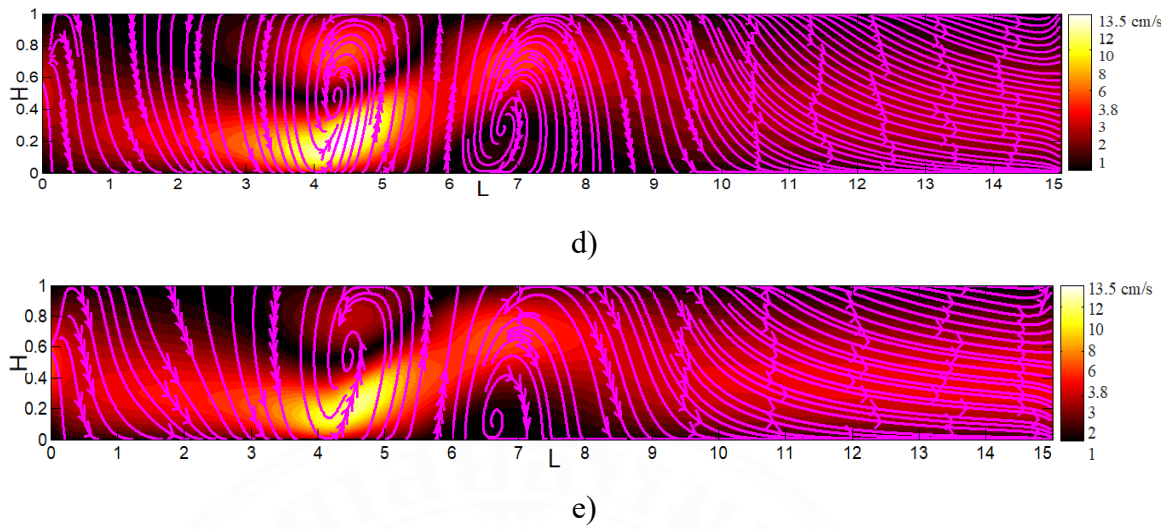


**Figure 4.4** Streamlines of the MN flow: a) FHD, b) MHD, c)  $B=2$ , d)  $B=5$ , e)  $B=8$ .

#### 4.7.2 Impact of MN (therapeutic drug-loaded and MN) on Blood Flow:

Consider  $(a,b)=(10, 10)$ ,  $\bar{u}_f = 3.8$ ,  $C_v = 0.004$ ,  $B=5$ ,  $f=1$ , and  $Re \approx 250$ .

Consider 5 cases.

Case 1:  $\bar{d}_{mp} = 250$ ,  $f_1 = 0$ ,  $\bar{\rho}_p = 5200$ ,  $St \approx 3.5 \times 10^{-4}$ ,  $Re_p \approx 8.2 \times 10^{-4}$ ,  $M_{nF_p} \approx 98153$ ,  
 $M_{nM_p} \approx 6.2 \times 10^{-9}$ .

Case 2:  $\bar{d}_{mp} = 300$ ,  $f_1 = 30\%$ ,  $\bar{\rho}_p \approx 3015.6$ ,  $St \approx 2.47 \times 10^{-4}$ ,  $Re_p \approx 9.8 \times 10^{-4}$ ,  
 $M_{nF_p} \approx 165804$ ,  $M_{nM_p} \approx 8.9 \times 10^{-9}$ .

Case 3:  $\bar{d}_{mp} = 400$ ,  $f_1 = 40\%$ ,  $\bar{\rho}_p \approx 1343.8$ ,  $St \approx 1.47 \times 10^{-4}$ ,  $Re_p \approx 1.3 \times 10^{-3}$ ,  
 $M_{nF_p} \approx 372079$ ,  $M_{nM_p} \approx 1.5 \times 10^{-8}$ .

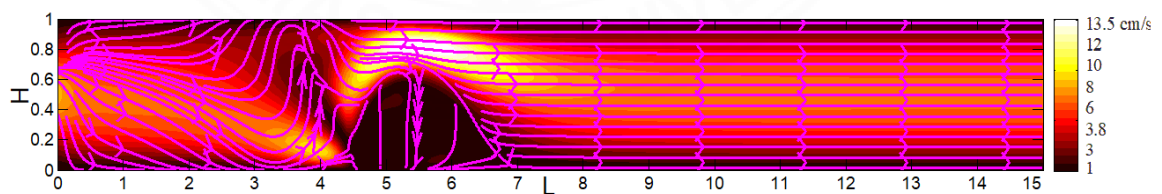
Case 4:  $\bar{d}_{mp} = 500$ ,  $f_1 = 50\%$ ,  $\bar{\rho}_p \approx 829.8$ ,  $St \approx 1.13 \times 10^{-4}$ ,  $Re_p \approx 1.64 \times 10^{-3}$ ,  
 $M_{nF_p} \approx 602700$ ,  $M_{nM_p} \approx 2.4 \times 10^{-8}$ .

Case 5 :  $\bar{d}_{mp} = 20,000$ ,  $f_1 = 50\%$ ,  $\bar{\rho}_p \approx 1594$ ,  $St \approx 1.23 \times 10^{-2}$ ,  $Re_p \approx 6.5 \times 10^{-2}$ ,  
 $M_{nF_p} \approx 602700$ ,  $M_{nM_p} \approx 3.9 \times 10^{-5}$ .

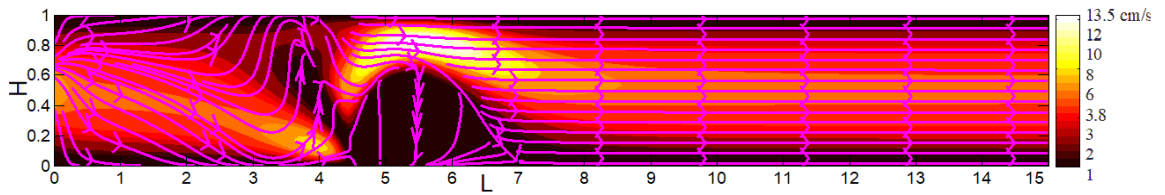
The magnetic numbers  $M_{nF} \approx 32812$ ,  $M_{nM} = 2.5 \times 10^{-2}$ . The streamlines of the blood flow for Cases 1, 2, 3, 4 and 5 are shown in **Figure 4.5**. Clearly, the drug-loaded MN concentration has a major impact on blood flow. The circulation is characterized by a strong vortex and backflow. As we increase the drug concentration from 30% to 50%, the size of the vortices increases. For  $d=250$  nm, the change is insignificant (Case 2 to 4 in **Figure 4.5b-d**). However, when we increased the size of MN (20,000) while keeping the drug concentration at 50%, the TMDD zone grew significantly (Case 5 in **Figure 4.5e**).

On the other hand, the velocities of blood and drug-loaded MN flow vary throughout the TMDD zone. This is because the density of MN varies substantially, this affects the  $St$ ,  $Re_p$ , and magnetic numbers. Two well-defined vortices are depicted in **Figure 4.6a-e** for cases 1 to 5.

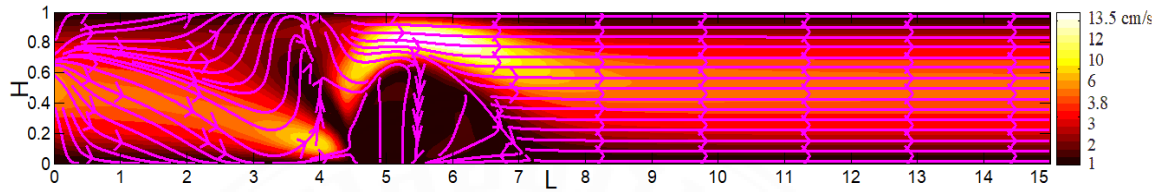
It is worth noting that drug concentrations are essential in cancer treatment because these medications also harm healthy cells. Widder et al. (1981) reported that high dosages of doxorubicin (0.5-5 mg/kg) have a negative effect on the animal and with an average weight loss of 12 g in animals given large doses of doxorubicin, indicating that the medicine causes systemic toxicity. The weights of animals given low dosages of doxorubicin medicines, on the other hand, increased by 23.3 g and 17.8 g.



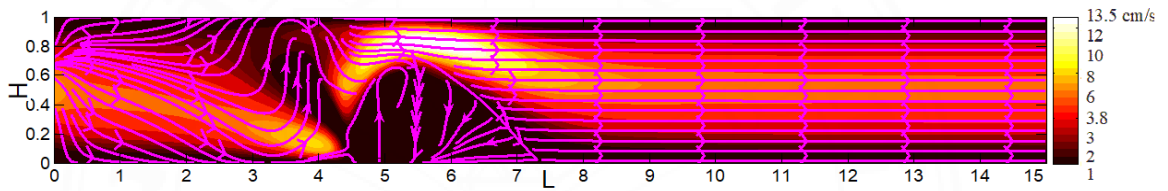
a)



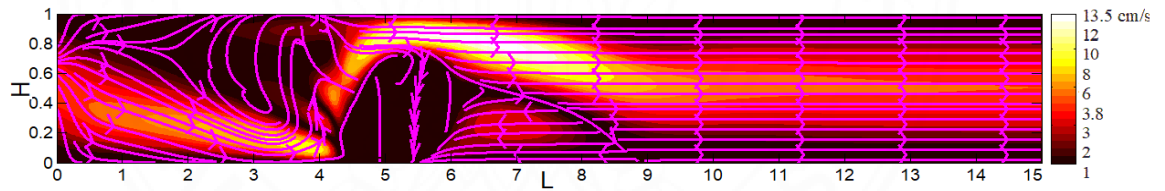
b)



c)



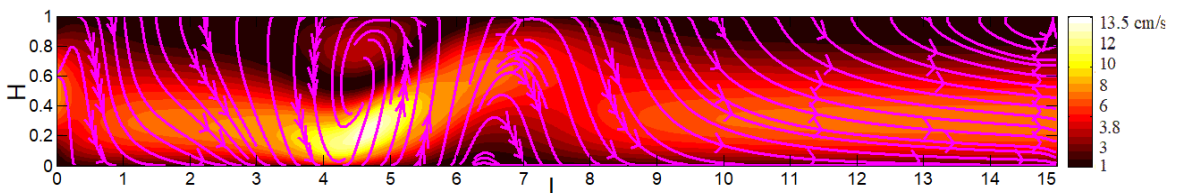
d)



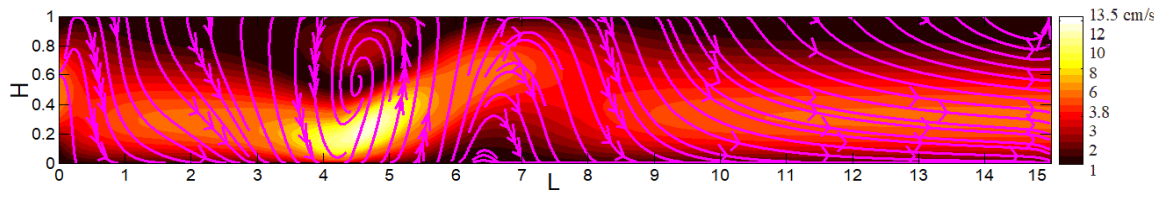
e)

**Figure 4.5** Streamlines of the blood for different sizes of the MN:

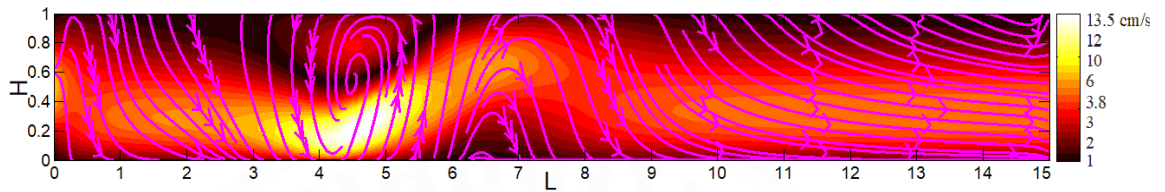
a)  $\bar{\rho}_p = 5200$ , b)  $\bar{\rho}_p \approx 3015.6$ , c)  $\bar{\rho}_p \approx 1343.8$ , d)  $\bar{\rho}_p \approx 829.8$ ,  $\bar{\rho}_p \approx 1594$ ,  $t_s \approx 1.0$ .



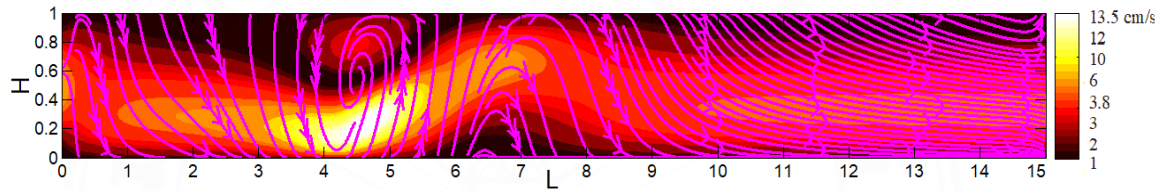
a)



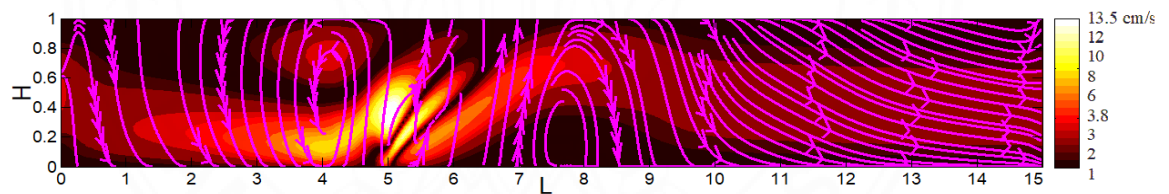
b)



c)



d)



e)

**Figure 4.6** Streamlines of the MN for different sizes of MN:

a)  $\bar{\rho}_p = 5200$ , b)  $\bar{\rho}_p \approx 3015.6$ , c)  $\bar{\rho}_p \approx 1343.8$ , d)  $\bar{\rho}_p \approx 829.8$ ,  $\bar{\rho}_p \approx 1594$ .

### 4.7.3 The Concentration of MN (therapeutic drug-loaded) in Normal and Tumor Cells:

In a straight idealized blood artery with endothelial membrane surrounded by tissue, MN is subjected to diffusion, blood convection, MFs and a source, we consider four conditions where  $(a,b)=(10, 10)$ ,  $\bar{u}_r = 3.8$ ,  $\bar{d}_{mp} = 300$ ,  $f_1 = 30\%$ ,  $\bar{\rho}_p \approx 3015.6$ ,  $C_v = 0.04$ ,  $St \approx 2.47 \times 10^{-4}$ ,  $B = 5$ ,  $f = 1$ , and  $Re \approx 250$ .

Case 1: The concentration of drug-loaded MN in normal blood arteries is considered in this situation. As a result, the diameters of the pores in the endothelium membrane are smaller than those of MN. Hence,  $D_M \approx D_T \approx 0$  and the MN remains inside the blood vessels (see **Figure 4.7**). The magnetic field intensity and magnetic numbers are  $B = 2$ ,  $M_{nF} = 13125$ ,  $M_{nFp} \approx 165804$ .

Case 2: The concentration of drug-loaded MN inside leaky blood arteries is examined when the MF is zero. Clearly, the MN is leaving the vessel through endothelial pores when  $D_M$  and  $D_T$  are greater than zero. However, the concentration remains inside the endothelium membrane, preventing it from reaching tumorous tissue via diffusion alone.

Nevertheless, the external MFs are required to drag the particles towards the tumorous tissue in order to enhance the concentration of MN. For this purpose, we discussed two more cases: Case 3: MN begins to flow towards the magnet when the external MF is applied. For this case,  $B=2$ ,  $M_{nF}=13125$ ,  $M_{nFp}=165804$ .

Case 4: Further increasing the MF increases the concentration of MN towards tumorous tissue. The magnetic field and magnetic numbers are  $B=5$ ,  $M_{nF}=32812$ ,  $M_{nFp}=221000$ .

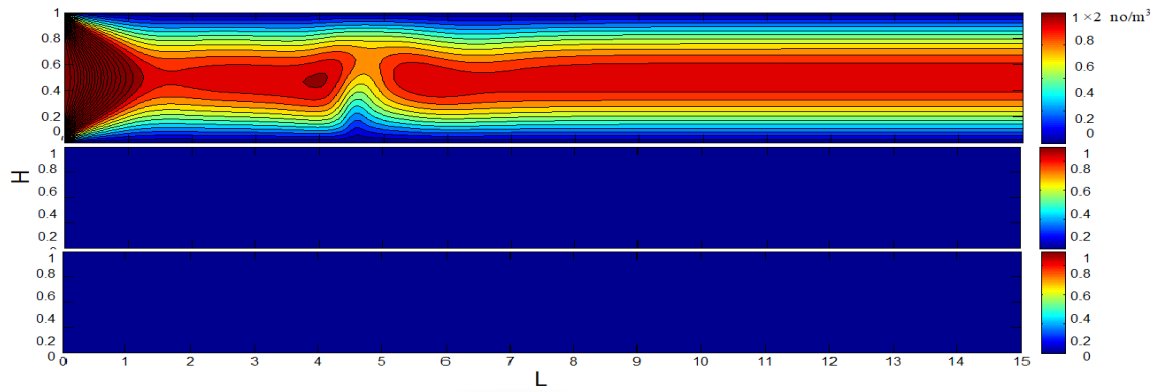


**Figure 4.7** Concentration of drug-loaded MN in normal blood vessel, endothelial cell and tissue:  $B = 2$ ,  $b = 10\text{cm}$ ,  $M_{nF} = 13125$ ,  $M_{nF_p} \approx 165804$ .

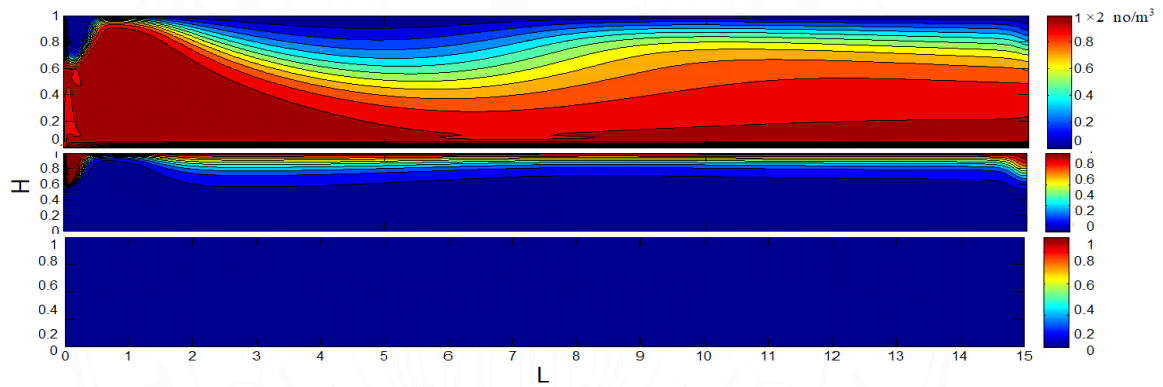


**Figure 4.8** Concentration of drug-loaded MN in leaky blood vessel, endothelial cell and tissue (tumorous cells):  $B = 0$ .

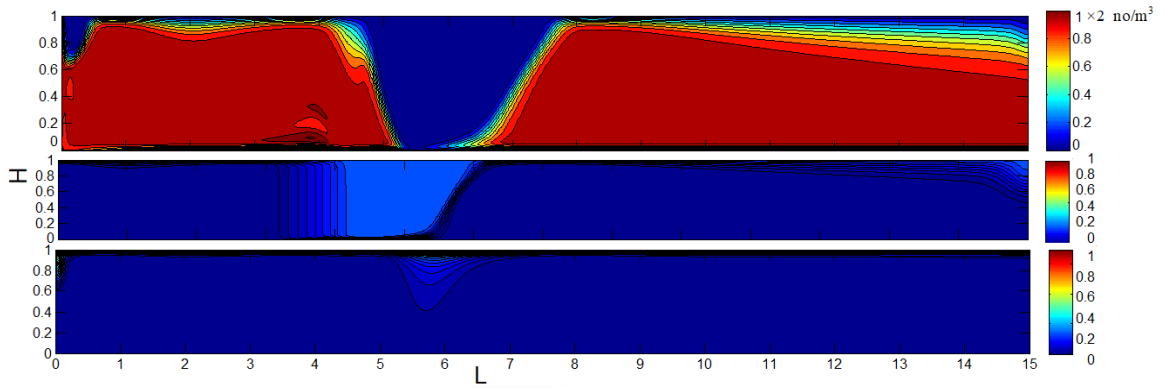


**Figure 4.9** Concentration of drug-loaded MN in leaky blood vessel, endothelial cell and tissue (tumorous cells):  $B = 2$ ,  $b = 10$ cm,  $M_{nF} = 13125$ ,  $M_{nF_p} \approx 165804$ .

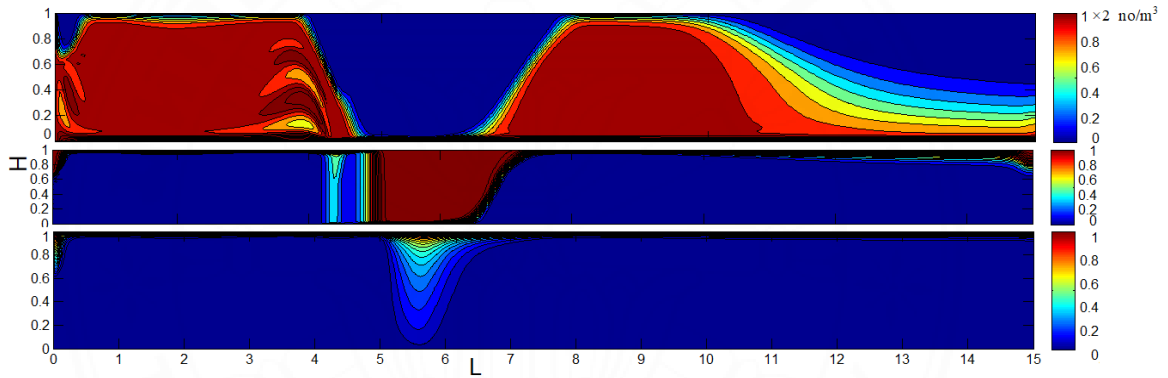


**Figure 4.10** Concentration of drug-loaded MN in leaky blood vessel, endothelial cell and tissue (tumorous cells):  $B = 5$ ,  $b = 10$ cm,  $M_{nF} = 32812$ ,  $M_{nF_p} \approx 221000$ .



## **CHAPTER 5**

### **ENTROPY GENERATION IN A MIXED CONVECTION POISEUILLE FLOW OF MOLYBDENUM DISULPHIDE JEFFREY NANOFUID**

#### **5.1 Introduction**

In this chapter, entropy analysis in a mixed convection Poiseuille flow of a Molybdenum Disulphide Jeffrey Nanofluid (MDJN) is presented. The problem is formulated in terms of a boundary value problem for a system of partial differential equations. An analytical solution for the velocity and the temperature is obtained using the perturbation technique. Entropy generation has been derived as a function of the velocity and temperature gradients. The solutions are displayed graphically and the relevant importance of the input parameters is discussed. A Jeffrey nanofluid (JN) has been compared with a Second Grade Nanofluid (SGN) and Newtonian Nanofluid (NN).

#### **5.2 Mathematical Formulation**

The mathematical formulation for the non-Newtonian single phase JN model is considered (the velocity of the nanoparticles and the base fluid is the same) which consists of the following components.

##### **5.2.1 Governing Equations**

Consider entropy generation in a mixed convection Poiseuille flow of a  $\text{MoS}_2$ -water JN. The flow is due to the buoyancy force and the external pressure gradient (oscillatory type). Properties of the specific nanofluid are taken from experimental works (see the Introduction). The temperature is assumed constant at the boundary walls. The  $x$  – axis is considered parallel to the flow, and the  $y$  – axis is normal to the flow. Further, it is assumed

that the thermophysical properties of the nanofluid are constant, except the density variation (Boussinesq approximation, Tiwari & Das, 2007). The governing equations of an unsteady, one-dimensional, unidirectional non-Newtonian MDJN flow are given by

$$\bar{\rho}_{nf} \frac{\partial \bar{u}}{\partial t} = -\nabla p + \frac{\bar{\mu}_{nf}}{(1+\lambda_1)} \left(1 + \lambda_2 \frac{\partial}{\partial t}\right) \nabla^2 \mathbf{V} + (\bar{\rho}\bar{\beta})_{nf} g (\bar{T} - T_0), \quad (5.1)$$

$$(\bar{\rho}\bar{c})_{nf} \frac{\partial \bar{T}}{\partial t} = \bar{k}_{nf} \nabla^2 T + 4\alpha_0^2 (\bar{T} - T_0), \quad (5.2)$$

where  $\bar{u}(y,t)$  is the velocity of the nanofluid,  $\bar{T}(y,t)$  the temperature,  $\bar{\rho}_{nf}$  the density,  $\bar{\mu}_{nf}$  the dynamic viscosity,  $\lambda_1$  the relaxation to retardation time parameter,  $\lambda_2$  the retardation parameter,  $(\bar{\rho}\bar{\beta})_{nf}$  the thermal expansion coefficient,  $g$  the acceleration of gravity,  $(\bar{\rho}\bar{c})_{nf}$  the heat capacitance,  $\bar{k}_{nf}$ , the thermal conductivity, and  $\alpha_0$  the mean radiation absorption coefficient.

### 5.3 Thermo physical Properties of Nanofluids

Further, we assume spherical nanoparticles characterized by (Das & Jana, 2015; Aaiza et al., 2015a; Aaiza et al., 2015b):

$$\begin{aligned} \bar{\rho}_{nf} &= \bar{\rho}(1-\phi) + \phi\bar{\rho}_p, \quad (\bar{\rho}\bar{\beta})_{nf} = \bar{\rho}\bar{\beta}(1-\phi) + \phi(\bar{\beta}\rho)_p, \\ (\bar{\rho}\bar{c})_{nf} &= \bar{\rho}\bar{c}(1-\phi) + \phi\bar{\rho}_p\bar{c}_p, \end{aligned} \quad (5.3)$$

$$\bar{\mu}_{nf} = \frac{\bar{\mu}}{(1-\phi)^{2.5}}, \quad \bar{k}_{nf} = \bar{k} \frac{(\bar{k}_p + 2\bar{k}) - 2\phi(\bar{k} - \bar{k}_p)}{(\bar{k}_p + 2\bar{k}) + \phi(\bar{k} - \bar{k}_p)},$$

where  $\phi$  specifies the volume fraction of the nanoparticles.

The properties of the base fluid and the nanoparticles are presented in **Table 5.1** (Das &

Jana, 2015; McBride et al., 1976; Liu et al., 2014; Ding et al., 2015; Benavente et al., 2004).

**Table 5.1** Thermophysical properties of water and nanoparticles.

Model	$\bar{\rho}$	$\bar{c}$	$\bar{k}$	$\beta_1 \times 10^{-5}$
H <sub>2</sub> O	997.1	4179	0.613	21
MoS <sub>2</sub>	$5.06 \times 10^3$	397.21	85-110	2.8424

#### 5.4 Dimensionless Equations

Some of the dimensionless parameters are same as Chapter 3, while, the others dimensionless variables are as follows:

$$x^* = \frac{\bar{x}}{\bar{h}}, \quad y^* = \frac{\bar{y}}{\bar{h}}, \quad t^* = \frac{\bar{t}\bar{u}_r}{\bar{h}}, \quad p^* = \frac{\bar{h}}{\bar{\mu}\bar{u}_r}, \quad T^* = \frac{\bar{T} - T_0}{T_w - T_0}. \quad (5.4)$$

Substituting into Equations (5.1) and (5.2) and omitting the superscript \* (non-dimensionalization) yields

$$\phi_1 \text{Re} \frac{\partial u}{\partial t} = -\frac{\partial p}{\partial x} + \frac{\phi_2}{1 + \lambda_1} \frac{\partial^2 u}{\partial y^2} + \lambda \frac{\phi_2}{1 + \lambda_1} \frac{\partial^3 u}{\partial t \partial y^2} + \text{Gr} \phi_3 T, \quad (5.5)$$

$$\frac{\phi_4 \text{Pe}}{\lambda_n} \frac{\partial T}{\partial t} = \frac{\partial^2 T}{\partial y^2} + \frac{N^2}{\lambda_n} T, \quad (5.6)$$

where

$$\phi_1 = (1-\phi) + \phi \frac{\bar{\rho}_p}{\bar{\rho}}, \quad \phi_2 = \frac{1}{(1-\phi)^{2.5}}, \quad \lambda = \frac{\lambda_2 \bar{u}_r}{\bar{h}}, \quad \phi_3 = (1-\phi) + \phi \frac{(\bar{\rho}\bar{\beta})_p}{(\bar{\rho}\bar{\beta})},$$

$$\text{Gr} = \frac{(\bar{\rho}\bar{\beta}_1) g \bar{h}^2 (T_w - T_0)}{\bar{u}_r \bar{\mu}}, \quad \text{Pe} = \frac{(\bar{\rho}\bar{c})_p u_r \bar{h}}{\bar{k}}, \quad \phi_4 = \left[ (1-\phi) + \phi \frac{(\bar{\rho}\bar{c})_p}{(\bar{\rho}\bar{c})} \right],$$

$$\lambda_n = \frac{\bar{k}_{nf}}{\bar{k}} = \frac{(\bar{k}_p + 2\bar{k}) - 2\phi(\bar{k} - \bar{k}_p)}{(\bar{k}_p + 2\bar{k}) + \phi(\bar{k} - \bar{k}_p)}, \quad N^2 = \frac{4\bar{h}^2 \alpha_0^2}{\bar{k}}.$$

$\lambda$ , Gr, Pe and  $N$  denote the Jeffery parameter, thermal Grashof number, Peclet number, and the radiation parameter respectively.

After some algebraic manipulations, Equations (5.5) and (5.6) become:

$$a_0 \frac{\partial u}{\partial t} = -\frac{\partial p}{\partial x} + \alpha_1 \frac{\partial^2 u}{\partial y^2} + \alpha_2 \frac{\partial^3 u}{\partial t \partial y^2} + a_1 T, \quad (5.7)$$

$$b_0^2 \frac{\partial T}{\partial t} = \frac{\partial^2 T}{\partial y^2} + b_1^2 T, \quad (5.8)$$

where

$$a_0 = \phi_1 \text{Re}, \quad \alpha_1 = \frac{\phi_2}{1 + \lambda_1}, \quad \alpha_2 = \alpha_1 \lambda, \quad a_1 = \phi_3 \text{Gr}, \quad b_0^2 = \frac{\text{Pe} \phi_4}{\lambda_n}, \quad b_1^2 = \frac{N^2}{\lambda_n},$$

## 5.5 Boundary Conditions

The boundary conditions at  $y=0$  and  $y=\bar{h}$  are:

$$\bar{u}(0, \bar{t}) = 0, \quad \bar{u}(\bar{h}, \bar{t}) = 0, \quad (5.9)$$

$$\bar{T}(0, \bar{t}) = T_0, \bar{T}(\bar{h}, \bar{t}) = T_w. \quad (5.10)$$

where  $T_0$ ,  $T_w$  is temperature at the lower and upper wall of the channel.

Non-dimensionalization of the boundary conditions yields:

$$u(0, t) = 0, u(1, t) = 0, t > 0, \quad (5.11)$$

$$T(0, t) = 0, T(1, t) = 1, t > 0, \quad (5.12)$$

## 5.6 Mathematical Solution

In order to solve the boundary value problem (5.7)-(5.8), (5.11)-(5.12) by perturbation techniques, the unknowns are represented by (Ali et al., 2012):

$$u(y, t) = u_0(y) + \varepsilon \exp(i\omega t) u_1(y), \quad (5.13)$$

$$T(y, t) = T_0(y) + \varepsilon \exp(i\omega t) T_1(y). \quad (5.14)$$

where  $u_0(y)$ ,  $u_1(y)$ , are the perturb velocities,  $T_0(y)$ ,  $T_1(y)$ , are the perturb temperatures, and  $\varepsilon$ ,  $\omega$ , are the perturb parameter and the frequency of oscillation, respectively.

The external pressure is represented using the same approach:

$$-\frac{\partial p}{\partial x} = \lambda_0 + \varepsilon \exp(i\omega t) \bar{\lambda}_1,$$

where  $\lambda_0$ ,  $\bar{\lambda}_1$  are the perturb pressure gradients.

Substituting Equations (5.13) and (5.14) into Equations (5.7) and (5.8) yields the following system of ordinary differential equations:

$$\frac{d^2 u_0}{dy^2} = -\frac{\lambda_0}{\alpha_2} - m_1^2 T_0, \quad (5.15)$$

$$\frac{d^2 u_1}{dy^2} - m_2^2 u_1 = -\bar{\lambda}_1 m_3, \quad (5.16)$$

$$\frac{d^2 T_0}{dy^2} + b_1^2 T_0 = 0, \quad (5.17)$$

$$\frac{d^2 T_1}{dy^2} + m_0^2 T_1, \quad (5.18)$$

where

$$m_1 = \sqrt{\frac{\alpha_1}{\alpha_1}}, m_2 = \sqrt{\frac{a_0 i \omega}{\alpha_1 + i \omega \alpha_2}}, m_3 = \frac{1}{\alpha_1 + i \omega \alpha_2}, m_0 = \sqrt{b_1^2 - i \omega b_0^2}.$$

The corresponding boundary conditions are:

$$u_0(0) = 0, u_0(1) = 0, \quad (5.19)$$

$$u_1(0) = 0, u_1(1) = 0, \quad (5.20)$$

$$T_0(0) = 0, T_0(1) = 1, \quad (5.21)$$

$$T_1(0) = 0, T_1(1) = 0. \quad (5.22)$$

Solving Equations (5.17) and (5.18) with the boundary conditions (5.21) and (5.22) yields:

$$T_0 = \frac{\sin(b_1 y)}{\sin(b_1)}, T_1 = 0. \quad (5.23)$$

Taking into account Equation (13) reveals that:

$$T(y,t) = \frac{\sin(b_1 y)}{\sin(b_1)}. \quad (5.24)$$

Equations (5.15) and (5.16) with the boundary conditions (5.19) and (5.20) yield that:

$$u_0 = -\frac{\lambda_0 y^2}{2\alpha_2} + \frac{m_1^2}{b_1^2} \frac{\sin(b_1 y)}{\sin(b_1)} + c_1 y + c_2, \quad (5.25)$$

$$u_1 = c_3 \sinh(m_2 y) + c_4 \cosh(m_2 y) + \frac{m_3 \bar{\lambda}_1}{m_2^2}, \quad (5.26)$$

where

$$c_1 = \frac{\lambda_0}{2\alpha_2} - \frac{m_1^2}{b_1^2}, \quad c_2 = 0, \quad c_3 = \frac{1}{\sinh(m_2)} \left( \frac{m_3 \bar{\lambda}_1}{m_2^2} (\cosh(m_2) - 1) \right), \quad c_4 = -\frac{m_3 \bar{\lambda}_1}{m_2^2}.$$

Finally,

$$u(y,t) = -\frac{\lambda_0 y^2}{2\alpha_2} + \frac{m_1^2}{b_1^2} \frac{\sin(b_1 y)}{\sin(b_1)} + \frac{\lambda_0}{2\alpha_2} y - \frac{m_1^2}{b_1^2} y + \varepsilon \exp(i\omega t) \left( \frac{\sinh(m_2 y)}{\sinh(m_2)} \left( \frac{m_3 \bar{\lambda}_1}{m_2^2} (\cosh(m_2) - 1) \right) + \frac{m_3 \bar{\lambda}_1}{m_2^2} (1 - \cosh(m_2 y)) \right). \quad (5.27)$$

## 5.7 Entropy generation

The local volumetric rate of entropy generation for nanofluids is defined by (Bejan, 1982; Butt & Ali, 2013) by:

$$S_G = \underbrace{\frac{\bar{k}_{nf}}{T_0^2} \left( \frac{\partial T}{\partial y} \right)^2}_{\text{entropy generation due to fluid friction}} + \underbrace{\frac{\bar{\mu}_{nf}}{T_0 (1 + \lambda_1)} \left( \frac{\partial u}{\partial y} \right)^2 + \frac{\lambda_2 \bar{\mu}_{nf}}{T_0 (1 + \lambda_1)} \left( \frac{\partial u}{\partial t} \right) \left( \frac{\partial^2 u}{\partial y^2} \right)}_{\text{entropy generation due to fluid friction or viscous dissipation}}. \quad (5.28)$$

In a dimensionless form, Equation (5.28) becomes:

$$Ns = \frac{S_G}{S_0} = \lambda_n \left( \frac{\partial T}{\partial y} \right)^2 + \frac{\alpha_1 \text{Br}}{\Omega} \left( \frac{\partial u}{\partial y} \right)^2 + \frac{\alpha_2 \text{Br}}{\Omega} \left( \frac{\partial u}{\partial t} \right) \left( \frac{\partial^2 u}{\partial y^2} \right), \quad (5.29)$$

where

$$S_0 = \frac{\bar{k} (T_w - T_0)^2}{T_0^2 \bar{h}^2}, \quad \text{Br} = \frac{\bar{\mu} u_r^2}{\bar{k} (T_w - T_0)}, \quad \Omega^{-1} = \frac{T_0}{T_w - T_0}.$$

Note that  $Ns$  is the ratio of the local volumetric generation rate to a characteristic entropy generation rate.  $S_0$  denotes the rate of characteristic entropy generation and  $\text{Br}$  is the Brickman number.

Introduce the irreversibility distribution parameter defined by

$$\text{Be} = \frac{\text{Entropy generation due to heat transfer}}{\text{Total entropy generation}}$$

Note that  $0 < \text{Be} < 1$ . When  $\text{Be} > 0.5$ , the entropy due to heat transfer dominates the entropy due to the fluid friction and the magnetic field.  $\text{Be} < 0.5$  indicates otherwise.

## 5.8 Nusselt Number and Skin-friction

The dimensionless Nusselt number and skin-friction are evaluated from Equations (5.24) and (5.27) as follows:

$$Nu = \left. \frac{dT}{dy} \right|_{y=0} = - \frac{b_1}{\sin b_1} \quad (5.30)$$

$$f = \left. \frac{du}{dy} \right|_{y=0} = \frac{m_1^2}{b_1} \frac{1}{\sin(b_1)} + \frac{\lambda_0}{2\alpha_2} - \frac{m_1^2}{b_1^2} - \frac{m_3 \bar{\lambda}}{m_2 \sinh(m_2)} (\cosh(m_2) + 1) + \frac{m_3 \bar{\lambda}_1}{m_2^2}. \quad (5.31)$$



## 5.9 Numerical Results and Discussion

In this section we study the behavior of the model with a varying Jeffery parameter, relaxation to retardation parameter, radiation parameter, Grashof number, and volume fraction of nanoparticles.

Recall that the thermophysical properties of the nanofluids are given in **Figures 5.1**. The spherical shape of  $MoS_2$  nanoparticles is used. The base fluid is water.

Unless stated otherwise, the model is analyzed with the following input parameters:  $Gr = 0.1$ ,  $N = 0.4$ ,  $Re = 1$ ,  $\lambda_1 = 1$ ,  $\lambda = 2$ ,  $\lambda_0 = 1$ ,  $\bar{\lambda}_1 = 1$ ,  $\phi = 0.1$ , **Figure 5.1-5.6**, **5.6-5.12** and **5.15-5.16** display the velocity, entropy generation, and the temperature profiles respectively.

### 5.9.1 Impact of the Different Parameters on the Velocity of Nanofluids

**Figures 5.1** and **5.2** show the effects the ratio of relaxation to retardation time on the velocity profile. Clearly, the velocity of the NN ( $\lambda_1 = \lambda = 0$ ) exceeds that of the non-Newtonian JN ( $\lambda_1 = 1, \lambda = 2$ ), and the non-Newtonian SGN ( $\lambda_1 = 0$ ). The SGN has the lowest velocity followed by the non-Newtonian JN. The velocity of the nanofluid increases with an increase of  $\lambda_1$ . An increase in the ratio of relaxation to retardation time parameter increases the viscoelasticity. In turn, the greater the elasticity of the nanofluid, the greater is the velocity. Further, the non-Newtonian JN becomes a NN when the relaxation time is equal to the retardation time,  $\lambda_1 = \lambda = 0$  (Jena et al., 2016). When  $\lambda_1 = 0, \lambda = 1$  the non-Newtonian JN becomes a non-Newtonian SGN. The results show that the NN are less viscous, compared to the non-Newtonian JN and the SGN, which complies with the general law of viscosity. The velocity is minimal at the walls and maximal at the midpoint of the channel.

The impact of the retardation time parameter on the velocity profile is shown in **Figure 5.3**. The velocity of the non-Newtonian JN decreases with an increase of the

retardation time parameter or the Jeffery parameter. Physically, this means that the nanofluid is getting thicker with increase of  $\lambda$ . Consequently, non-viscous fluids move faster than viscous fluids.

The impact of  $\phi$  is illustrated in **Figure 5.4**. An increase of  $\phi$  decreases the velocity due to the increase of the viscosity.

The impacts of  $Gr$  and  $N$  are shown in **Figures 5.5** and **5.6**. Radiation increases the velocity by increasing the heat rate, which in turn increases the buoyancy force and reduces the viscosity.

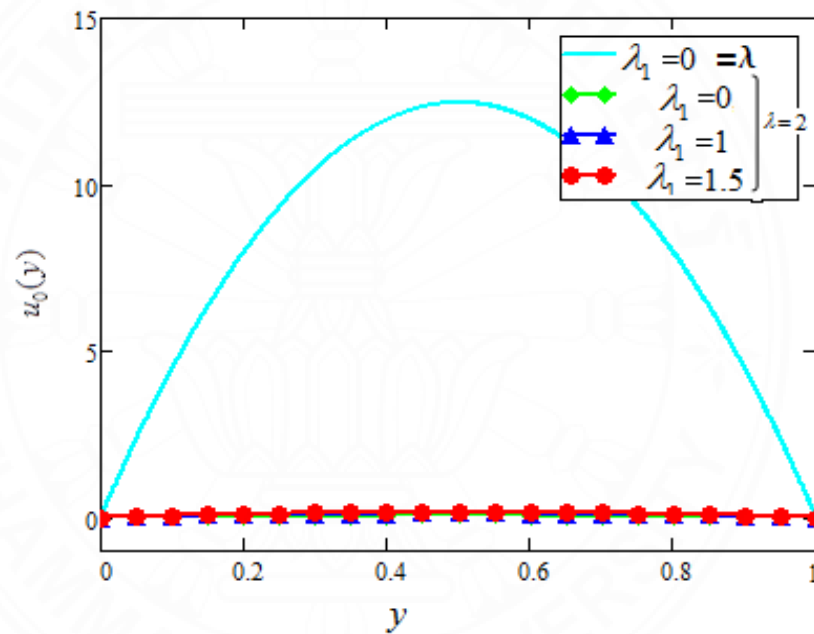


**Figure 5.1** MDJN, SGN, NN vs.  $\lambda_1$ .

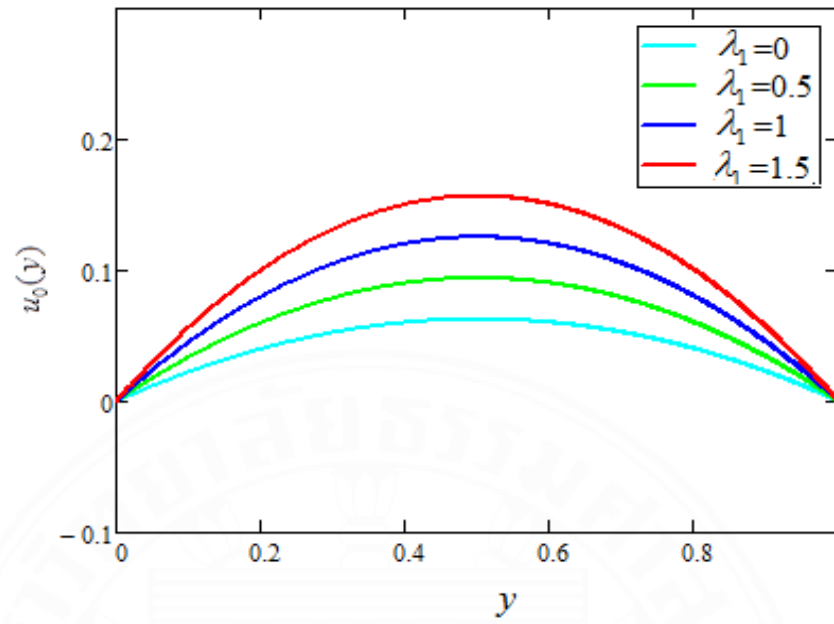


**Figure 5.2** Comparison of MDJN, SGN, and NN.

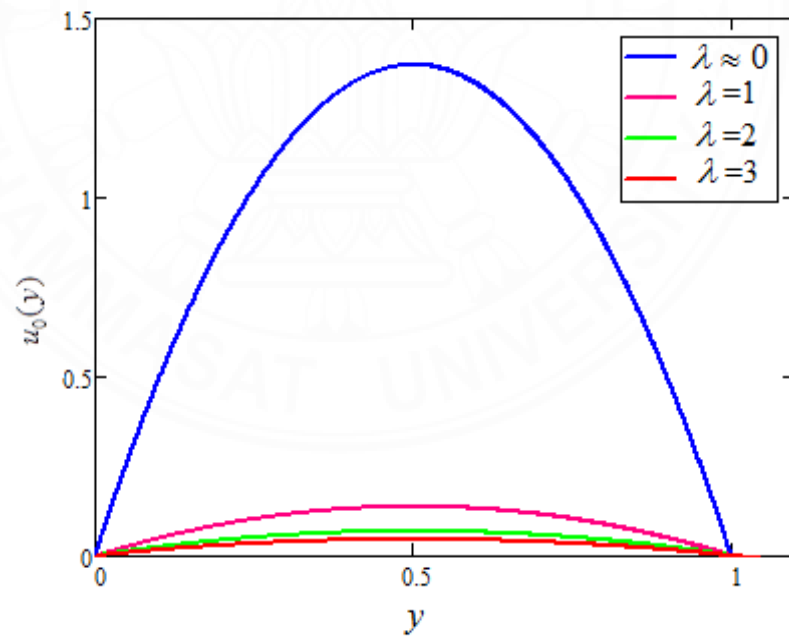


**Figure 5.3** Impact of  $\lambda$  on the velocity of MDJN.

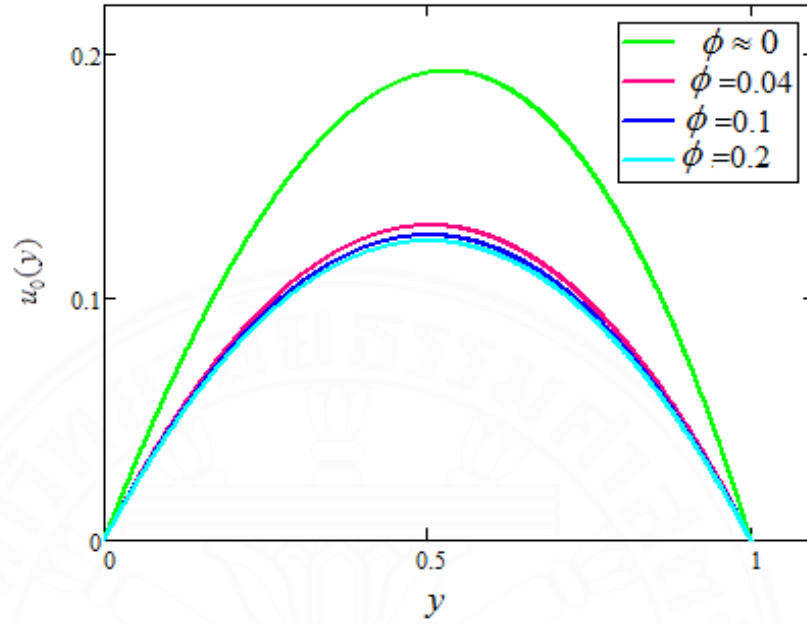


**Figure 5.4** Velocity of the MDJN vs.  $\phi$ .

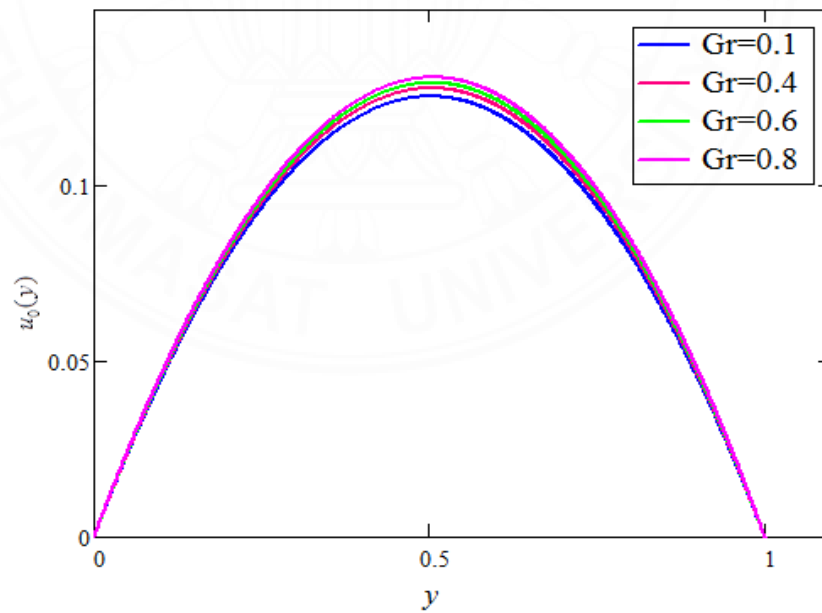


**Figure 5.5** Velocity of the MDJN vs.  $Gr$ .

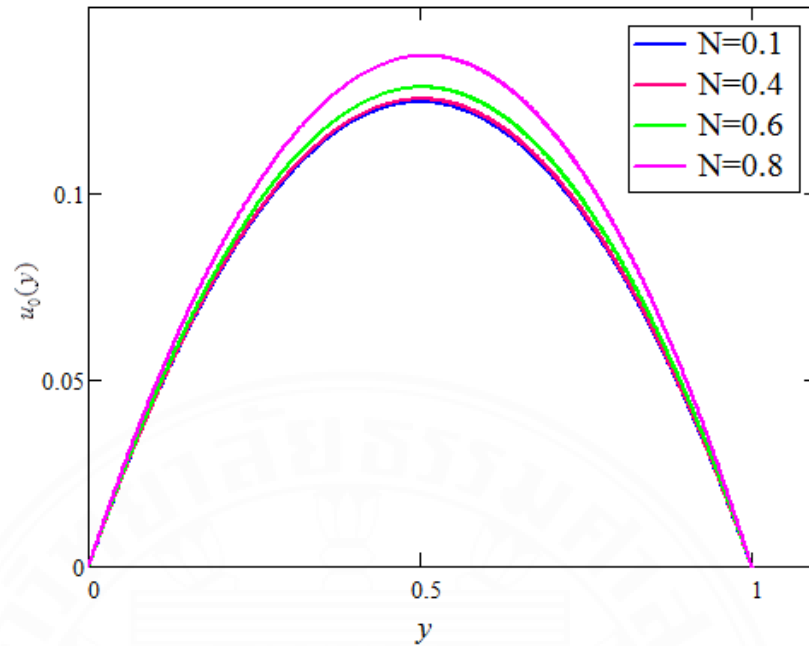


**Figure 5.6** Velocity of the MDJN vs.  $N$  .

### 5.9.2 Impact of the Different Parameters on Entropy Generation

**Figures 5.7** and **5.8** show the effect of  $\lambda_1$  and  $\lambda$  on entropy generation. The graphs of the entropy for the non-Newtonian JN and SGN intersect. Therefore, entropy generation for nonp-Newtonian JN can exceed or not exceed that of the SGN.

**Figures 5.9**, **5.10**, and **5.11** show the entropy generation vs.  $Br\Omega^{-1}$ ,  $Br$ , and  $\Omega$ , respectively. Note that **Figure 5.8** shows that the entropy generation decreases when the temperature increases. The heat flux increases the internal energy of the fluid. Recall that the Brickman number is defined as the ratio of the heat produced by the viscous dissipation to the heat transfer by conduction. Clearly, an increase of Brickman number means that a larger amount of heat has been produced through viscous dissipation, and a smaller amount of heat has been conducted through the molecules of the fluids. Therefore, increasing the Brickman number increases entropy generation. This increases the randomness of the

system. On the other hand, decreasing the temperature decreases entropy generation.

**Figure 5.12, 5.13 and 5.14** display the impact of  $\phi$ ,  $Gr$ , and  $N$ . Clearly, entropy generation decreases with an increase of the Grashof number, and increases with an increase of the volume fraction and the radiation parameter. The molecules of the liquid are arranged regularly when the volume fraction of nanoparticles is small. The irregularity increases with an increase of the amount of nanoparticles per unit volume.

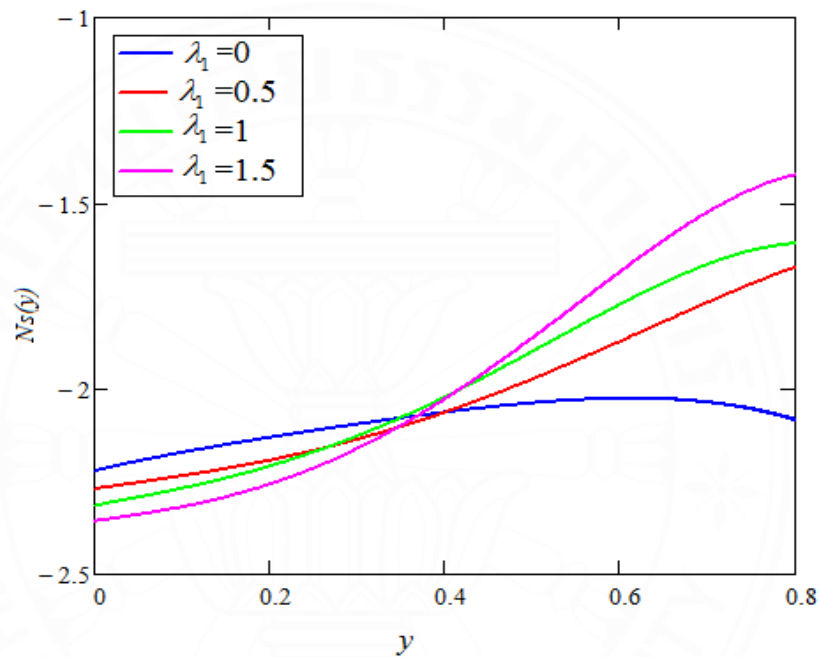


**Figure 5.7** Entropy generation of MDJN vs. the SGN vs.  $\lambda_1$ .

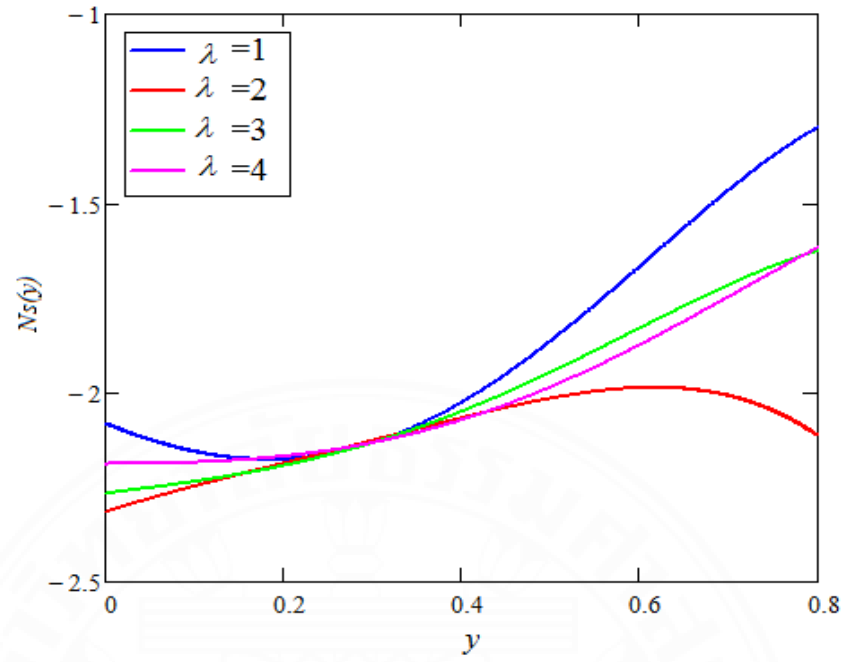


**Figure 5.8** Impact of  $\lambda$  on the entropy generation of MDJN.

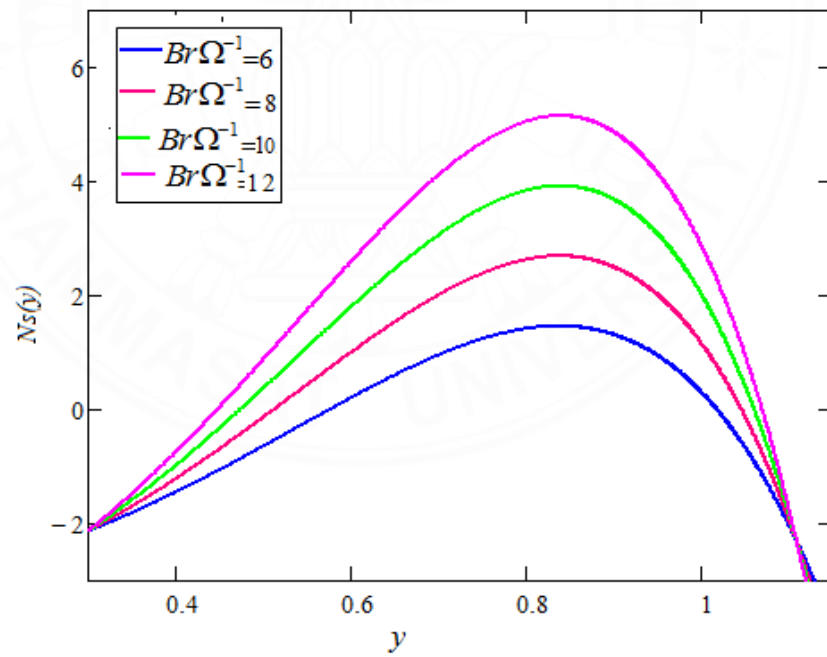


**Figure 5.9** Impact of  $Br\Omega^{-1}$  on the entropy generation.

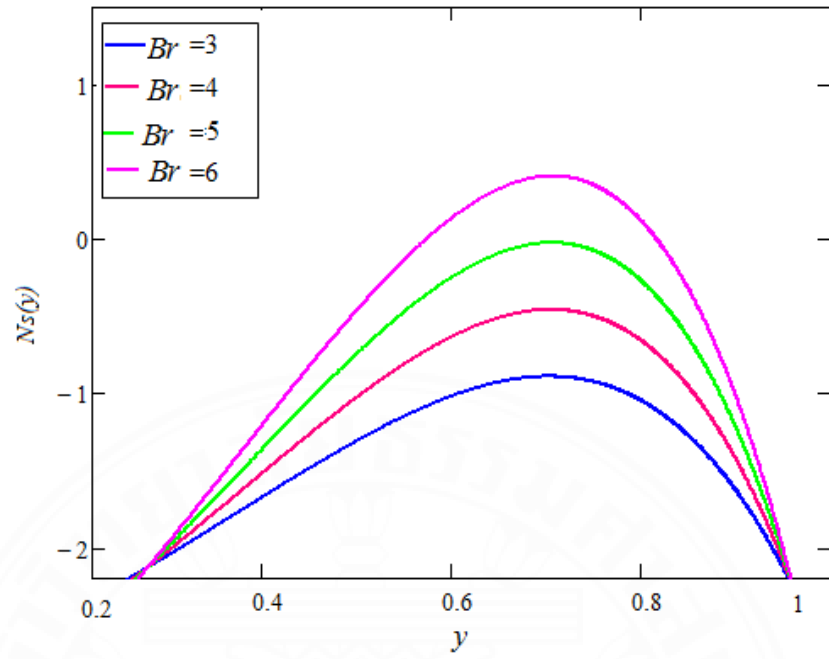


**Figure 5.10** Impact of  $Br$  on the entropy generation.

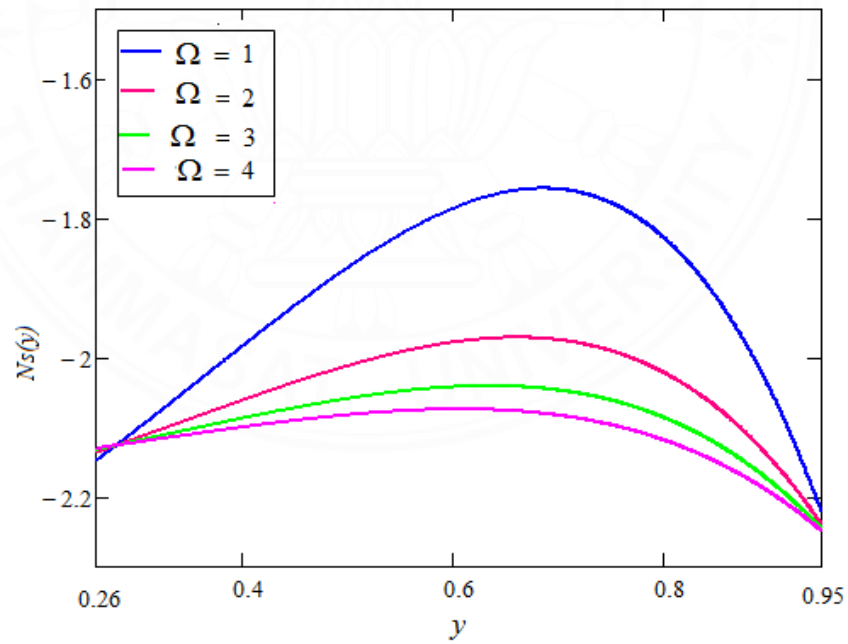


**Figure 5.11** Impact of  $\Omega$  on the entropy generation.



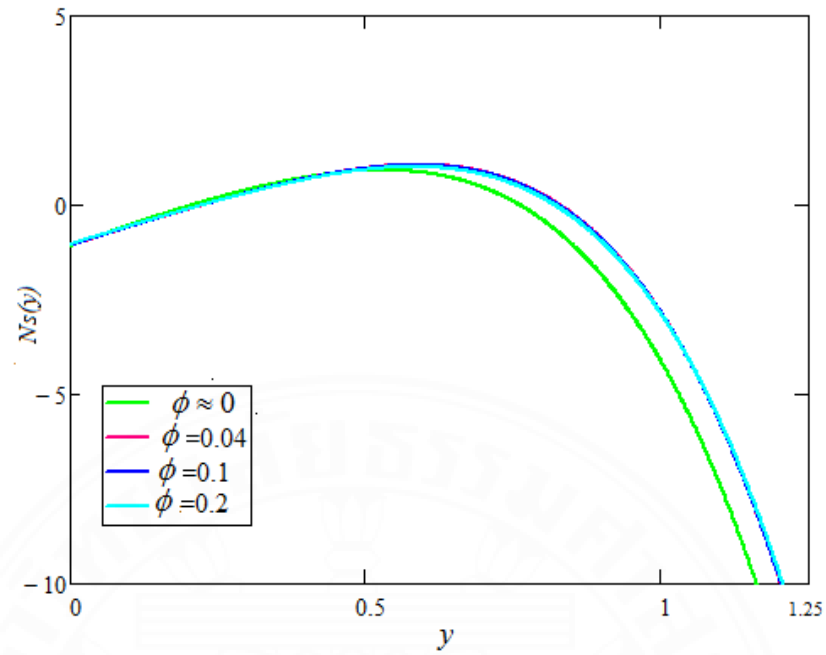


**Figure 5.12** Impact of  $\phi$  on the entropy generation.

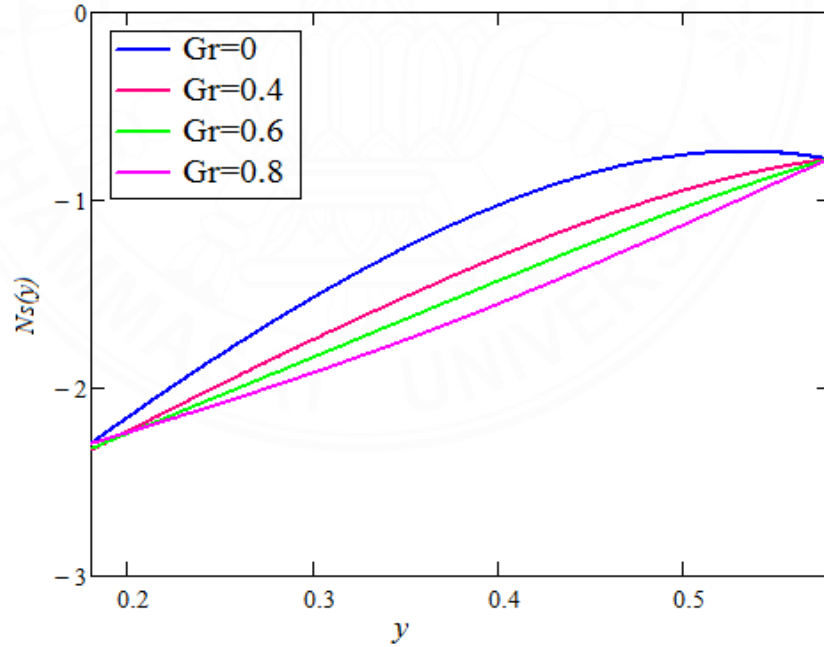


**Figure 5.13** Impact of  $Gr$  on the entropy generation.

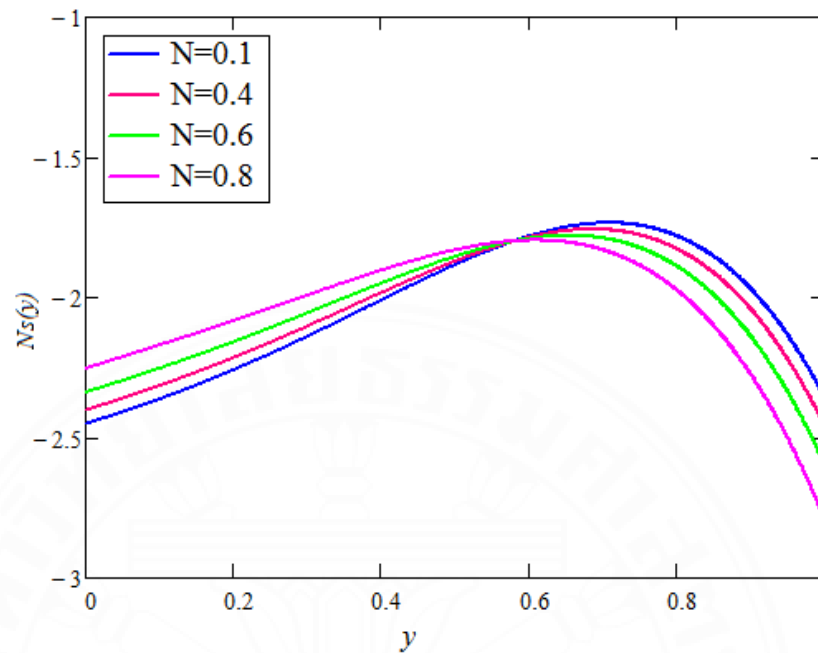


**Figure 5.14** Impact of  $N$  on the entropy generation.

### 5.9.3 Impact of the Different Parameters on Temperature of Nanofluids

The impact of  $N$  on the temperature is shown in **Figure 5.15**. Clearly, heating the nanofluid increases the emission of radiation. As a result, the temperature increases. **Figure 5.16** shows the impact of the volume fraction of nanoparticles on the temperature profile. Aaiza et al. (2015b) show that the temperature of NN decreases with an increase of volume fraction of nanoparticles. However, the effect of the volume fraction of nanoparticles on the temperature of a non-Newtonian MDJN, is different. Actually, in this case, the temperature decreases with increasing volume fraction of nanoparticles.

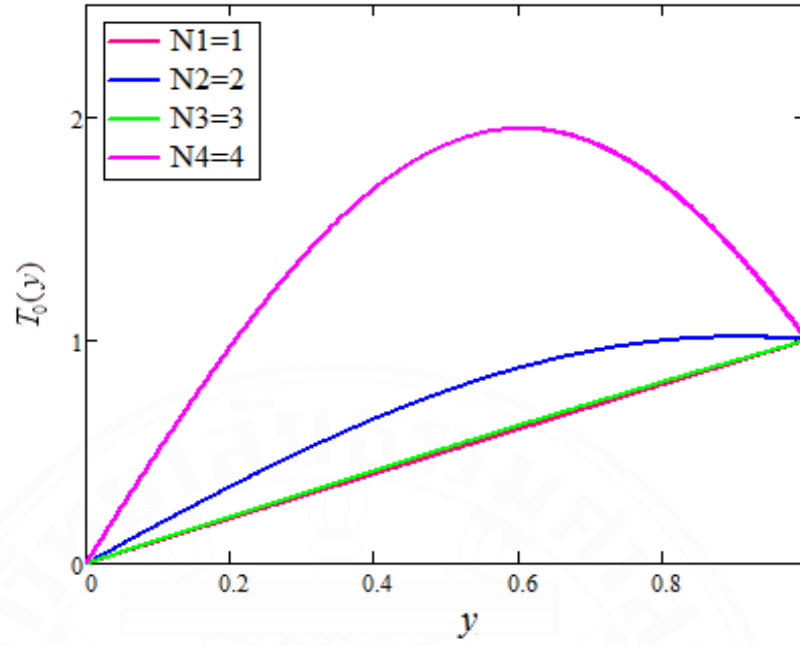


**Figure 5.15** Impact of  $N$  on the temperature of the MDJN.

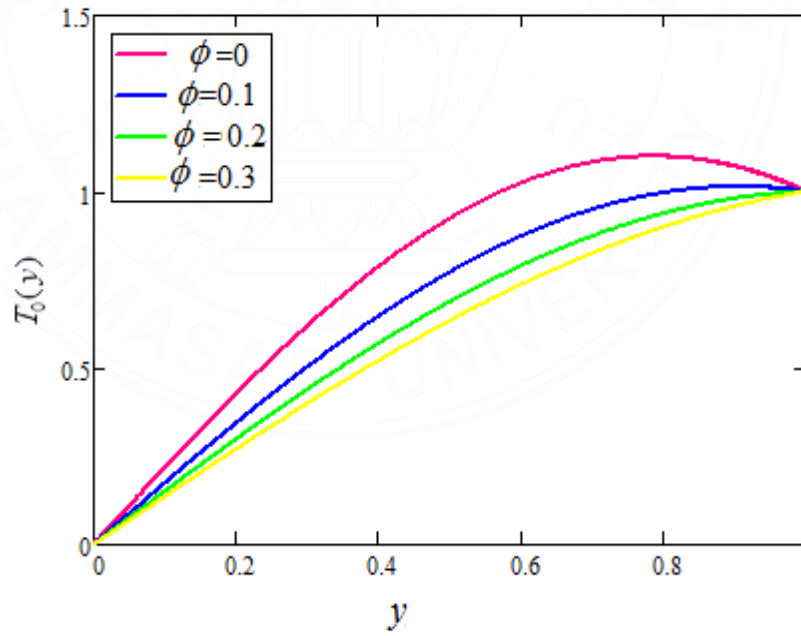


**Figure 5.16** Impact of  $\phi$  on the temperature of the MDJN.

## CHAPTER 6

### CONCLUSION

#### 6.1 Introduction

This chapter summarizes the results and presents the limitation of the present work. Some ideas of the future research are discussed.

#### 6.2 Conclusions

The Dissertation contributes to a better understanding of the TMDD and the relevant mathematical models. The proposed model makes it possible to simulate the behavior of the MN-blood flow inside the vessels and tissues. The impact of the MF and the position of the magnet are analyzed.

The most important feature of the model is the possibility to evaluate the inverse impact of the MN on the blood flow. The numerical experiments show the possibility to evaluate the impact of the Reynolds number on the topology of the blood flow and the MN flow. For  $Re > 100$  and the MF characterized by  $B \in [0.5, 1]$  T, the DF works against the MF. The TMDD region (low blood velocity) becomes small and the magnitude of the MN flow in this region decreases. The model is capable of simulating the impact of the MF and the position of the magnet. Positioning the magnet close to the desired TMDD region and applying a strong MF  $B = 1$  T generates large TMDD regions. However, the topological structure of the blood flow is characterized by increased vorticity. In particular, the closest position of the magnet ( $b = 5$  cm) generates a complicated flow with several vortices extending across the entire vessel.

Our conjecture, supported by medical (experimental) research, is that the increased vorticity may harm the patient in the case of long-term treatment. The model shows that

the size of the MN has an impact on the dynamics of the flow. Large nanoparticles create a large TMDD zone where the MN moves faster to the target. However, it is well known that the large MN may damage the blood vessels and cause blood leakage. This is not included in the model. Finally, the two-way coupled energy equations analyze the impact of the size of the MN on the temperature of the blood flow. The model shows that under certain conditions, the large MN include a temperature increase of about 2°C (from 37 to 39°C) over a relatively large region inside the vessel. Clearly, such an increase combined with the increased vorticity may lead to a negative impact on the patient.

In this Chapter 4, a three-layer mathematical model is discussed. The mass transport of magnetic nanoparticles (MN) from a blood vessel (artery) to the endothelial membrane and tissue via leaky tumor arteries has been investigated. The blood and tumor vessels are notoriously leaky. The general formulation for the effect of the magnetic field is that of BFD which incorporates both principles of MHD and FHD. To analyze the effect of Lorentz force, a special case has been discussed. The obtained result shows that the additional Lorentz force (MHD) reduces blood flow and suppresses the large vortices created by FHD flows. The MN flow, on the other hand, is not significantly affected. Despite the small disturbance in MN flow caused by Lorentz force, the model shows that MHD effects are significant when the applied magnetic field is uniform and smooth.

Another important result is the concentration of medicinal drugs. These drugs can also harm healthy cells. Therefore, medical drug effects must be weighed against MN size. Our findings suggest that as we increase the drug concentration from 30% to 50%, the size of the vortices increases. The difference is insignificant when  $d=250$  nm. However, the TMDD zone grew significantly when the size of MN (20,000) was increased while keeping the drug concentration as 50%.

Furthermore, we investigate the concentration of drug-loaded MN in normal and leaky blood arteries, both with and without an external magnetic field. The result shows that MN starts leaving the vessel through endothelial pores when  $D_M$  and  $D_T$  are greater than zero and blood cells are leaky. However, the concentration remains inside the

endothelium membrane, preventing it from reaching tumorous tissue via diffusion alone. Nevertheless, the external MFs dragged the particles towards the tumorous tissue and enhanced the concentration of MN.

The entropy analysis in a mixed convection Poiseuille flow of an MDJN has been analyzed in Chapter 5. The numerical results show that increasing the volume fraction of the MN decreases the velocity of ferrofluids. Besides the velocity of the nanofluid increases when the relaxation to retardation time parameter increases and vice versa. Increasing decreases the velocity since fluid gets more viscous. The velocity of the fluid increases with increasing the thermal Grashof number and radiation parameter. When the radiation parameter increases the temperature of the fluid increases as well.

### **6.3 Limitations of the Present Work**

The model has a number of limitations. The magnet is represented as a pointwise wire. However, the shape of the magnet can vary. The corresponding MF depends on the shape and the orientation of the magnet. This effect has not been fully considered. The dependence of the heat transfer on the MF has not been considered either. The model does not include a number of important effects such as the Brownian motion of the nanoparticles, the acoustic radiation force, the lift force (Saffman & Magnus effects), and the thermophoretic force. Finally, the shape of the MN (an important factor) has not been included in the proposed two-phase equations. Therefore, future research includes further validation of the model using new experimental results and modifying the model to include the above-mentioned effects.

### **6.4 Suggestions for Future Research**

Since validation of the proposed model depends upon the experimental studies. At this point, the measurements of the velocity of the MN-blood flow during TMDD are not available in the literature. The model has been validated using the measurements of the Nusselt number. Therefore, it is important, to validate the model once such measurements

are published. Alternatively, there might be a way to validate the model using the MRI images during the TMDD.

#### **6.4.1 Damage to Vessels and Tissues**

These magnetic nanoparticles are forcefully dragged to the biological environment (membranes and tissues). These forces depend on the shape and size of the MN. Modeling this damage is a subject of future research.

#### **6.4.2 Aggregation of MN**

A recent study (Karvelas et al., 2021) shows the importance of aggregation of the magnetic carriers. We propose future research along the lines of including these effects in the proposed model.

#### **6.4.3 Implanted Magnet**

When an external MF is applied, the magnet is not in direct contact with the cancerous region. However, several research works introduce a magnetic implant or stent. The magnets are implanted near the cancerous region. The TMDD region is in direct contact with the magnet. Although, a magnet implant is not suitable for every patient and every clinical condition. Potentially harmful procedures are often required for placing such magnets (Donson, 2006; Hayden & Hafeli, 2006; Shapiro, 2009; Cao & Han, 2011). However, the technology is promising and can be simulated using the proposed model.

#### **6.4.4 Longer Circulation Nanoparticles**

Most magnetic nanoparticles, when injected into the blood, are removed within minutes or hours by the cells of the mononuclear phagocyte system (MPS). When the MN is modified by adding Poly(Ethylene) Glycol (PEG) to its surface, this increases drastically enhances the half-life of the MN inside the bloodstream. The purpose of the “stealth” MN is to maximize the half-life (Albanese et al., 2012). Simulation of this effect using the proposed model is another direction of future research.





## REFERENCES

- Afshari, F., Tuncer, A.D., Sözen, A., Variyenli, H.I., Khanlari, A. & Gürbüz, E.Y. (2021). A comprehensive survey on utilization of hybrid nanofluid in plate heat exchanger with various number of plates, *International Journal of Numerical Methods for Heat & Fluid Flow*, (in print).
- Abrougui, M. M., Srasra, E., Lopez-Lopez, M. T., & Duran, J. D. (2020). Rheology of magnetic colloids containing clusters of particle platelets and polymer nanofibres. *Philosophical Transactions of the Royal Society A*, 378(2171), 20190255.
- Abadeh, A., Sardarabadi, M., Abedi, M., Pourramezan, M., Passandideh-Fard, M., & Maghrebi, M. J. (2020). Experimental characterization of magnetic field effects on heat transfer coefficient and pressure drop for a ferrofluid flow in a circular tube. *Journal of Molecular Liquids*, 299, 112206.
- Alsabery A.I., Armaghani T., Chamkha A.J., & Hashim, I. (2020). Two-phase nanofluid model and magnetic field effects on mixed convection in a lid-driven cavity containing heated triangular wall, *Alexandria Engineering Journal*, 59(1), 129-148.
- Aaiza, G., Ilyas, K., & Sharidan, S., Energy transfer in mixed convection flow of nanofluids, published, LAP LAMBERT Academic Publishing OmniScriptum GmbH & Co. KG Bahnhofstraße 28, D-66111, Saarbrücken, Germany.
- Aaiza, G. (2016). *Energy transfer in mixed convection flow of nanofluids*. University Teknologi Malaysia, JB, Malaysia.

- Aaiza, G., Khan, I., Shafie, S., Khalid, A., & Khan, A. (2015). Heat transfer in MHD mixed convection flow of a ferrofluid along a vertical channel. *PloS one*, *10*(11), e0141213.
- Aaiza, G., Khan, I., & Shafie, S. (2015). Energy transfer in mixed convection MHD flow of nanofluid containing different shapes of nanoparticles in a channel filled with saturated porous medium. *Nanoscale Research Letters*, *10*(1), 1-14.
- Alshare A., & Tashtoush, B. (2016). Simulations of magneto hemodynamics in stenosed arteries in diabetic or anemic models, *Computational and Mathematical Methods in Medicine 2016*, article ID 8123930, 1-13.
- Au, J. L. S., Yeung, B. Z., Wientjes, M. G., Lu, Z., & Wientjes, M. G. (2016). Delivery of cancer therapeutics to extracellular and intracellular targets: Determinants, barriers, challenges and opportunities. *Advanced Drug Delivery Reviews*, *97*, 280-301.
- Albanese, A., Tang, P. S., & Chan, W. C. (2012). The effect of nanoparticle size, shape, and surface chemistry on biological systems. *Annual Review of Biomedical Engineering*, *14*, 1-16.
- Alexiou, C., Tietze, R., Schreiber, E., Jurgons, R., Richter, H., Trahms, L., Rahn, H., Odenbach, S., & Lyer, S. (2011). Cancer therapy with drug loaded magnetic nanoparticles—Magnetic drug targeting. *Journal of Magnetism and Magnetic Materials*, *323*(10), 1404–1407.
- Alexiou, C., Arnold, W., Hulin, P., Klein, R. J., Renz, H., Parak, F. G., & Lübbe, A. S. (2001). Magnetic mitoxantrone nanoparticle detection by histology, X-ray and MRI

- after magnetic tumor targeting. *Journal of Magnetism and Magnetic Materials*, 225(1-2), 187-193.
- Alexiou, C., Arnold, W., Klein, R. J., Parak, F. G., Hulin, P., Bergemann, C., & Luebbe, A. S. (2000). Locoregional cancer treatment with magnetic drug targeting. *Cancer Research*, 60(23), 6641-6648.
- Bletsos, G., Kühn, N., & Rung, T. (2021). Adjoint-based shape optimization for the minimization of flow-induced hemolysis in biomedical applications, *Engineering Applications of Computational Fluid Mechanics*, 15(1), 1095–1112.
- Boutopoulos, I. D., Lampropoulos, D. S., Bourantas, G. C., Miller, K., & Loukopoulos, V. C. (2020). Two-Phase Biofluid Flow Model for Magnetic Drug Targeting. *Symmetry*, 12(7), 1060-1083.
- Baghban, A., Sasanipour, J., Pourfayaz, F., Ahmadi, M.H., Kasaeian, A Chamkha, A.J., Oztop, H.F., & Chau, K.-W. (2019). Towards experimental and modeling study of heat transfer performance of water-SiO<sub>2</sub> nanofluid in quadrangular cross-section channels, *Engineering Applications of Computational Fluid Mechanics* 13 (1), 453-469.
- Bortoli, A.L., Andreis, G., & Pereira, F. (2015). Numerical methods for reactive flows, Elsevier, 123-169.
- Bose, S., & Banerjee, M. (2015). Magnetic particle capture for biomagnetic fluid flow in stenosed aortic bifurcation considering particle–fluid coupling. *Journal of Magnetism and Magnetic Materials*, 385, 32-46.

- Bianco, V., Chiacchio, F., Manca, O., & Nardini, S. (2009). Numerical investigation of nanofluids forced convection in circular tubes. *Applied Thermal Engineering*, 29(17-18), 3632-3642.
- Bali, R., & Awasthi, U. (2007). Effect of a magnetic field on the resistance to blood flow through stenotic artery, *Applied Mathematics and Computation*, 188(2), 1635-1641.
- Buongiorno, J. (2006). Convective transport in nanofluids.
- Benavente, E., Santa Ana, M. A., & Gonzalez, G. (2004). Electrical conductivity of MoS<sub>2</sub> based organic–inorganic nanocomposites. *Physica Status Solidi (b)*, 241(10), 2444-2447.
- Burke, D., Carnochan, P., Glover, C., & Allen-Mersh, T. G. (2000). Correlation between tumour blood flow and fluorouracil distribution in a hypovascular liver metastasis model. *Clinical & Experimental Metastasis*, 18(7), 617.
- Baxter, L. T., & Jain, R. K. (1990). Transport of fluid and macromolecules in tumors. II. Role of heterogeneous perfusion and lymphatics. *Microvascular Research*, 40(2), 246-263.
- Baxter, L. T., & Jain, R. K. (1991). Transport of fluid and macromolecules in tumors: III. Role of binding and metabolism. *Microvascular Research*, 41(1), 5-23.
- Bejan, A. (1982). *Entropy generation through heat and fluid flow* (Vol. 1). New York: Wiley.
- Contijoch, F. J., Horowitz, M., Masutani, E., Kligerman, S., & Hsiao, A. (2020). 4D Flow vorticity visualization predicts regions of quantitative flow inconsistency for

- optimal blood flow measurement. *Radiology: Cardiothoracic Imaging*, 2(1), e190054.
- Carlier, C., Mathys, A., De Jaeghere, E., Steuperaert, M., De Wever, O., & Ceelen, W. (2017). Tumour tissue transport after intraperitoneal anticancer drug delivery. *International Journal of Hyperthermia*, 33(5), 534-542.
- Ceelen, W. P., & Levine, E. (Eds.). (2015). *Intraperitoneal cancer therapy: principles and practice*. CRC Press.
- Colla, L., Fedele, L., Scattolini, M., & Bobbo, S. (2012). Water-based Fe<sub>2</sub>O<sub>3</sub> nanofluid characterization: thermal conductivity and viscosity measurements and correlation. *Advances in Mechanical Engineering*, 4, 674947.
- Cregg, P. J., Murphy, K., & Mardinoglu, A. (2012). Inclusion of interactions in mathematical modelling of implant assisted magnetic drug targeting. *Applied Mathematical Modelling*, 36(1), 1-34.
- Chauhan, V. P., Stylianopoulos, T., Boucher, Y., & Jain, R. K. (2011). Delivery of molecular and nanoscale medicine to tumors: transport barriers and strategies. *Annual Review of Chemical and Biomolecular Engineering*, 2, 281-298.
- Cao, Q., Han, X., & Li, L. (2011). Enhancement of the efficiency of magnetic targeting for drug delivery: Development and evaluation of magnet system. *Journal of Magnetism and Magnetic Materials*, 323(15), 1919-1924.
- Chertok, B., David, A.E., & Yang, V.C. (2010). Polyethyleneimine-modified iron oxide nanoparticles for brain tumor drug delivery using magnetic targeting and intra-carotid administration. *Biomaterials* 31, 6317–6324.

- Cervera, M., Codina, R. & Galindo, M. (1996). On the computational efficiency and implementation of block-iterative algorithms for nonlinear coupled problems, *Engineering Computations*, 13(6), 4-30.
- Dewhirst, M. W., & Secomb, T. W. (2017). Transport of drugs from blood vessels to tumour tissue. *Nature Reviews Cancer*, 17(12), 738-750.
- Ding, Y., & Xiao, B. (2015). Thermal expansion tensors, Grüneisen parameters and phonon velocities of bulk MT<sub>2</sub> (M= W and Mo; T= S and Se) from first principles calculations. *Rsc Advances*, 5(24), 18391-18400.
- Das, S., & Jana, R. N. (2015). Natural convective magneto-nanofluid flow and radiative heat transfer past a moving vertical plate. *Alexandria Engineering Journal*, 54(1), 55-64.
- Dalir, N. (2014). Numerical study of entropy generation for forced convection flow and heat transfer of a Jeffrey fluid over a stretching sheet. *Alexandria Engineering Journal*, 53(4), 769-778.
- Das, S. K., Choi, S. U., Yu, W., & Pradeep, T. (2008). *Nanofluids-Science and Technology*. John Wiley & Sons. Inc., Hoboken.
- Dobson, J. (2006). Magnetic micro-and nano-particle-based targeting for drug and gene delivery. *Future NanoMedicine*, 1(1), 31-37.
- Deerasamee, S., Martin, N., Sontipong, S., Sriamporn, S., Sriplung, H., Srivatanakul, P., & Parkin, D. (2001). Cancer registration in Thailand. *Asian Pacific Journal Cancer Prevention*, 2, 79-84.

- Ellahi, R., Hassan, M., Zeeshan, A., & Khan, A. A. (2016). The shape effects of nanoparticles suspended in HFE-7100 over wedge with entropy generation and mixed convection. *Applied Nanoscience*, 6(5), 641-651.
- Rashidi, M. M., Abelman, S., & Mehr, N. F. (2013). Entropy generation in steady MHD flow due to a rotating porous disk in a nanofluid. *International Journal of Heat and Mass Transfer*, 62, 515-525.
- Fernández, M., Javaid, F., & Chudasama, V. (2018). Advances in targeting the folate receptor in the treatment/imaging of cancers. *Chemical Science*, 9(4), 790-810.
- Forbes, Z. G., Yellen, B. B., Halverson, D. S., Fridman, G., Barbee, K. A., & Friedman, G. (2008). Validation of high gradient magnetic field based drug delivery to magnetizable implants under flow. *IEEE Transactions on Biomedical Engineering*, 55(2), 643-649.
- Fournier, R. L. (2017). *Basic transport phenomena in biomedical engineering*. CRC press.
- Fukumura, D., & Jain, R. K. (2007). Tumor microenvironment abnormalities: causes, consequences, and strategies to normalize. *Journal of Cellular Biochemistry*, 101(4), 937-949.
- Fernández-Pacheco, R., Marquina, C., Valdivia, J. G., Gutiérrez, M., Romero, M. S., Cornudella, R., & Ibarra, M. R. (2007). Magnetic nanoparticles for local drug delivery using magnetic implants. *Journal of Magnetism and Magnetic Materials*, 311(1), 318-322.
- Furlani, E. P. (2001). *Permanent magnet and electromechanical devices: Materials, Analysis, and Applications*. Academic Press.

- Geranpayehvaghei, M., Dabirmanesh, B., Khaledi, M., Atabakhshi-Kashi, M., Gao, C., Taleb, M., & Nie, G. (2021). Cancer-associated-platelet-inspired nanomedicines for cancer therapy. *Wiley Interdisciplinary Reviews: Nanomedicine and Nanobiotechnology*, e1702.
- Granados-Ortiz, F.-J., Leon-Prieto, L., & Ortega-Casanova J. (2021). Computational study of the application of Al<sub>2</sub>O<sub>3</sub> nanoparticles to forced convection of high-Reynolds swirling jets for engineering cooling processes, *Engineering Applications of Computational Fluid Mechanics*, 15(1), 1-22.
- Ghalandari, M., Mirzadeh, E., Mohamadian, K.F., Shamshirband, S., & Chau K.W. (2019). Numerical simulation of nanofluid flow inside a root canal, *Engineering Applications of Computational Fluid Mechanics*, 13(1), 254-264.
- Giresha, B. J., Venkatesh, P., Shashikumar, N. S., & Prasannakumara, B. C. (2017). Boundary layer flow of dusty fluid over a radiating stretching surface embedded in a thermally stratified porous medium in the presence of uniform heat source. *Nonlinear Engineering*, 6(1), 31-41.
- Goharkhah, M., & Ashjaee, M. (2014). Effect of an alternating nonuniform magnetic field on ferrofluid flow and heat transfer in a channel. *Journal of Magnetism and Magnetic Materials*, 362, 80-89.
- Gu, S., Zhang, Y., & Yan, B. (2013). Solvent-free ionic molybdenum disulfide (MoS<sub>2</sub>) nanofluids with self-healing lubricating behaviors. *Materials Letters*, 97, 169-172.
- Grief, A. D., & Richardson, G. (2005). Mathematical modelling of magnetically targeted drug delivery. *Journal of Magnetism and Magnetic Materials*, 293(1), 455-463.



- Ganguly, R., Gaiind, A. P., Sen, S., & Puri, I.K. (2005). Analyzing ferrofluid transport for magnetic drug targeting. *Journal of Magnetism and Magnetic Materials*, 289, 331-334.
- Goodwin, S. C., Bittner, C. A., Peterson, C. L., & Wong, G. (2001). Single-dose toxicity study of hepatic intra-arterial infusion of doxorubicin coupled to a novel magnetically targeted drug carrier. *Toxicological Sciences*, 60(1), 177-183.
- Goodwin, S., Peterson, C., Hoh, C., & Bittner, C. (1999). Targeting and retention of magnetic targeted carriers (MTCs) enhancing intra-arterial chemotherapy. *Journal of Magnetism and Magnetic Materials*, 194(1), 132-139.
- Gordon, W.J., & Thiel, L.C. (1982). Transfinite mappings and their application to grid generation, *Applied Mathematics and Computation*, 10–11, 171-233.
- Gray, L. H., Conger, A., Ebert, M., Hornsey, S., & Scott, O. C. A. (1953). The concentration of oxygen dissolved in tissues at the time of irradiation as a factor in radiotherapy. *The British journal of radiology*, 26(312), 638-648.
- Fournier, R. L. (2017). *Basic Transport Phenomena in Biomedical Engineering*. CRC press.
- Hamdipoor, V., Afzal, M. R., Le, T. A., & Yoon, J. (2018). Haptic-based manipulation scheme of magnetic nanoparticles in a multi-branch blood vessel for targeted drug delivery. *Micromachines*, 9(1), 14.
- Habibi, M. R., & Ghasemi, M. (2011). Numerical study of magnetic nanoparticles concentration in biofluid (blood) under influence of high gradient magnetic field. *Journal of Magnetism and Magnetic Materials*, 323(1), 32-38.

- Haverkort, J. W., Kenjereš, S., & Kleijn, C. R. (2009). Computational simulations of magnetic particle capture in arterial flows. *Annals of Biomedical Engineering*, 37(12), 2436-2448.
- Hatakeyama, H., Akita, H., Ishida, E., Hashimoto, K., Kobayashi, H., Aoki, T., & Kiwada, H. (2007). Tumor targeting of doxorubicin by anti-MT1-MMP antibody-modified PEG liposomes. *International Journal of Pharmaceutics*, 342(1-2), 194-200.
- Hayden, M. E., & Häfeli, U. O. (2006). Magnetic bandages for targeted delivery of therapeutic agents. *Journal of Physics: Condensed Matter*, 18(38), S2877.
- Han, K. H., & Frazier, A. B. (2006). Paramagnetic capture mode magnetophoretic microseparator for high efficiency blood cell separations. *Lab on a Chip*, 6(2), 265-273.
- Haddad, O. M., Alkam, M. K., & Khasawneh, M. T. (2004). Entropy generation due to laminar forced convection in the entrance region of a concentric annulus. *Energy*, 29(1), 35-55.
- Haik, Y., Pai, V., & Chen, C. J. (1999). Development of magnetic device for cell separation. *Journal of Magnetism and Magnetic Materials*, 194(1-3), 254-261.
- Haik, Y., Chen, J. C., & Pai, V. M. (1996b). Development of bio-magnetic fluid dynamics. *In Proceedings of the IX international symposium on transport properties in thermal fluids engineering, Singapore, Pacific Center of Thermal Fluid Engineering* (pp. 121-126). Hawaii, USA.
- Higashi, T., Yamagishi, A., Takeuchi, T., Kawaguchi, N., Sagawa, S., Onishi, S., & Date, M. (1993). Orientation of erythrocytes in a strong static magnetic field.

- Jena, S., Mishra, S. R., & Dash, G. C. (2017). Chemical reaction effect on MHD Jeffery fluid flow over a stretching sheet through porous media with heat generation/absorption. *International Journal of Applied and Computational Mathematics*, 3(2), 1225-1238.
- Jeon M.J., Gordon A.C., Larson A.C., Chung J.W., Kim Y.I., & Kim D.H. (2016). Transcatheter intra-arterial infusion of doxorubicin loaded porous magnetic nano-clusters with iodinated oil for the treatment of liver cancer. *Biomaterials*, 88, 25–33.
- Jain, R. K., Martin, J. D., & Stylianopoulos, T. (2014). The role of mechanical forces in tumor growth and therapy. *Annual Review of Biomedical Engineering*, 16, 321-346.
- Jain, R. K., & Stylianopoulos, T. (2010). Delivering nanomedicine to solid tumors. *Nature Reviews Clinical Oncology*, 7(11), 653.
- Jain, S., Mishra, V., Singh, P., Dubey, P. K., Saraf, D. K., & Vyas, S. P. (2003). RGD-anchored magnetic liposomes for monocytes/neutrophils-mediated brain targeting. *International Journal of Pharmaceutics*, 261(1), 43-55.
- Karvelas, E. G., Lampropoulos, N. K., Benos, L. T., Karakasidis, T., & Sarris, I. E. (2021). On the magnetic aggregation of Fe<sub>3</sub>O<sub>4</sub> nanoparticles. *Computer Methods and Programs in Biomedicine*, 198, 105778.
- Kenjereš, S., & Tjin, J. L. (2017). Numerical simulations of targeted delivery of magnetic drug aerosols in the human upper and central respiratory system: A validation study. *Royal Society Open Science*, 4(12), 170873.

- Kenjereš, S., & Tjin, J. L. (2018). Numerical simulations of targeted delivery of magnetic drug aerosols in the human upper and central respiratory system: a validation study. *Royal Society Open Science*, 4(12), 170873.
- Kandelousi, M. S., & Ellahi, R. (2015). Simulation of ferrofluid flow for magnetic drug targeting using the lattice-Boltzmann method. *Zeitschrift für Naturforschung A*, 70, 115–124.
- Kenjereš, S. (2014). Modeling and simulation of multi-physics multi-scale transport phenomena in bio-medical applications. In *Journal of Physics: Conference Series*, 530(1), 012006, IOP Publishing.
- Kenjereš, S., & Righolt, B. (2012). Simulations of magnetic capturing of drug carriers in the brain vascular system. *International Journal of Heat and Fluid Flow*, 35, 68–75.
- Krukemeyer, M. G., Krenn, V., Jakobs, M., & Wagner, W. (2012). Mitoxantrone-iron oxide biodistribution in blood, tumor, spleen, and liver—magnetic nanoparticles in cancer treatment. *Journal of Surgical Research*, 175(1), 35-43.
- Krukemeyer, M. G., Krenn, V., Jakobs, M., & Wagner, W. (2012). Mitoxantrone-iron oxide biodistribution in blood, tumor, spleen, and liver—Magnetic nanoparticles in cancer treatment. *Journal of Surgical Research*, 175(1), 35-43.
- Kayal, S., Bandyopadhyay, D., Mandal, T. K., & Ramanujan, R. V. (2011). The flow of magnetic nanoparticles in magnetic drug targeting. *Royal Society of Chemistry Advances*, 1(2), 238-246.

- Kenjereš, S. (2008). Numerical analysis of blood flow in realistic arteries subjected to strong non-uniform magnetic fields. *International Journal of Heat and Fluid Flow*, 29(3), 752-764.
- Kirpotin, D. B., Drummond, D. C., Shao, Y., Shalaby, M. R., Hong, K., Nielsen, U. B., & Park, J. W. (2006). Antibody targeting of long-circulating lipidic nanoparticles does not increase tumor localization but does increase internalization in animal models. *Cancer Research*, 66(13), 6732-6740.
- Kato, H., Takama, M., Iwai, Y., Washida, K., & Sasaki, Y. (2003). Wear and mechanical properties of sintered copper–tin composites containing graphite or molybdenum disulfide. *Wear*, 255(1-6), 573-578.
- Kinouchi, Y., Yamaguchi, H., & Tenforde, T. S. (1996). Theoretical analysis of magnetic field interactions with aortic blood flow. *Bioelectromagnetics: Journal of the Bioelectromagnetics Society, The Society for Physical Regulation in Biology and Medicine, The European Bioelectromagnetics Association*, 17(1), 21-32.
- Le, T. N., Straatman, L. V., Lea, J., & Westerberg, B. (2017). Current insights in noise-induced hearing loss: a literature review of the underlying mechanism, pathophysiology, asymmetry, and management options. *Journal of Otolaryngology-Head & Neck Surgery*, 46(1), 1-15.
- Luong, D., Sau, S., Kesharwani, P., & Iyer, A. K. (2017). Polyvalent folate-dendrimer-coated iron oxide theranostic nanoparticles for simultaneous magnetic resonance imaging and precise cancer cell targeting. *Biomacromolecules*, 18(4), 1197-1209.

- Lee, K., David, A. E., Zhang, J., Shin, M. C., & Yang, V. C. (2017). Enhanced accumulation of theranostic nanoparticles in brain tumor by external magnetic field mediated in situ clustering of magnetic nanoparticles. *Journal of Industrial and Engineering Chemistry*, *54*, 389-397.
- Larimi, M. M., Ramiar, A., & Ranjbar, A. A. (2014). Numerical simulation of magnetic nanoparticles targeting in a bifurcation vessel. *Journal of Magnetism and Magnetic Materials*, *362*, 58-71.
- Liu, J., Choi, G. M., & Cahill, D. G. (2014). Measurement of the anisotropic thermal conductivity of molybdenum disulfide by the time-resolved magneto-optic Kerr effect. *Journal of Applied Physics*, *116*(23), 233107.
- Liu, L. J., Brown, S. L., Ewing, J. R., & Schlesinger, M. (2011). Phenomenological model of interstitial fluid pressure in a solid tumor. *Physical Review E*, *84*(2), 021919.
- Liu, H. L., Hua, M. Y., Yang, H. W., Huang, C. Y., Chu, P. C., Wu, J. S., & Wei, K. C. (2010). Magnetic resonance monitoring of focused ultrasound/magnetic nanoparticle targeting delivery of therapeutic agents to the brain. *Proceedings of the National Academy of Sciences*, *107*(34), 15205-15210.
- Lübbe, A.S., & Bergemann, C. in: Shapiro, B (Ed.). (2005), Email Exchange.
- Loukopoulos, V. C., & Tzirtzilakis, E. E. (2004). Biomagnetic channel flow in spatially varying magnetic field. *International Journal of Engineering Science*, *42*(5-6), 571-590.

- Loukopoulos, V. C., Katsiaris, G. A., & Karahalios, G. T. (2003). A steady-state solver for the simulation of Taylor vortices in spherical annular flow. *Computer Methods in Applied Mechanics and Engineering*, 192(26-27), 2993-3003.
- Loukopoulos, V. C., & Tzirtzilakis, E. E. (2004). Biomagnetic channel flow in spatially varying magnetic field. *International Journal of Engineering Science*, 42(5-6), 571-590.
- Lübbe, A.S., Alexiou, C., & Bergemann, C. (2001). Clinical applications of magnetic drug targeting. *Journal of Surgical Research*, 95(2), 200-206.
- Lübbe, A.S., Bergemann, C., Brock, J., & McClure, D. G. (1999). Physiological aspects in magnetic drug-targeting. *Journal of Magnetism and Magnetic Materials*, 194(1-3), 149-155.
- Lübbe, A.S., Bergemann, C., Riess, H., Schriever, F., Reichardt, P., Possinger, K., & Hohenberger, P. (1996a). Clinical experiences with magnetic drug targeting: A phase I study with 4'-epidoxorubicin in 14 patients with advanced solid tumors. *Cancer Research*, 56(20), 4686-4693.
- Lübbe, A.S., Bergemann, C., Huhnt, W., Fricke, T., Riess, H., Brock, J. W., & Huhn, D. (1996b). Preclinical experiences with magnetic drug targeting: Tolerance and efficacy. *Cancer Research*, 56(20), 4694-4701.
- Mamun, K., Funazaki, K., Akter, S., & Akhter, M. N. (2020). The effect of magnetic field on blood flow through stenotic artery-a review on bio-magnetic fluid dynamics. *Series on Biomechanics*, 34 (1), 20-30.

- Mukherjee, S., Liang, L., & Veiseh, O. (2020). Recent advancements of magnetic nanomaterials in cancer therapy. *Pharmaceutics*, *12*(2), 147.
- Mohammadian, M., & Pourmehran, O. (2019). CFD simulation of magnetic drug delivery to a human lung using an SAW nebulizer. *Biomechanics and Modeling in Mechanobiology*, *18*(3), 547-562.
- Manshadi, M. K., Saadat, M., Mohammadi, M., Kamali, R., Shamsi, M., Naseh, M., & Sanati-Nezhad, A. (2019). Magnetic aerosol drug targeting in lung cancer therapy using permanent magnet. *Drug delivery*, *26*(1), 120-128.
- Mohd Zin, N. A., Khan, I., & Shafie, S. (2016). Influence of thermal radiation on unsteady MHD free convection flow of Jeffrey fluid over a vertical plate with ramped wall temperature. *Mathematical Problems in Engineering*, 2016.
- Mao, C., Huang, Y., Zhou, X., Gan, H., Zhang, J., & Zhou, Z. (2014). The tribological properties of nanofluid used in minimum quantity lubrication grinding. *The International Journal of Advanced Manufacturing Technology*, *71*(5), 1221-1228.
- Mahian, O., Kianifar, A., Kalogirou, S. A., Pop, I., & Wongwises, S. (2013). A review of the applications of nanofluids in solar energy. *International Journal of Heat and Mass Transfer*, *57*(2), 582-594.
- McKay, J. C., Prato, F. S., & Thomas, A. W. (2007). A literature review: The effects of magnetic field exposure on blood flow and blood vessels in the microvasculature. *Bioelectromagnetics: Journal of the Bioelectromagnetics Society, The Society for Physical Regulation in Biology and Medicine, The European Bioelectromagnetics Association*, *28*(2), 81-98.



- Mahmud, S., & Fraser, R. A. (2005). Flow, thermal, and entropy generation characteristics inside a porous channel with viscous dissipation. *International Journal of Thermal Sciences*, 44(1), 21-32.
- Matsuki, H., Yamasawa, K., & Murakami, K. (1977). Experimental considerations on a new automatic cooling device using temperature-sensitive magnetic fluid. *IEEE Transactions on Magnetics*, 13(5), 1143-1145.
- McBride, J. J., & Westrum Jr, E. F. (1976). Low-temperature heat capacity of anisotropic crystals lamellar molybdenum disulfide. *The Journal of Chemical Thermodynamics*, 8(1), 37-44.
- Nikookar, H., Abouali, O., Eghtesad, M., Sadrizadeh, S., & Ahmadi, G. (2019). Enhancing drug delivery to human trachea through oral airway using magnetophoretic steering of microsphere carriers composed of aggregated superparamagnetic nanoparticles and nanomedicine: A numerical study. *Journal of Aerosol Science*, 127, 63-92.
- Nacev, A. N. (2013). *Magnetic drug targeting: developing the basics*. University of Maryland, College Park.
- Nacev, A., Beni, C., Bruno, O., & Shapiro, B. (2011a). The behaviors of ferromagnetic nano-particles in and around blood vessels under applied magnetic fields. *Journal of Magnetism and Magnetic Materials*, 323(6), 651-668.
- Nacev, A., Kim, S. H., Rodriguez-Canales, J., Tangrea, M. A., Shapiro, B., & Emmert-Buck, M. R. (2011b). A dynamic magnetic shift method to increase nanoparticle concentration in cancer metastases: A feasibility study using simulations on autopsy specimens. *International Journal of Nanomedicine*, 6, 2907.

- Nacev, A., Weinberg, I. N., Stepanov, P. Y., Kupfer, S., Mair, L. O., Urdaneta, M. G., & Shapiro, B. (2015). Dynamic inversion enables external magnets to concentrate ferromagnetic rods to a central target. *Nano Letters*, *15*(1), 359-364.
- Ostrovski, Y., Hofemeier, P., & Sznitman, J. (2016). Augmenting regional and targeted delivery in the pulmonary acinus using magnetic particles. *International Journal of Nanomedicine*, *11*, 3385.
- Pawar, S., & San, O. (2019). CFD Julia: A learning module structuring an introductory course on computational fluid dynamics. *Fluids*, *4*(3), 159.
- Pourmehran, O., Gorji, T. B., & Gorji-Bandpy, M. (2016). Magnetic drug targeting through a realistic model of human tracheobronchial airways using computational fluid and particle dynamics. *Biomechanics and Modeling in Mechanobiology*, *15*(5), 1355-1374.
- Pedrizzetti, G., La Canna, G., Alfieri, O., & Tonti, G. (2014). The vortex—An early predictor of cardiovascular outcome. *Nature Reviews Cardiology*, *11*(9), 545-553.
- Pouponneau, P., Leroux, J. C., Soulez, G., Gaboury, L., & Martel, S. (2011). Co-encapsulation of magnetic nanoparticles and doxorubicin into biodegradable microcarriers for deep tissue targeting by vascular MRI navigation. *Biomaterials*, *32*(13), 3481-3486.
- Polyak, B., Fishbein, I., Chorny, M., Alferiev, I., Williams, D., Yellen, B., & Levy, R. J. (2008). High field gradient targeting of magnetic nanoparticle-loaded endothelial cells to the surfaces of steel stents. *Proceedings of the National Academy of Sciences*, *105*(2), 698-703.

- Padera, T. P., Stoll, B. R., Tooredman, J. B., Capen, D., di Tomaso, E., & Jain, R. K. (2004). Cancer cells compress intratumour vessels. *Nature*, *427*(6976), 695-695.
- Pauling, L., & Coryell, C. D. (1936). The magnetic properties and structure of hemoglobin, oxyhemoglobin and carbonmonoxyhemoglobin. *Proceedings of the National Academy of Sciences*, *22*(4), 210-216.
- Rosiere, R., Van Woensel, M., Gelbcke, M., Mathieu, V., Hecq, J., Mathivet, T., & Wauthoz, N. (2018). New folate-grafted chitosan derivative to improve delivery of paclitaxel-loaded solid lipid nanoparticles for lung tumor therapy by inhalation. *Molecular Pharmaceutics*, *15*(3), 899-910.
- Russo, F., Boghi, A., & Gori, F. (2018). Numerical simulation of magnetic nano drug targeting in patient-specific lower respiratory tract. *Journal of Magnetism and Magnetic Materials*, *451*, 554-564.
- Rehman, S. U., Haq, R. U., Khan, Z. H., & Lee, C. (2016). Entropy generation analysis for non-Newtonian nanofluid with zero normal flux of nanoparticles at the stretching surface. *Journal of the Taiwan Institute of Chemical Engineers*, *63*, 226-235.
- Rukshin, I., Mohrenweiser, J., Yue, P., & Afkhami, S. (2017). Modeling superparamagnetic particles in blood flow for applications in magnetic drug targeting. *Fluids*, *2*(2), 29.
- Raptis, A., Xenos, M., Tzirtzilakis, E., & Matsagkas, M. (2014). Finite element analysis of magnetohydrodynamic effects on blood flow in an aneurysmal geometry. *Physics of Fluids*, *26*(10), 101901.

- Rudnick, S. I., Lou, J., Shaller, C. C., Tang, Y., Klein-Szanto, A. J., Weiner, L. M., & Adams, G. P. (2011). Influence of affinity and antigen internalization on the uptake and penetration of Anti-HER2 antibodies in solid tumors. *Cancer Research*, *71*(6), 2250-2259.
- Raut, S. L., Kirthivasan, B., Bommana, M. M., Squillante, E., & Sadoqi, M. (2010). The formulation, characterization and in vivo evaluation of a magnetic carrier for brain delivery of NIR dye. *Nanotechnology*, *21*(39), 395102.
- Rosen, J. (2004). Permeability (Physics), Encyclopedia of Physics, Facts on File science library, New York: Facts on File, 2004, ISBN 9780816049745.
- Ranz W. E., & Marshall Jr. W. R. (1952). Evaporation from drops, Part I. *Chemical Engineering Progress*. *48* (3), 141–146.
- Said, Z., Sundar, L. S., Tiwari, A. K., Ali, H. M., Sheikholeslami, M., Bellos, E., & Babar, H. (2021). Recent advances on the fundamental physical phenomena behind stability, dynamic motion, thermophysical properties, heat transport, applications, and challenges of nanofluids. *Physics Reports*, (in press).
- Saadat, M., Manshadi, M. K., Mohammadi, M., Zare, M. J., Zarei, M., Kamali, R., & Sanati-Nezhad, A. (2020). Magnetic particle targeting for diagnosis and therapy of lung cancers. *Journal of Controlled Release*.
- Sharifi, A., Motlagh, S. Y., & Badfar, H. (2019). Ferro hydro dynamic analysis of heat transfer and biomagnetic fluid flow in channel under the effect of two inclined permanent magnets. *Journal of Magnetism and Magnetic Materials*, *472*(0), 115-122.

- Saenrueang, T., Promthet, S., Kamsa-Ard, S., & Pongsaa, P. (2019). Cervical cancer in Khon Kaen, Thailand: Analysis of 1990-2014 incidence data and prediction of future trends. *Asian Pacific journal of cancer prevention: APJCP*, 20(2), 369.
- Sun, Q., You, Q., Wang, J., Liu, L., Wang, Y., Song, Y., & Li, N. (2018a). Theranostic nanoplatform: Triple-modal imaging-guided synergistic cancer therapy based on liposome-conjugated mesoporous silica nanoparticles. *ACS Applied Materials & Interfaces*, 10(2), 1963-1975.
- Sun, W., Fan, J., Wang, S., Kang, Y., Du, J., & Peng, X. (2018b). Biodegradable drug-loaded hydroxyapatite nanotherapeutic agent for targeted drug release in tumors. *ACS Applied Materials & Interfaces*, 10(9), 7832-7840.
- Shamsi, M., Sedaghatkish, A., Dejam, M., Saghafian, M., Mohammadi, M., & Sanati-Nezhad, A. (2018). Magnetically assisted intraperitoneal drug delivery for cancer chemotherapy. *Drug Delivery*, 25(1), 846-861.
- Soleimani, S., Shamsi, M., Ghazani, M. A., Modarres, H. P., Valente, K. P., Saghafian, M., & Sanati-Nezhad, A. (2018). Translational models of tumor angiogenesis: A nexus of in silico and in vitro models. *Biotechnology Advances*, 36(4), 880-893.
- Steuperaert, M., Falvo D'Urso Labate, G., Debbaut, C., De Wever, O., Vanhove, C., Ceelen, W., & Segers, P. (2017). Mathematical modeling of intraperitoneal drug delivery: simulation of drug distribution in a single tumor nodule. *Drug Delivery*, 24(1), 491-501.
- Saatchi, K., Tod, S. E., Leung, D., Nicholson, K. E., Andreu, I., Buchwalder, C., & Gray, S. L. (2017). Characterization of alendronic-and undecylenic acid coated magnetic

- nanoparticles for the targeted delivery of rosiglitazone to subcutaneous adipose tissue. *Nanomedicine: Nanotechnology, Biology and Medicine*, 13(2), 559-568.
- Sur, I., & Taipale, J. (2016). The role of enhancers in cancer. *Nature Reviews Cancer*, 16(8), 483-493.
- Sefidgar, M., Soltani, M., Raahemifar, K., Bazmara, H., Nayinian, S. M. M., & Bazargan, M. (2014). Effect of tumor shape, size, and tissue transport properties on drug delivery to solid tumors. *Journal of Biological Engineering*, 8(1), 1-13.
- Siegel, R., & Jemal, A. (2015). Cancer facts & Figures 2015. *American Cancer Society Cancer Facts & Figures*.
- Su, Y., Gong, L., Li, B., & Chen, D. (2015). An experimental investigation on thermal properties of molybdenum disulfide nanofluids. In *Proceedings of the 2015 International Conference on Materials, Environmental and Biological Engineering, Guilin, China* (pp. 28-30).
- Schuerle, S., Erni, S., Flink, M., Kratochvil, B. E., & Nelson, B. J. (2012). Three-dimensional magnetic manipulation of micro-and nanostructures for applications in life sciences. *IEEE Transactions on Magnetics*, 49(1), 321-330.
- Soltani, M., & Chen, P. (2012). Effect of tumor shape and size on drug delivery to solid tumors. *Journal of Biological Engineering*, 6(1), 1-15.
- Shapiro, B. (2009). Towards dynamic control of magnetic fields to focus magnetic carriers to targets deep inside the body. *Journal of Magnetism and Magnetic Materials*, 321(10), 1594-1599.

- Shen, B. (2008). *Minimum quantity lubrication grinding using nanofluids* (Doctoral dissertation, University of Michigan).
- Schulze, K., Koch, A., Schöpf, B., Petri, A., Steitz, B., Chastellain, M., & von Rechenberg, B. (2005). Intraarticular application of superparamagnetic nanoparticles and their uptake by synovial membrane—an experimental study in sheep. *Journal of Magnetism and Magnetic Materials*, 293(1), 419-432.
- Saltzman, W. M. (2001). *Drug delivery: Engineering Principles for Drug Therapy*. Oxford University Press.
- Schenck, J. F., Dumoulin, C. L., Redington, R.W., Kressel, H. Y., Elliot, R. T., & McDougall, I. L. (1992). Human exposure to 4.0-Tesla magnetic fields in a whole-body scanner. *Medical Physics*, 19(1), 1089-1098.
- Sud, V. K., & Sekhon, G. S. (1989). Blood flow through the human arterial system in the presence of a steady magnetic field. *Physics in Medicine & Biology*, 34(7), 795.
- Tak Takayasu, M., Duske, N., Ash, S., & Friedlaender, F. (1982). HGMS studies of blood cell behavior in plasma. *IEEE Transactions on Magnetics*, 18(6), 1520-1522.
- Timofeeva, E. V., Routbort, J. L., & Singh, D. (2009). Particle shape effects on thermophysical properties of alumina nanofluids. *Journal of Applied Physics*, 106(1), 014304.
- Tiwari, R. K., & Das, M. K. (2007). Heat transfer augmentation in a two-sided lid-driven differentially heated square cavity utilizing nanofluids. *International Journal of Heat and Mass Transfer*, 50(9-10), 2002-2018.

- Tozer, G. M., Kanthou, C., & Baguley, B. C. (2005). Disrupting tumour blood vessels. *Nature Reviews Cancer*, 5(6), 423-435.
- Tzirtzilakis, E. E. (2005). A mathematical model for blood flow in magnetic field. *Physics of Fluids*, 17(7), 077103.
- Tzirtzilakis, E. E. (2008). A simple numerical methodology for BFD problems using stream function vorticity formulation. *Communications in Numerical Methods in Engineering*, 24(8), 683-700.
- Tzirtzilakis, E. E. (2015). Biomagnetic fluid flow in an aneurysm using ferrohydrodynamics principles. *Physics of Fluids*, 27(6), 061902.
- Tzirtzilakis, E. E., & Loukopoulos, V. C. (2005). Biofluid flow in a channel under the action of a uniform localized magnetic field. *Computational Mechanics*, 36(5), 360-374.
- Umadevi, C., Dhange, M., Haritha, B., & Sudha, T. (2021). Flow of blood mixed with copper nanoparticles in an inclined overlapping stenosed artery with magnetic field. *Case Studies in Thermal Engineering*, 25, 100947.
- Virani, S., Bilheem, S., Chansaard, W., Chitapanarux, I., Daoprasert, K., Khuanchana, S., & Sriplung, H. (2017). National and subnational population-based incidence of cancer in Thailand: assessing cancers with the highest burdens. *Cancers*, 9(8), 108.
- Wang, H., Wu, L., & Sun, X. (2020). Intratracheal Delivery of Nano-and Microparticles and Hyperpolarized Gases: A Promising Strategy for the Imaging and Treatment of Respiratory Disease. *Chest*, 157(6), 1579-1590.



- Wei, J., Shuai, X., Wang, R., He, X., Li, Y., Ding, M., & Fu, Q. (2017). Clickable and imageable multiblock polymer micelles with magnetically guided and PEG-switched targeting and release property for precise tumor theranosis. *Biomaterials*, *145*,138-153.
- Wilson, M. W., Kerlan Jr, R. K., Fidelman, N. A., Venook, A. P., LaBerge, J. M., Koda, J., & Gordon, R. L. (2004). Hepatocellular carcinoma: regional therapy with a magnetic targeted carrier bound to doxorubicin in a dual MR imaging/conventional angiography suite—Initial experience with four patients. *Radiology*, *230*(1), 287-293.
- Wen, D., & Ding, Y. (2004). Experimental investigation into convective heat transfer of nanofluids at the entrance region under laminar flow conditions. *International Journal of Heat and Mass Transfer*, *47*(24), 5181-5188.
- Widder, K. J., Morris, R. M., Poore, G., Howard, D. P., & Senyei, A. E. (1981). Tumor remission in Yoshida sarcoma-bearing rats by selective targeting of magnetic albumin microspheres containing doxorubicin. *Proceedings of the National Academy of Sciences*, *78*(1), 579-581.
- Yue, P., Lee, S., Afkhami, S., & Renardy, Y. (2012). On the motion of superparamagnetic particles in magnetic drug targeting. *Acta Mechanica*, *223*(3), 505-527.
- Yang, N., & Vafai, K. (2006). Modeling of low-density lipoprotein (LDL) transport in the artery—effects of hypertension. *International Journal of Heat and Mass Transfer*, *49*(5-6), 850-867.

- Xenos, M. A., & Tzirtzilakis, E. E. (2013). MHD effects on blood flow in a stenosis. *Advances in Dynamical Systems and Applications*, 8(2), 427-437.
- Xie, Y., Zeng, P., Siegel, R. A., Wiedmann, T. S., Hammer, B. E., & Longest, P. W. (2010). Magnetic deposition of aerosols composed of aggregated superparamagnetic nanoparticles. *Pharmaceutical Research*, 27(5), 855-865.
- Xu, H., Song, T., Bao, X., & Hu, L. (2005). Site-directed research of magnetic nanoparticles in magnetic drug targeting. *Journal of Magnetism and Magnetic Materials*, 293(1), 514-519.
- Yamamoto, T., Nagayama, Y., & Tamura, M. (2004). A blood-oxygenation-dependent increase in blood viscosity due to a static magnetic field. *Physics in MediciBiology*, 49(14), 3267-3277.
- Zhang, Y., Li, C., Jia, D., Li, B., Wang, Y., Yang, M., & Zhang, X. (2016). Experimental study on the effect of nanoparticle concentration on the lubricating property of nanofluids for MQL grinding of Ni-based alloy. *Journal of Materials Processing Technology*, 232, 100-115.
- Zhang, Y., Gu, S., Yan, B., & Ren, J. (2012). Solvent-free ionic molybdenum disulphide (MoS<sub>2</sub>) nanofluids. *Journal of Materials Chemistry*, 22(30), 14843-14846.
- Zin, N. A. M., Khan, I., & Shafie, S. (2016). The impact silver nanoparticles on MHD free convection flow of Jeffrey fluid over an oscillating vertical plate embedded in a porous medium. *Journal of Molecular Liquids*, 222, 138-150.